UILU-ENG-76-2548

FINAL REPORT ON RESEARCH IN INFRARED

AND OPTICAL QUANTUM ELECTRONICS

by

Henry Merkelo

May 1976

Quantum Electronics Research Laboratory
Department of Electrical Engineering
Engineering Experiment Station
University of Illinois
Urbana, Illinois 61801

REPORT DOCUMENTATION PAGE		READ INSTRUCTIONS BEFORE COMPLETING FORM
1. REPORT NUMBER	2. GOVT ACCESSION NO.	3. RECIPIENT'S CATALOG NUMBER
4. TITLE (and Subtitle) INFRARED AND OPTICAL QUANTUM ELECTRONICS. A. INFRARED SENSITIVITY OF PLASMAS. B. PICOSECOND DYNAMICS OF SURFACE PHOTOELECTRONS.		5. TYPE OF REPORT & PERIOD COVERED FINAL rept.
		6. PERFORMING ORG. REPORT NUMBER UILU-ENG-76-2548
7. AUTHOR(s) Henry Merkelo		8. CONTRACT OR GRANT NUMBER(s) N00014-67-A-0305-0017
9. PERFORMING ORGANIZATION NAME AND ADDRESS University of Illinois Dept. of Electrical Engineering Urbana, IL 61801		10. PROGRAM ELEMENT, PROJECT, TASK AREA & WORK UNIT NUMBERS AD 1731319.1431 00014 2B 121107
11. CONTROLLING OFFICE NAME AND ADDRESS Office of Naval Research Physics Program Office Code 421 Arlington, Virginia 22217		12. REPORT DATE May 1976
		13. NUMBER OF PAGES
14. MONITORING AGENCY NAME & ADDRESS(If different from Controlling Office) 168p.		15. SECURITY CLASS. (of this report) Unclassified
		15a. DECLASSIFICATION/DOWNGRADING SCHEDULE

16. DISTRIBUTION STATEMENT (of this Report)

Approved for Public Release: Distribution Unlimited.

17. DISTRIBUTION STATEMENT (of the abstract entered in Block 20, if different from Report)

18. SUPPLEMENTARY NOTES

19. KEY WORDS (Continue on reverse side if necessary and identify by block number)

Plasmas, Low Density, He, Ne, Ar, Xe, Photoelectrons, Negative-Affinity, Quenching, Photocathodes, Picosecond, Sampling
Infrared
Laser, CO_2, Photoionization

20. ABSTRACT (Continue on reverse side if necessary and identify by block number)

Upon discovery of the infrared sensitivity of weakly ionized plasmas, research was initiated at establishing the quantum origins of the observed interactions. Taking into account the obvious inverse bremsstrahlung process, studies were made to evaluate the role of bound-bound and bound-free transitions under the influence of low energy photon flux corresponding to the intermediate and far-infrared portions of the spectrum. It was established and documented that in a broad range of electron temperatures and densities of weakly ionized plasmas, the bound-free transitions induced by infrared photons affect the recombination

DD FORM 1473 EDITION OF 1 NOV 65 IS OBSOLETE

ABSTRACT (20)

process to a significant and, frequently, to dominant degree. Theoretical results are obtained on the basis of a hydrogenic model. Experiments demonstrate the generality of the infrared sensitivity of plasmas.

A separate phase of research in optical quantum electronics dealt with optical interaction with surface and near surface electrons in photoemissive materials. In particular, the dynamics on picosecond time scales of electrons released from the surface and near-surface of select materials is of both fundamental and practical interest. Negative electron affinity materials, known for their high quantum efficiency, are predicted to exhibit maximum time dispersion of a step excitation. Preliminary studies and the development of tools needed for an experimental determination of parameters on picosecond time scales, were the principal goals of this effort. As a byproduct, a patent was filed and granted on the more successful configurations of devices designed to carry out the basic surface emission studies. The program is currently well under way and results continue to emerge in an area that was heretofore not amenable to experimental exploration due to the unavailability of picosecond-resolving devices.

FINAL REPORT ON RESEARCH IN INFRARED

AND OPTICAL QUANTUM ELECTRONICS

by

Henry Merkelo

May 1976

Contract No. N00014-67-A-0305-0017

Prepared for the

Office of Naval Research
Physics Program Office
Code 421
Arlington, Virginia 22217

Quantum Electronics Research Laboratory
Department of Electrical Engineering
Engineering Experiment Station
University of Illinois
Urbana, Illinois 61801

TABLE OF CONTENTS

SUMMARY

Upon discovery of the infrared sensitivity of weakly ionized plasmas, research was initiated at establishing the quantum origins of the observed interactions. Taking into account the obvious inverse bremsstrahlung process, studies were made to evaluate the role of bound-bound and bound-free transitions under the influence of low energy photon flux corresponding to the intermediate and far-infrared portions of the spectrum. It was established and documented that in a broad range of electron temperatures and densities of weakly ionized plasmas, the bound-free transitions induced by infrared photons affect the recombination process to a significant and, frequently, to a dominant degree. Theoretical results are obtained on the basis of a hydrogenic model. Experiments demonstrate the generality of the infrared sensitivity of plasmas.

A separate phase of research in optical quantum electronics dealt with optical interaction with surface and near surface electrons in photoemissive materials. In particular, the dynamics on picosecond time scales of electrons released from the surface and near-surface of select materials is of both fundamental and practical interest. Negative electron affinity materials, known for their high quantum efficiency, are predicted to exhibit maximum time dispersion of a step excitation. Preliminary studies and the development of tools needed for an experimental determination of parameters on picosecond time scales, were the principal goals of this effort. As a byproduct, a patent was filed and granted on the more successful configurations of devices designed to carry out the basic surface emission studies. The program is currently well under way and results continue to emerge in an area that was heretofore not amenable to experimental exploration due to the unavailability of picosecond-resolving devices.

EVIDENCE OF LOW-BINDING-ENERGY ELECTRONS
IN A LOW-TEMPERATURE HELIUM AFTERGLOW*

J. P. Kaplafka, H. Merkelo, and L. Goldstein
Gaseous Electronics Laboratory, University of Illinois, Urbana, Illinois
(Received 12 July 1968)

Moderate, pulsed microwave heating of the free electrons in a weakly ionized helium afterglow plasma at 9.5 Torr at a gas temperature of 77°K produces an unusual modulation of the visible afterglow light. Observations of a second (probing) microwave signal indicate an accompanying significant increase in free-electron density under the assumption that there is no significant anomalous phase shift or absorption of the probing signal.

Observations have been made of the modulation of both visible afterglow radiation and microwave transmission resulting from perturbations of the free-electron gas temperature imposed during various intervals in the decay of a weakly ionized helium gas at a pressure of 9.5 Torr maintained at a gas temperature near 77°K. The perturbation of the free-electron temperature T_e is produced by the introduction of a second microwave signal of a different frequency and necessarily higher power than the probing microwave signal. This "heating" microwave signal is ≤ 200 μsec in duration. Under the tentative assumption that there is no significant anomalous phase shift or absorption of the transmitted probing microwave signal, interpretation of the modulation on phase shift and absorption implies a significant, unexpected increase in free-electron density n_e (on the order of unperturbed n_e) in the course of moderate microwave heating and a subsequent fast (~50-100 μsec) return to unperturbed n_e upon removal of heating.

The discharge tube is Pyrex, rectangular, approximately 24 cm in length, and makes a close fit within an X-band microwave waveguide. A 2-μsec, high-voltage (~7-kV) pulse applied between electrodes located outside the waveguide produces breakdown of the cataphoretically pure helium. At 200 μsec after breakdown, n_e is found to be ~10^{11}/cc, falling to 10^9/cc in approximately 4 msec. Spectrally resolved observations of visible light intensities in the early afterglow (within 800 μsec) were made with a Jarrell-Ash, Model 82-000, 0.5-m monochromator and an RCA phototube (S-11 photocathode). The decay of atomic He lines is markedly different than that of diatomic molecular He bands. The lines are very strong in the breakdown but decay rapidly in intensity. By approximately 300 μsec the sum of atomic line contributions to the signal from the photomultiplier can be neglected in comparison with the sum of molecular band contributions.

The most prominent six molecular bands (5735 Å $[3\,^3\Delta_u-2\,^3\Pi_g]$, 4725 Å $[4\,^1\Sigma_u{}^+-2\,^1\Pi_g]$, 4650 Å $[3\,^3\Pi_g-2\,^3\Sigma_u{}^+]$, 4547 Å $[4\,^3\Sigma_u{}^+-2\,^3\Pi_g]$, ~4470 Å, and 4439 Å $[4\,^3\Pi_u-2\,^3\Pi_g]$)[1,2] can be followed with 15-Å resolution to beyond 800 μsec. These six bands appear to decay at the same rate. Beyond 800 μsec the observations of light intensity are not spectrally resolved; i.e., they are observations of the signal from the photomultiplier with total visible radiation incident on the photocathode.

When a short pulse of microwave radiation of insufficient power to cause significant ionization of ground-state or metastable-state He atoms is incident on an He afterglow plasma of gas temperature near 300°K at times on the order of a millisecond after the discharge, the visible afterglow light intensity is partially quenched during application of the pulse.[3,4] Generally such a pulse of constant power will maintain a constant free-electron temperature T_e (after the time necessary to establish this T_e) during its application even in the event that n_e decays appreciably during its application. If the pulse length is short (i.e., no significant change of n_e by recombination or diffusion losses occurs during application), then the afterglow light is observed to maintain a constant level until the removal of the microwaves. At this time the light intensity returns to approximately the same intensity as before introduction of the microwaves, in the time required for T_e to decay by means of elastic collisions between the free electrons and helium atoms.[4] The partial quenching of visible afterglow light intensity has been interpreted as due to a reduction of the recombination coefficient by increase in T_e which results in subsequent reduction of the light from recombination.

The upper traces of Fig. 1 illustrate the very different effect produced on the visible afterglow light of a 9.5-Torr, helium afterglow plasma at a gas temperature of 77°K. The electron temper-
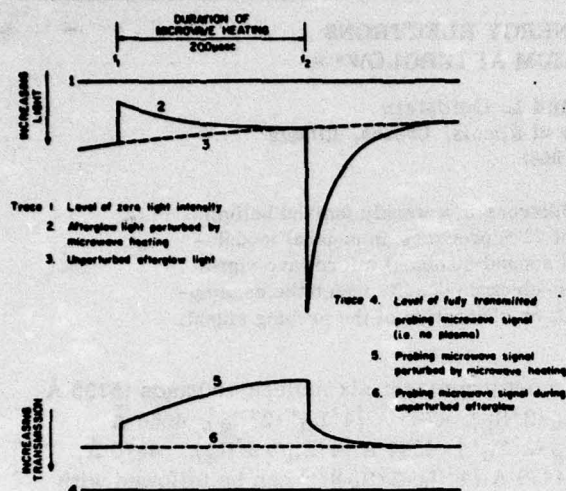
FIG. 1. Effects of moderate microwave heating upon the visible afterglow light (upper traces) and upon a transmitted probing microwave signal (lower traces) for a He afterglow plasma at a gas pressure of 9.5 Torr and gas temperature of 77°K.

FIG. 2. Typical plot of electron density at 150 μsec of microwave heating versus electron temperature during heating. Each has been normalized to the respective unperturbed value for this particular afterglow time. ($T_{e_0} \sim 170$°K for this plot, gas temperature of 77°K and pressure of 9.5 Torr.)

ature increases rapidly (~3 μsec) at the time of application of the microwave pulse t_1, accompanied by an expected rapid partial quenching of the visible afterglow light. However, visible afterglow light subsequently increases and reaches a nearly constant amplitude within approximately 150 μsec. This amplitude is nearly coincident with the unperturbed amplitude when the heating is relatively small (this is the case in Fig. 1) and progressively less than the unperturbed amplitude as heating power is increased. At the time of removal of the heating microwaves, visible afterglow light intensity increases, within approximately 2 μsec, to an amplitude that can be several times the unperturbed and then decays to the unperturbed amplitude in approximately 100-200 μsec. Such a transient increase in afterglow light upon removal of heating microwaves was observed in He afterglows at gas temperatures of approximately 77 and 4.2°K by Goldan, Berlande, and Goldstein and termed the "afterpulse."[5]

The lower traces of Fig. 1 illustrate amplitude modulation produced on the low-power probing microwave signal (applied over a longer interval of time than the microwave heating pulse) due to application of the heating pulse. The rapid increase in the absorption at t_1 is in response to a rapid increase in T_e, inferred from the increase in the elastic electron-neutral collision frequency for momentum transfer as determined from

absorption and phase-shift measurements on the transmitted probing microwave signal. The subsequent more gradual increase in absorption during application of the heating microwaves is found to result from an increase in $n_e - T_e$ remaining approximately constant. In the case of Fig. 1 the increase in T_e by heating is about 100% and the modulations of the probing microwave signal and the visible afterglow light are typical of this relative increase in T_e throughout the region where most observations were made, i.e., between 1 and 3 msec.

Figure 2 is a typical plot of n_e, as inferred from the absorption and phase-shift measurements, at 150 μsec of microwave heating versus T_e during heating, both normalized to their respective unperturbed values. It should be noted that T_{e_0} at 1 msec of the afterglow (i.e., unperturbed T_e at 1 msec) is still falling and well above 77°K (~190 and ~150°K at 2 msec).[6] Ambipolar diffusion enhanced by increasing T_e must be significant in determining the shape of the latter portions of the curve, but nonetheless n_e can be increased by a factor of almost 3 during microwave heating, and merely doubling T_e gives rise to an almost 50% increase in n_e.

When the heating microwaves are suddenly removed at t_2, T_e falls rapidly to a value near unperturbed T_e, accompanied by the almost discontinuous fall in absorption seen in Fig. 1. The more gradual change in absorption after this fall results mainly from a decrease in n_e to unperturbed n_e.

The modulation of the unresolved visible light intensity is assumed to involve no spectral redistribution of the observed radiation because the six major molecular bands listed earlier show apparently identical modulations, relative to their own unperturbed intensities, for early afterglow times where they can be spectrally resolved.

The preceding remarks were based on the assumption that the free-electron density and electron temperature measurements are reliable. However, the reliability of determining free-electron density and electron temperature from phase-shift and absorption measurements on the probing microwave signal rests with the assumption that the phase shifts and absorptions are related to the free electrons undergoing elastic electron-atom collisions. The following are some additional possibilities:

(1) Inelastic electron collisions. However, at a given time in the afterglow a significant effect on phase shift or absorption due to free electrons undergoing inelastic collisions requires a population of "target" states several order of magnitude larger than the free-electron density or inelastic collision cross sections several orders of magnitude larger than the elastic electron-ground-state-atom collision cross section for momentum transfer.

(2) Resonant absorption of probing microwaves (i.e., absorption by means of photon-induced transitions between bound states). The probing microwave photon energy is small ($\sim 3 \times 10^{-5}$ eV). Therefore it is necessary to consider states which are situated close in energy. It is difficult to explain the modulation of visible molecular afterglow light if states responsible for a resonant microwave absorption are solely states of the atom. Moreover, it appears that if the probing microwave signal is significantly absorbed as the result of probing microwave photons inducing transitions between molecular rotational levels, the density of molecules in such rotational levels would be nearly as large as the density of helium atoms initially present in the gas ($\sim 10^{18}$/cc).

(3) Particle redistribution or oscillation. The possibility that the observed perturbations are due to particle redistribution was examined in several ways: (a) by spatially resolved observations of afterglow light across the width and along the length of the discharge tube, (b) by heating in the TE_{20} microwave mode rather than TE_{10} and observing visible afterglow light, and (c) by observing visible afterglow light emitted by a discharge tube situated outside the microwave waveguide and irradiated by means of a microwave horn. There was no evidence in these cases to support the possibility of spatial redistribution.

Tentative acceptance of the reliability of the measurements of n_e and T_e leads to certain implications: The rise of afterglow light (after the initial partial quenching) in the course of heating could be explained on the basis of increasing rate of recombination, caused by an increasing n_e. The afterpulse of light could be understood as a response to the sudden increase in recombination coefficient, the result of a rapid decrease in T_e. It should be noted that since it is difficult to determine at what time n_e actually returns to unperturbed n_e, it should not be inferred from Fig. 1 that the light in the tail of the afterpulse continues above its unperturbed level beyond this time.

The functional dependence of n_e on time t after removal of the microwave heating before n_e returns to normal cannot be explained by invoking a simple recombination law. Assuming that $dn_e/dt \propto n_e^\sigma$, slopes of plots of $\ln(dn_e/dt)$ vs $\ln n_e$ give inconsistent and, at times, inordinately high values of σ ($\sim 3 < \sigma < \sim 5$), T_e being essentially constant. Moreover dn_e/dt within this period is much greater than can be expected on the basis of the decay rates of n_e observed in the unperturbed afterglow. The additional observations that n_e returns to unperturbed n_e and that dn_e/dt at the time of application of the heating microwaves t_1 increases monotonically with T_e (i.e., monotonically with microwave heating power) suggest the following interpretation: There is a population $[X]$ of weakly bound electrons in a near-collisional equilibrium with the free-electron gas at a given afterglow time. Microwave heating of the free-electron gas has the effect of disturbing this equilibrium by increasing the destruction rate of $[X]$ and perhaps reducing the rate of formation. The electron density increases during heating until a new equilibrium population of state or states X is established at the enhanced T_e maintained during heating. After the microwave heating pulse is removed, T_e falls to a value near unperturbed T_e and $[X]$ is subsequently re-established at the value previous to heating.

At present additional efforts are being considered to confirm further the existence of a significant population of weakly bound electrons.

Administration under Contract No. NGR 14-005-037.

[1]G. Herzberg, Molecular Spectra and Molecular Structure: I. Spectra of Diatomic Molecules (D. Van Nostrand Company, Inc., Princeton, N.J., 1950), pp. 535-536.

[2]With the exception of 4470Å, the wavelengths given represent positions of the 0-0 bands. Herzberg's listing closest to the radiation observed to be maximum in the vicinity of 4470Å is a 0-0 band at 4456 Å [$4^3\Sigma_u^+ - 2^3\Pi_g$].

[3]L. Goldstein, J. M. Anderson, and G. L. Clark, Phys. Rev. 90, 486(L) (1953).

[4]C. L. Chen, C. C. Leiby, and L. Goldstein, Phys. Rev. 121, 1391 (1961).

[5]P. D. Goldan, J. A. Berlande, and L. Goldstein, Phys. Rev. Letters 13, 182 (1964).

[6]Assuming an elastic electron-neutral collision cross section for momentum transfer of 5.3×10^{-16} cm^2 from J. L. Pack and A. V. Phelps, Phys. Rev. 121, 798 (1961).

QUENCHING OF HELIUM AFTERGLOW BY INFRARED PHOTONS

J. P. Kaplafka, *H. Merkelo*, and *L. Goldstein*
Gaseous Electronics Laboratory
University of Illinois
Urbana, Illinois 61801
(Received 3 June 1969; in final form 16 July 1969)

The visible afterglow radiation from low-pressure weakly ionized helium exhibits a partial quenching due to absorption of infrared photons (0.11–0.14 eV). The helium sample is placed in the cavity of a Q-switched CO_2 laser and studied at gas temperatures in the range from 77 to 300°K. The partial quenching appears to originate from photon-induced change of population of a state or states of a neutral or ionic helium molecule.

A pulsed helium discharge tube was placed in the cavity of a Q-switched CO_2 laser. A partial quenching of the visible afterglow radiation from the weakly ionized helium—as large as 50% at a gas temperature near 77°K—is observed during the brief (~10 μsec) time interval of lasering. Gas pressure was varied in a range from a few tenths of a Torr to approximately 15 Torr, but the quenching is not observable below ~0.4 Torr at a gas temperature of 77°K or below ~2 Torr at room temperature. (Below these pressures the visible afterglow radiation consists primarily of atomic lines rather than molecular bands.) It is present throughout all but the very early afterglow period and appears to originate from photon-induced change of population of a state or states of a neutral or ionic helium molecule.

A major portion of the helium discharge tube (~50 cm in length and 10 mm i.d.) is contained within a styrofoam box to allow cooling of the helium gas in the region where observations are made of the visible afterglow radiation emitted following application of a 2- μsec several-thousand-volt discharge pulse. The helium is cataphoretically cleaned. The visible afterglow radiation is transmitted to the input of an RCA photomultiplier having an S-11 photocathode. Q switching of the CO_2 laser is accomplished by means of rotating one of the two spherical, cavity mirrors at a rate of 60 rps. Lasering occurs every 16.6 msec in the form of several short pulses spanning an interval of approximately 10 μsec. The time interval during which lasering takes place can be positioned to any time during the helium afterglow. The onset of quenching is essentially coincident in time with the onset of lasering. The measured rise times of the quenched light signals are found to be shorter than 0.5 μsec in all cases.

With the helium tube in a liquid-nitrogen bath (77°K) the percentage of quenching at most pressures can be conveniently obtained up to 3 msec after application of the 2-μsec helium-discharge voltage pulse. Within the precision of measurement of the change in visible radiation produced during lasering, the percentage of quenching varies little, after reaching a maximum in the very early afterglow, in comparison to the changes of parameters

of the electron gas. Based on microwave sensing measurements on systems under similar conditions of gas temperature (i.e., near 77°K), gas pressure, breakdown, and discharge tube geometry, it is expected that the free-electron density (~10^{10}/cc) changes by at least a factor of 10 and the free-electron temperature by at least a factor of 3.

In order to verify directly that the partial quenching is not due to an increase of temperature of the electron gas, the helium tube was inserted through a section of square cross-section microwave guide. Sensing microwaves at a frequency of 8.6 GHz were transmitted through this guide section at a low power level (so as not to disturb the electron-gas temperature) and observations were made of the transmitted signal during the interval of lasering. (An increase in temperature of the electron gas will cause an increase in the absorption of the microwave signal by the He plasma.) There was no clearly discernible change in absorption of the sensing microwaves during the interval of lasering. In order to verify the sensitivity of this method a proven means of changing electron temperature was introduced for the purpose of comparison. In order to selectively heat only the free-electron gas, a second microwave source operating at a frequency of 10.2 GHz was pulsed-on for a short time. The signal was transmitted through the guide section containing the helium tube, and its power was adjusted so that it produced the same percentage of quenching of the visible afterglow radiation, at the afterglow time of comparison, as was observed during lasering. The change in transmission (increased absorption) of the low power (sensing) microwave signal was clearly visible, as illustrated in Fig. 1. It is interesting to note that the helium afterglow has this capability of detecting and *distinguishing* between the incident infrared and microwave radiations. A partial quenching by the infrared irradiation is seen even during simultaneous application of a pulsed microwave signal of sufficient power to very substantially increase the electron temperature.

Since the partial quenching by the infrared photons with helium is not due to a heating of the electron gas, it appears that the lasering produces a partial destruction of the population of an excited
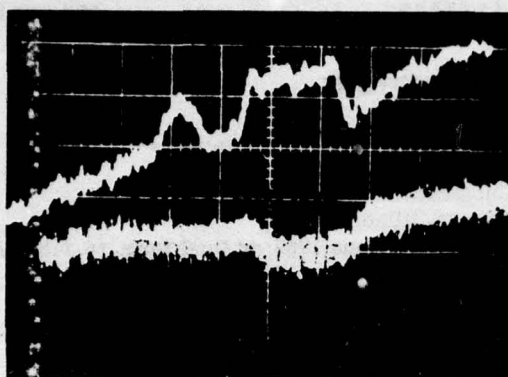
Fig. 1. Trace 1 is visible helium afterglow radiation between ~840 and 940 μsec after discharge (i.e., 10 μsec/cm) increasing downward. The radiation is shown partially quenched by infrared lasering and just adjacent to this it is partially quenched by a square pulse of microwave power. Trace 2 is the transmitted low power (sensing) microwave signal clearly perturbed (increased absorption) during microwave heating and virtually undisturbed during lasering. (Note that the lower trace is displaced slightly to the right on the screen.) The gas pressure was 8 Torr and gas temperature ~77°K.

specie(s) existing somewhere in the recombination cascade (even a state of the ion itself) that leads to the visible afterglow radiation.

It was previously observed by the authors, at gas temperature near 77°K and pressures of several Torr, that with similar breakdown and in the same discharge tube geometry the visible afterglow radiation after very early afterglow times is completely dominated by band radiation from the He_2 molecule.[1] The He_2^+ ion has been identified in room-temperature helium afterglows by means of mass spectrometry and recombination via this ion is assumed responsible for the observed He_2 band radiation in room-temperature afterglows. Recently, however, heavier helium ions have been identified at lower gas temperatures. The existence of an He_3^+ ion over a range of gas temperatures from 76 to 200°K and pressures from 1 to 30 Torr was inferred by means of drift-tube ion-mobility experiments.[2,3] In the course of these studies, Patterson[3] made the assessment that at 77°K the rate of formation of He_3^+ from He_2^+ is faster than the three-body formation of He_2^+ from He^+. In this regard and

as a direct proof of its existence, Ferguson et al.[4] found the He_3^+ ion, by means of mass spectrometry, in a flowing helium afterglow at a gas temperature of 82°K. In fact He_3^+ was the dominant ion they observed. We have since been informed that deVries and Oskam have also identified the He_3^+ ion by mass spectrometry, in helium afterglows at gas temperatures near 77°K, and in addition discovered an He_4^+ ion in these same afterglows.[5] Recombination of these necessarily weakly bound heavier ions is likely to be a source of excited states of He_2 and thereby responsible for the visible band radiation that we observe at the lower gas temperatures.

When the gas temperature is maintained near 77°K the percentage of quenching is largest near 0.7 Torr and decreases with increasing pressure.

Preliminary observations at a gas temperature near 77°K and a pressure of several Torr using spectral resolution with the present system, at early afterglow times where some intensities are adequate for resolution and where the rapidly decaying 5876 Å ($3^3D - 2^3P$) atomic line can still be observed ($< \sim300$ μsec), indicate that the partial quenching during lasering is present and the percentage of quenching constant on the strongest molecular bands (e.g., 4439 Å [$4^3\Pi_u - 2^3\Pi_g$], 4725 Å [$4^1\Sigma_u^+ - 2^1\Pi_g$]) and apparently absent on the strongest atomic line (5876 Å).

The visible afterglow quenching by the infrared photons of the CO_2 laser appears related to recombination of the molecular ions present and is due to photon-induced changes in population of a state or states of a neutral molecule formed in recombination or a change in population of a state of the ion that contributes significantly to recombination. In either case the response to the infrared irradiation can be expected to be very rapid.

We wish to thank Professor H. J. Oskam for his preprint regarding mass analysis of the low gas temperature helium afterglow. We also wish to acknowledge the able technical assistance of W. Johnson, K. Kuehl, E. Boose, and J. James.

[1] J. P. Kaplafka, H. Merkelo, and L. Goldstein, Phys. Rev. Letters 21, 970 (1968).
[2] E. C. Beaty and P. L. Patterson, Phys. Rev. 137, 347 (1965).
[3] P. L. Patterson, J. Chem. Phys. 48, 3625 (1968).
[4] E. E. Ferguson, D. B. Dunkin, F. C. Fehsenfeld, and A. L. Schmeltekopf, Bull. Am. Phys. Soc. 13, 212 (1968).
[5] C. P. deVries and H. J. Oskam (unpublished).

EFFECTS OF INFRARED RADIATION ON GASEOUS PLASMAS

H. Merkelo, J. P. Kaplafka and L. Goldstein

University of Illinois,

Urbana, Illinois 61801

The purpose of this talk is to report briefly on a preliminary study of the interaction of infrared radiations with gaseous plasmas and on the possible applications of the resulting effects. Particular emphasis is laid on the use of gaseous plasmas for detection of pulsed infrared radiation, in the 9-11 micron wavelength range of CO_2 lasers, in the presence and/or absence of pulsed microwaves.

1. Generalities on the plasma media considered. Interaction with high frequency electromagnetic waves.

For simplicity we shall first consider weakly ionized, low pressure (<10 Torr) noble gases and/or some of their mixtures.

The plasmas are produced by electric fields, either pulsed or continuous, between electrodes. The configurations and locations of these electrodes are compatible with the propagation of infrared and microwave radiations through the plasma. The gases investigated are housed in containers that are transparent to the visible radiations they emit when excited.

We shall restrict generality for the purpose of this summary and consider only pulsed infrared in the 9 to 11 micron wavelength range (from CO_2 lasers) and microwaves in the 3-10 cm wavelength range.

1-1. A weakly ionized gas can be generally considered as a mixture of the gases of neutral atoms and the gases of the charged particles i.e., the free electrons, e, and the positive ions, i. These are in continuous interaction with each other. An equation of state for such a mixture can be written, to a good approximation, in a form expressing the law that the total gas pressure, p_t, in the volume containing this gas is the sum of the partial pressures of each constituent:

$$p_t = p_e + p_i + p_n$$

Or, according to the kinetic theory of gases,

$$p_t = n_e k T_e + n_i k T_i + N k T_g$$

where (n_e, T_e), (n_i, T_i) and (N, T_g) represent the density and temperatures of the electrons, ions and neutral gas atoms respectively. A certain fraction of the neutral atoms is in various excited, radiating or nonradiating, states[*].

---

[*]Strictly speaking we should also include a photon gas component. However, in view of circumstances here considered, we may neglect it with no great loss of understanding; the plasmas being transparent for most of their own radiations.

1

Any phenomenon observed results from the interaction between the constituents. Since we excite these gases by electrical means, the electrons and ions gain and accumulate kinetic energy from the field. There are a great number of collisions and these tend to randomize their motions. Thus their temperatures are higher than that of the neutral gas. The ions, having the mass of the atoms, are in excellent thermal contact with the neutral gas atoms and reach a temperature only very slightly higher than that of the neutral component. The electron gas, however, because of poor thermal contact with the heavy particles, reaches temperatures which may be several orders of magnitude higher than gas temperature. Thus the electrons are responsible for both ionization and excitation of the neutral gas atoms, which take place either directly from ground state or from some already excited state.

As long as energy is supplied to the electrons from an external field, this situation prevails and $T_e \gg T_i \sim T_g$. The electron temperature rise, or even better, the mean energy of the electron gas is limited by geometrical conditions. For these low pressure cases the geometrical conditions determine the loss rates for charged particles. Steady state conditions correspond to balance between charged particle production and losses. As long as ionization of the gas is taking place from the ground state of the atoms, the plasma is said to be active.

1-2. The inactive plasma; the afterglow.

When the source of excitation and maintenance of the plasma is removed, the electron temperature decreases toward the gas temperature chiefly by thermal contact with the neutral gas. Once the electron temperature decays sufficiently that there remain very few electrons to produce further ionization--even from excited (metastable) atoms--the plasma becomes inactive. Such a plasma decays in a length of time determined by the initial conditions and the loss rates of the remaining charges.

The charged particles are lost by volume recombination and surface recombination. The excited atoms decay rapidly ($< 10^{-6}$ sec) by radiation and those in nonradiating states by other processes. Those charges which do not undergo volume recombination reach the bounding surfaces by diffusion (a process highly dependent on geometrical conditions).

In what follows we shall be dealing with plasmas in low pressure, monatomic gases at ordinary temperatures. The degree of ionization i.e. $\frac{n_i}{N}$, can be as small as 10^{-4} to 10^{-8}. The charge density range is $\sim 10^9$ to 10^{12}/cc with gas densities of 10^{16} to 10^{18} atoms/cc.

On the other hand, from the point of view of electron temperature, we shall discuss two kinds of such plasmas:

a) where $\frac{T_e}{T_g} \gg 1$ as in continuously excited active plasmas

and b) where $\frac{T_e}{T_g} \sim 1$ as in the case of decaying inactive afterglowing plasmas.

Investigations of volume recombination processes in inactive helium plasmas, in a range of gas temperature from 77°K to 300°K, led us to irradiate such plasmas with low energy photons (hν < 0.15 eV). These were conveniently provided by CO_2 lasers.

1-3. Effect of CO_2 laser radiation on inactive plasmas produced in low pressure noble gases. The underlying thought for using the $\sim 10\mu m$ infrared quanta was essentially the following:

2

When an electron recombines with an atomic, positive ion, the neutralized ion may find itself on any of the possible excited states of the atom. Cascading toward the ground state, such an atom emits light quanta--some of which are in the visible part of the spectrum. The total light thus emitted by all atoms constitutes the afterglow, which can be spectrally resolved.

In the most probable process for such a recombination (which involves two electrons with one positive ion) there is high probability for the captured electron to find itself initially on a very high lying excited state of the atom.

Such a state is characterized by a high principal quantum number (n > 8,9,10,etc.). The energy level of such an excited state, E_x, is quite close to the ionization energy of the atom, E_i. If there are highly excited atoms, in adequate concentrations in levels where hv (of the infrared) > E_i-E_x, photo-ionization can occur and as a result the visible light output of the plasma should be quenched. This follows from the fact that if destroyed, the atoms excited into those high lying states are no longer available to feed the populations of lower energy states from which visible light originates. Also, since new electrons are liberated, the free electron density should be increased.

We have, therefore, two independent ways of testing this hypothesis:

1) Optical--by observing light quenching.

2) Electrical--by measuring a change in the electrical conductivity of the plasma.

2. Generality of the phenomenon.

In as much as any atomic specie has energy levels very near the continuum, it is to be expected that the phenomenon of visible light quenching by the infrared photons will occur in a variety of gases. While our first experiments (see Fig. 1) were performed with helium plasmas and infrared from a Q-switched CO_2 laser, we have been able to readily show that afterglows in all the noble gases at low pressures show the same effect. Figure 2 illustrates the effect.

It can be readily understood that in view of the relatively low photoionization cross sections, rather high intensity infrared radiation may be needed to observe the effects. The Q-switched, CO_2 laser is operated at about 1 kW of in-cavity peak power.

If high intensity beams are used then, in addition to single photon effects, multiple photon effects may also occur. Resonance excitation from a state of lower to a state of higher quantum number may occur with no photoionization. Moreover, at high power the infrared may interact directly with the free-electron gas of the plasma and this may be partly responsible for the phenomena observed.

2-1. Effect of CO_2 laser radiation on active discharge plasmas.

Pursuing the hypothesis that the infrared photons interact with atoms that are excited to states close to the ionization state, there is no reason to limit the plasmas to conditions of low electron temperature and density as in afterglow plasmas. Excited states close to the ionization limit must be populated continuously from ground state atoms in dc or ac discharge plasmas in the low pressure noble gases. However, these excited atoms are not in the same concentrations as in the afterglow plasmas where high principal quantum numbered states are populated in recombination of slow electrons with positive ions, and not from lower states. Here again the infrared radiation effect should be essentially independent of

3

the nature of the monatomic gas used.

In order to test spacially distinct regions of the plasma that differ in electron density, electron temperature and associated excited atom populations, a _cold_ cathode discharge tube of the type shown in Figure 3 was used. Two essentially different regions are considered: a) the cathode region and 2) the positive column region (nearly or fully developed).

Figures 4, 5 and 6 illustrate the generality of the effect of infrared by showing quenching produced on dc excited noble gases. It is seen that the Q-switched CO_2 laser radiation produces photoeffects in the visible region of the spectrum which are readily monitored with photomultipliers. Thus there is possible application to infrared-image transformation. The plasma response is rapid. Figure 7A and 7B show comparisons between the infrared signal as detected by a Ge:Au infrared detector (which requires a low temperature, 77°K, bath for operation) and as seen as perturbation of the light from a plasma at room temperature.

In view of the interaction between the electrons and the atoms and ions of the host gas, any light intensity variation in the plasma will be accompanied by a perturbation in the electron gas--directly or indirectly induced by the infrared. Perturbation in the electron gas implies change in either its density or its temperature or in both. In a dc discharge, current variation is observed during infrared irradiation. It occurs in the form of an increase in current. This current modulation is as readily observed and measured as the photoeffect. Figure 8 illustrates that it is as rapid and as faithful. We have to keep in mind, however, the fact that in comparing these, the current is an integrated effect over the whole discharge, whereas the visible light is sampled only from a small volume of the plasma, not all of which is traversed by the infrared beam. In any event, these are two independent ways of monitoring the CO_2-laser pulses. It is to be noted that the cross section of the infrared beam can be smaller or larger than that of the plasma. Gaseous plasmas are highly flexible media. They can be dimensioned and/or tailored to many specialized tasks.

One such task is the use of gaseous plasmas for the detection of both simultaneous or nonsimultaneous pulsed microwave and CO_2-laser infrared radiations.

2-2. _Pulsed microwave and infrared radiations in gaseous plasmas._

It is now well understood that microwaves, which can propagate in gaseous plasmas, interact directly and _only_ with the free electron gas of the plasma. The resulting physical phenomena can be used for detection and monitoring of microwave pulses.

Figure 9 shows the effects observed on such plasmas when pulsed microwaves and infrared radiations are propagated either simultaneously or one following the other.

A particularly interesting feature in the pulsed light outputs from the plasma is the fact that the infrared pulse quenches the light output regardless of the sign of the light intensity variation produced by the microwaves. Thus, the plasma possesses a discriminatory feature by which it can distinguish between pulses of infrared and microwave frequencies.

4

2-3. <u>Sensitivity as a detector of infrared radiation in the 9 to 11 micron range</u>.

Thus far no attempts have been made to determine or optimize the minimum detectable infrared power. Very preliminary estimates indicate that in tubes of the order of 1 cm^2 cross section, and for the plasma conditions discussed, dc current perturbations provide a sensitivity of the order of 50 microvolts per watt incident.

<u>Summary</u>.

It has been shown that infrared radiation in the 10 micron range interacts with gaseous plasmas of monatomic gases. The results of this interaction provide two independent methods (optical and electrical) for the detection of pulsed CO_2 laser radiation. The detection response time is relatively rapid (< 1μsec). No restrictions are imposed on the temperature of the gas hosting the plasma. The plasma medium can be dimensioned and shaped for particular tasks. The plasmas described can be used for monitoring both pulsed infrared and microwave radiations even when these are present in the plasma simultaneously. The study pursuing the identification and quantitative understanding of the basic processes involved in the observed effects is being continued.

It is a pleasure to acknowledge the important contributions of Mr. J. H. Hammond to this work.

5
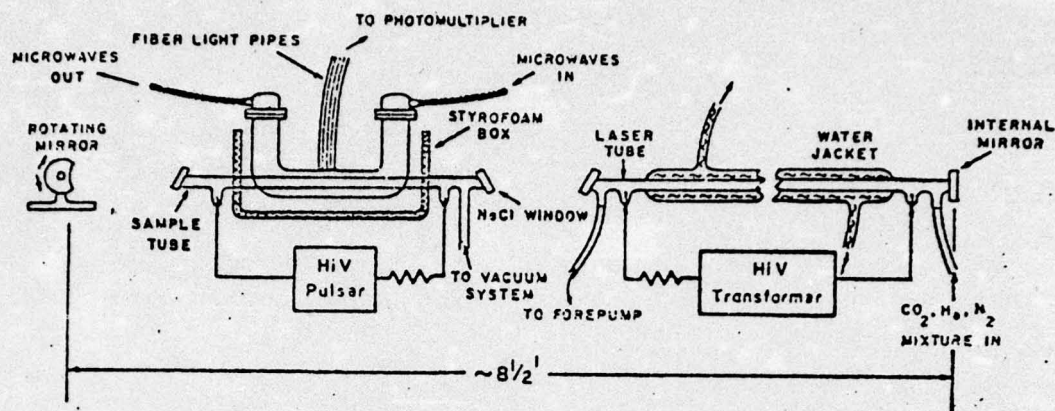
Figure 1. Simplified Schematic Cross-Section of Apparatus

Figure 2. Example of the quenching of the visible after-
glow of a helium plasma by a single infrared
pulse; 2 μsec/div.

6

Figure 3. DISCHARGE TUBE
FOR IR INTERACTION EXPERIMENTS
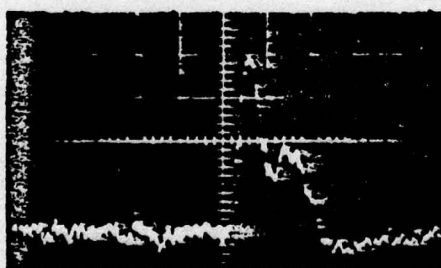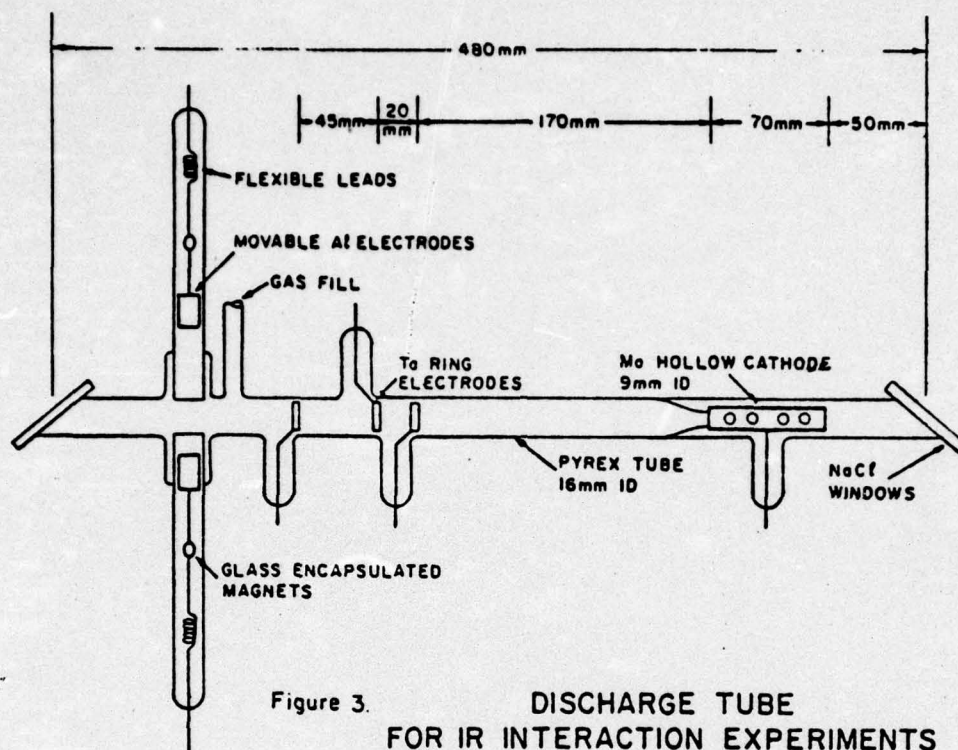
Figure 4. Quenching of visible emission by IR in a dc-excited He

discharge; 5μsec/div, 5mv/div.

Observations made near the cathode neck.

(Discharge 0.85 Torr helium, 14mA in 16mm dia tube,

hollow cathode)

7

Figure 5. Quenching of visible emission by IR in a dc-excited Ne
discharge ; 20 μsec/div, 5mv/div.
Observations made near the cathode neck.
(Discharge : 1.3 Torr neon, 3.1mA in 16mm dia tube,
hollow cathode.)
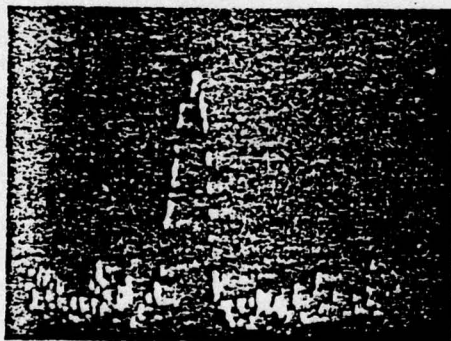
Figure 6. Quenching of visible emission by IR in a dc-excited Xe
discharge; 10μsec/div, 5mv/div
Observations made near the cathode neck.
(Discharge : 17 Torr xenon, 75mA in 16mm dia tube,
hollow cathode.)

8
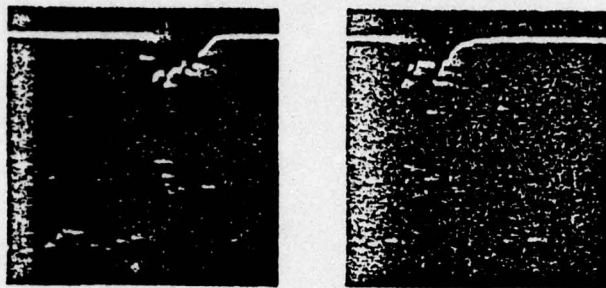
Figure 7A

Quenching of visible emission (bottom trace: 5μsec/div,
10mv/div) by IR (top trace: Ge:Au detector, 5μsec/div,
20mv/div) in a dc-excited He discharge. Observation
made near the cathode neck. (Discharge: 0.9Torr helium,
14mA in 16mm dia tube, hollow cathode.)
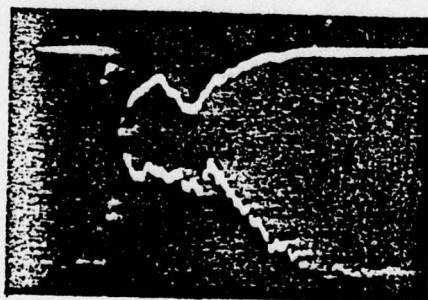
Figure 7B
(Same as Figure 7A, except 2μsec/div.)

9

10 μ sec/div   5 μ sec/div
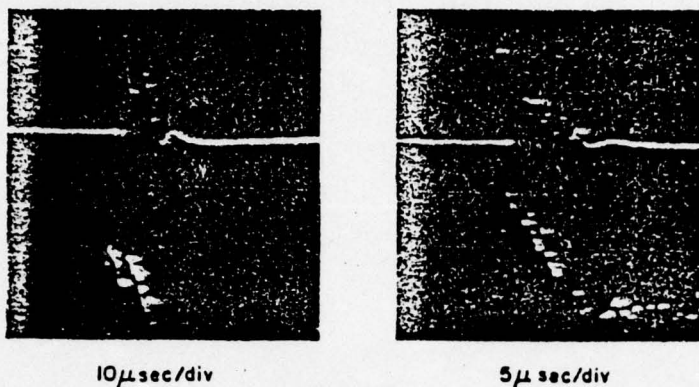
Figure 8.

Current perturbation (top trace: 10 μA/div) and quenching of plasma
emission (bottom trace: 10 μv/div) by IR in a dc-excited He plasma.
Observations made near the cathode neck. (Discharge: 1.3 Torr helium,
7.5 mA in 16 mm dia tube, hollow cathode.)
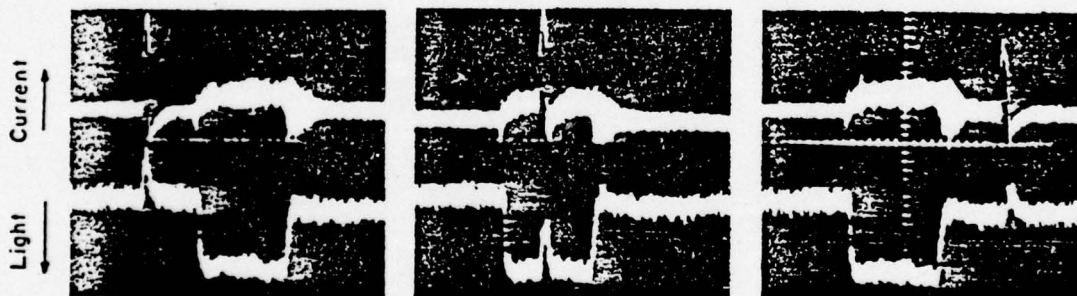
Figure 9.

Illustration of the independence of IR and microwave interactions with a dc-excited
plasma. Upper trace: discharge current; lower trace: plasma light emission.

10

Quenching of Radiation from Ionized Gases by Infrared Photons*

J. P. Kaplafka, H. Merkelo, and L. Goldstein
Gaseous Electronics Laboratory, University of Illinois, Urbana, Illinois 61801
(Received 28 June 1971)

Visible afterglow radiations from low-pressure weakly ionized inert gases are partially quenched during irradiation of the gases by the infrared produced with CO_2 lasers (photon energies ~ 0.1 eV). The most plausible interpretation of the effect appears to involve photoionization or photoexcitation of neutral atoms in excited states populated during the process of recombination.

The original observation of a partial quenching of visible emission from a plasma, induced by the infrared radiation of a CO_2 laser (operating near 10 μm), was reported for a weakly ionized helium afterglow plasma.[1] The quenching (as large as 50%) occurred on visible band radiations from the diatomic helium molecule and was interpreted as originating from photon-produced change of populations of states of a neutral or ionic helium molecule. However, the quenching has since been observed with afterglow plasmas of Ne, Ar, Kr, and Xe and at pressures where atomic ion recombination is known to dominate the volume loss rate. Additionally, quenching of atomic lines of helium has since been observed. Therefore, it is apparent that the effect is of much greater generality. Thus far, the most plausible interpretation is based on photoionization or photoexcitation of neutral species from energy states near the continuum.

Quenching of visible afterglow emission from room-temperature Ne, Ar, and Xe has been observed down to pressures on the order of 0.1 Torr but has not

been observed for pressures beyond a few Torr. As in the case of He, quenching in Ne and Ar was observed everywhere within the range where the gas temperature was varied (from 77 to 300 °K). Xe was tested in the range from 195 to 300 °K and exhibits quenching throughout this range. The source of the infrared has been either a mechanically Q-switched or a transversely excited, pulsed CO_2 laser. Figure 1 is for the purpose of illustration and shows a partial quenching of the total visible radiation from a Ne afterglow plasma at a gas pressure of 1 Torr on a 1-μsec/div time base. Although most observations were made with afterglow plasmas, similar observations have been made recently in dc discharges in He, Ne, Ar, and Xe. But in the case of the dc-discharge plasmas, there is less evidence to support an interpretation.

It is expected that the free-electron densities, in the afterglow plasmas studied, lie within the range of about 10^{12} to 10^9/cm³ during the afterglow times when quenching has been observed. There is always a certain "blind time" in the early afterglows where quenching is unobservable or very small. This blind time extends approximately to a time where the visible afterglow emission generally assumes a relative maximum—a time generally somewhere in a range from about 50 to 100 μsec after the 2-μsec active discharge.

There is evidence that the quenching is not primarily the result of heating of the free-electron gas by the infrared. On the other hand, such heating of the electron gas by electromagnetic radiation is easily produced at microwave frequencies and does result in quenching. This occurs because increasing the electron temperature reduces the recombination coefficient and thus quenches recombination emission. A short-duration exposure to microwave radiation at any time of the afterglow results in an increase in electron temperature and a decrease toward normal after the end of irradiation. The time characteristic of this decay toward normal is reflected in the re-
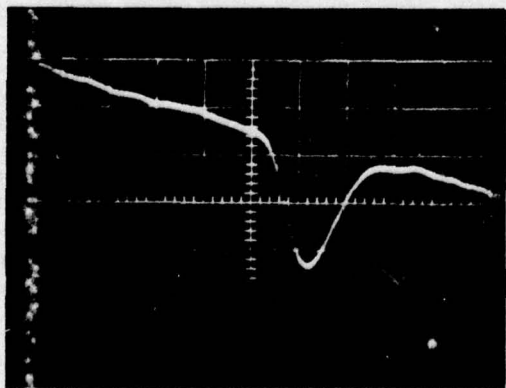

FIG. 1. Infrared-induced partial quenching of total visible radiation from a Ne afterglow plasma at a gas pressure of 1 Torr. The time base is 1 μsec/div and the time in the afterglow is approximately 600 μsec.
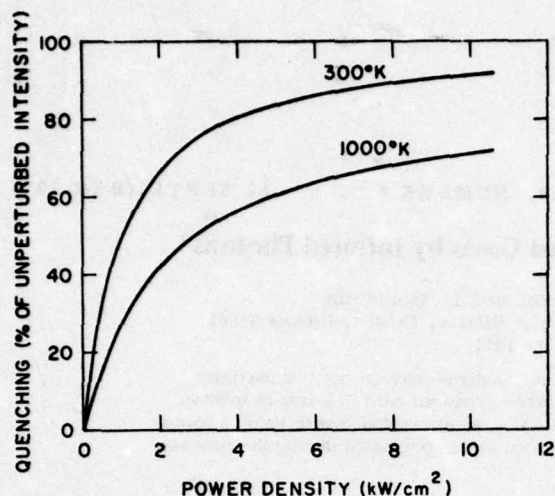
FIG. 2. Theoretical percentage of quenching of radiation originating from states of low quantum number vs the power density of the incident infrared radiation at two different temperatures of the free-electron gas. The free-electron density is taken to be $10^{10}/cm^3$.

covery of the afterglow light and depends on the relative mass of electron and atom and on the collision rates between electrons and atoms or ions. It is found experimentally that under many conditions, when power levels are adjusted to produce comparable amounts of quenching, the recovery of the afterglow light after infrared irradiation is very much faster than the recovery after microwave irradiation. This has been most easily observed with afterglow plasmas in Ne and Ar. As a result, the cause of the quenching by infrared appears to differ from the cause of quenching by microwaves.

The more intense of the visible emissions originate from energy states of low principal quantum number, e.g., when employing spectral resolution while observing quenching by infrared, the spectral lines that were studied originate from states of principal quantum number 3, 4, or 5. In many cases it is clear that populations in such levels cannot be altered directly by means of photoexcitation produced by absorption of single infrared photons from a CO_2 laser, because the separation between energy levels is greater than the photon energies, i.e., greater than ~0.1 eV. An appreciable amount of multiphoton photoexcitation does not appear to be a strong possibility at the infrared power densities employed.

Photon absorption by atoms in more highly excited states is possible since energy levels are less widely separated. The quenching phenomenon in afterglows of Ne, Ar, Kr, and Xe is favored at lower pressures where "collisional-radiative" recombination[2] is believed to describe the volume recombination process. In this type of recombination there is generally little direct formation of excited states of lower quantum number. Instead, the states of lower

quantum number are principally populated by cascade (both radiative and collisionally induced cascade) from excited states closer to the continuum. Therefore, reduction of populations of more highly excited states can result in reduced populations in lower levels and less emission from these levels.

In order for photoexcitation to occur at a significant rate there must be close coincidence between the infrared-photon energies of the laser and energy separations in the atoms. However, photoionization does not require such coincidences and actually results in the creation of a positive ion and free electron so that there can be no subsequent cascade of the atom until the ion again undergoes neutralization.

In order to investigate the credibility of the photoionization hypothesis, the approach of Bates, Kingston, and McWhirter in examining recombination[2] was adapted to a recombining system of atomic hydrogen ions and electrons in the presence of infrared radiation. It was postulated that all the laser energy appears at 10.6 μ and loss terms were included to account for the rates of photoionization from excited states sufficiently close to the continuum to be photoionized, i.e., those of principal quantum number, $n = 11$, 12, 13, etc. Then, by comparing the population of a given state of low quantum number, which was predicted with the infrared incident at a given intensity, to the population predicted with no infrared incident, the percentage of quenching expected on all emissions originating from the given state of low quantum number was obtained. By using the form of photoionization cross section for excited states of hydrogen derived by Menzel and Pekeris,[3] estimations were obtained of the percentage of quenching due to photoionization in terms of kW/cm^2 of the incident infrared beam. Some of the results are shown in Fig. 2. Actually, only an upper limit on the expected percentage of quenching is obtained in this manner because the calculation gives predictions valid after equilibrium has been established during infrared irradiations. It is expected that such is not the case when pulses of infrared power occur for only short duration. It should be noted that under the conditions indicated in Fig. 2 the estimated percentage quenchings on emissions originating from levels of $n = 3$, 4, 5 were nearly the same so only one curve is drawn. Quenching is observed at power densities contained within the range on Fig. 2, although quantitative agreement is not implied. It is also of interest to note that no lines in an afterglow have yet been observed which show an enhancement rather than a quenching. Figure 2 suggests a decrease in the percentage of quenching as the temperature of the free electrons increases. A decrease is observed when the temperature of the free-electron gas is deliberately increased for a short period of the afterglow, covering the time when the infrared is incident. The method used to selectively increase the electron

temperature has been application of microwave radiation. Moreover, the largest percentages of quenching for a given level of infrared have generally been observed with the plasma in a liquid-nitrogen bath.

The observed disappearance of the quenching in afterglows of Ne, Ar, and Xe with increase in pressure can be due to the fact that the dissociative recombination of the diatomic molecular ions—favored as pressure increases—does not result in the formation of atoms in excited states sufficiently close to the continuum for photoionization or significant photoexcitation to occur, if the majority of such ions are vibrationally unexcited. He is the exception in the sense that quenching does occur at pressures where recombination with a diatomic molecular ion dominates recombination loss. But the observation of quenching on visible bands of He_2 is not surprising because the very existence of bands indicates that the recombination is not directly dissociative.

It would be difficult to ascertain whether or not photoionization takes place by seeking to record an increase in density of free electrons during infrared irradiation. The difficulty is that estimates, using the recombination model referred to earlier, indicate the sum of populations in excited levels subject to appreciable photoionization is generally a few orders of magnitude less than the corresponding density of free electrons. Moreover, a small increase in free-electron density could occur even in the presence of photoexcitation alone, by means of ionizing collisions with free electrons. Such collisions normally play an important part in determining the populations of highly excited states.

Identification of the origin of the quenching phenomenon requires further evidence.

[1] J. P. Kaplaфka, H. Merkelo, and L. Goldstein, Appl. Phys. Letters 15, 113 (1969).
[2] D. R. Bates, A. E. Kingston, and R. W. P. McWhirter, Proc. Phys. Soc. (London) 267A, 297 (1962).
[3] D. H. Menzel and C. L. Pekeris, Monthly Notices Roy. Astron. Soc. 96, 77 (1935).

THEORETICAL ANALYSIS OF THE INFRARED SENSITIVITY OF
ATOMIC HYDROGEN AND HELIUM AFTERGLOW PLASMAS

BY

BARRY GENE GROSSMAN

B.S., University of Illinois, 1971

THESIS

Submitted in partial fulfillment of the requirements
for the degree of Master of Science in Electrical Engineering
in the Graduate College of the
University of Illinois at Urbana-Champaign, 1973

Urbana, Illinois

ACKNOWLEDGMENT

The author wishes to acknowledge the advice given by his graduate
advisor H. Merkelo and to thank the Office of Naval Research and the National
Science Foundation for their financial support.

PREFACE

This text comprises an analysis of the atomic processes occurring in atomic hydrogen and helium as they pertain to the population densities of excited atomic energy levels. Three-body collisional ionization and recombination, collisional excitation and de-excitation between discrete levels, radiative recombination, and spontaneous transitions are considered along with the effects of an external source of infrared photon flux.

Detailed calculations of the population densities performed both with and without the infrared radiation indicate a decrease of densities due to photoionization of highly excited states by the infrared. From the calculated densities, quantitative predictions are made for the percentage quenching of visible light emission which originates from low-lying states in hydrogen and helium afterglow plasmas when subjected to infrared radiation at a number of wavelengths.

Infrared wavelengths in the range 1.46 μm to 32.8 μm with a constant intensity of 1.0 kW/cm^2 are considered. Calculations for hydrogen at a temperature of 300° K and a free electron density of 10^{10}/cm^3 are performed. Helium calculations were done for temperatures of 300° K, 500° K, and 1000° K with electron densities of 10^8/cm^3, 10^9/cm^3, 10^{10}/cm^3 and 10^{11}/cm^3.

TABLE OF CONTENTS

INTRODUCTION

There is experimental evidence of the effects of infrared radiation at 10.6 μm on gaseous plasmas [1], [2], [3] and [4]. One such effect is the quenching of visible afterglow light in plasmas subjected to an infrared laser pulse, indicating a reduction of population densities on lower excited atomic energy levels. At present, the hypothesis is that the quenching is indirectly due to photoionization of highly excited states although the possibility also exists that the quenching may, to some degree, be due to infrared heating of the free electrons. Since an increase in electron temperature decreases the recombination coefficient and thus produces light quenching, quantitative predictions of quenching due to photoionization were needed.

The present text is a theoretical analysis of the atomic processes determining the various population densities, and the change in densities due to a steady state presence of infrared radiation at a variety of wavelengths. From the population densities calculated, percentage quenching of visible light can be calculated. This is done for atomic hydrogen and helium.

The reaction rates governing the population density of excited levels for helium are derived from those predicted for hydrogen and the calculation of excited level populations follows the procedure presented in [5] with modification made for additional loss mechanisms such as collisional de-excitation at the walls of the discharge tube and photoionization by infrared photons.

Free electron densities in the range $10^8/cm^3$ - $10^{11}/cm^3$ and electron temperatures from $300°$ K - $1000°$ K are considered.

Explanations of the basic procedure for analysis of hydrogen and helium are identical except where noted.

I. HYDROGEN AND HELIUM ATOMS AND THEIR AFTERGLOWS

The hydrogen atom consists of one bound electron orbiting a nucleus of charge +1. The energy level diagram is shown in Figure 1. Using the free electron energy as a zero reference point, the ground state energy is -109678 cm^{-1}, with the first excited level at -27419 cm^{-1}. The measured energy levels are very closely approximated by the Bohr formula in which degenerate levels of a principal quantum number are taken together.

The Bohr formula is:

$$\text{ENERGY} = \frac{109678}{p^2} \text{ cm}^{-1} , \qquad (1.1)$$

where p = principal quantum number.

Since the energy spread between degenerate levels is much smaller than the difference in energy between levels of consecutive principal quantum numbers, these levels are grouped together and are considered as one level. The population of that level is then assumed to be equally distributed among the degenerate states.

The helium atom has two bound electrons surrounding a positive nuclear charge of +2. Figure 2a illustrates the ground state condition in which each electron is at -318066 cm^{-1}. Figure 2b shows the effects of exciting one of the electrons, called here e'. As e' is excited from the ground state, e forms an orbit closer to the nucleus at -437827 cm^{-1}. The energy lost by e is gained by e', which then requires a total energy of only -198305 cm^{-1} to be ionized. Thus, since e remains in the new ground state (actually it moves slightly lower in energy as e' increases in energy) until e' is fully excited to the ionization energy, e' can be considered to be part of a one electron type of atom with a ground state energy of -198305 cm^{-1}.

As e' becomes increasingly excited, the interaction between the two
electrons decreases and the shielding of one of the protons by e makes it
appear that e' is part of a hydrogen atom. Comparison between tabulated
helium energy levels [6] and those for hydrogen calculated by Equation (1.1)
for p = 4 show an error of less than 0.1%. This error decreases with
increasing p. Furthermore, the energy spread between degenerate levels
decreases with increasing p, allowing the approximation to be made that for
levels p ≥ 4, helium can be considered basically hydrogen-like in energy
structure. Below p = 4, the energy spread between degenerate levels is
increasing, necessitating the grouping of these levels by angular momentum
quantum number. Thus, for p less than four in helium the levels are treated
as approximately hydrogen-like but treated as separate levels. For p ≥ 4
the levels are considered to be essentially hydrogen-like with the
degenerate levels grouped together by principal quantum number.

Both hydrogen and helium afterglow plasmas are treated in this text.
The afterglow plasma consists of free electrons, ions, excited atoms, and,
predominantly, neutral atoms in the ground state, i.e., those constituents
remaining after the removal of the accelerating electric field in the
discharge. Once the field is removed, the electron temperature decays
toward the gas temperature by thermal contact with the neutral gas until the
two temperatures are approximately equal.

Principle recombination mechanisms for the free electrons and ions for
atomic hydrogen and helium are

$$X^+ + e + e \rightarrow X^* + e \qquad (1.2a)$$

$$X^+ + e \rightarrow X^* + h\nu . \qquad (1.2b)$$

Reaction (1.2a), which is a three-body collisional recombination into an excited level, predominates in the early part of the afterglow where the free electron and ion densities are high. The reaction of (1.2b), in which the excess energy of the combining electron is given off as radiation, predominates in the later afterglow. Thus, both reactions must be considered simultaneously as presented in [1]. As previously mentioned, electron densities of $10^8/cm^3$ – $10^{11}/cm^3$ and temperatures of 300° K – 1000° K are investigated.

ATOMIC HYDROGEN ENERGY LEVELS
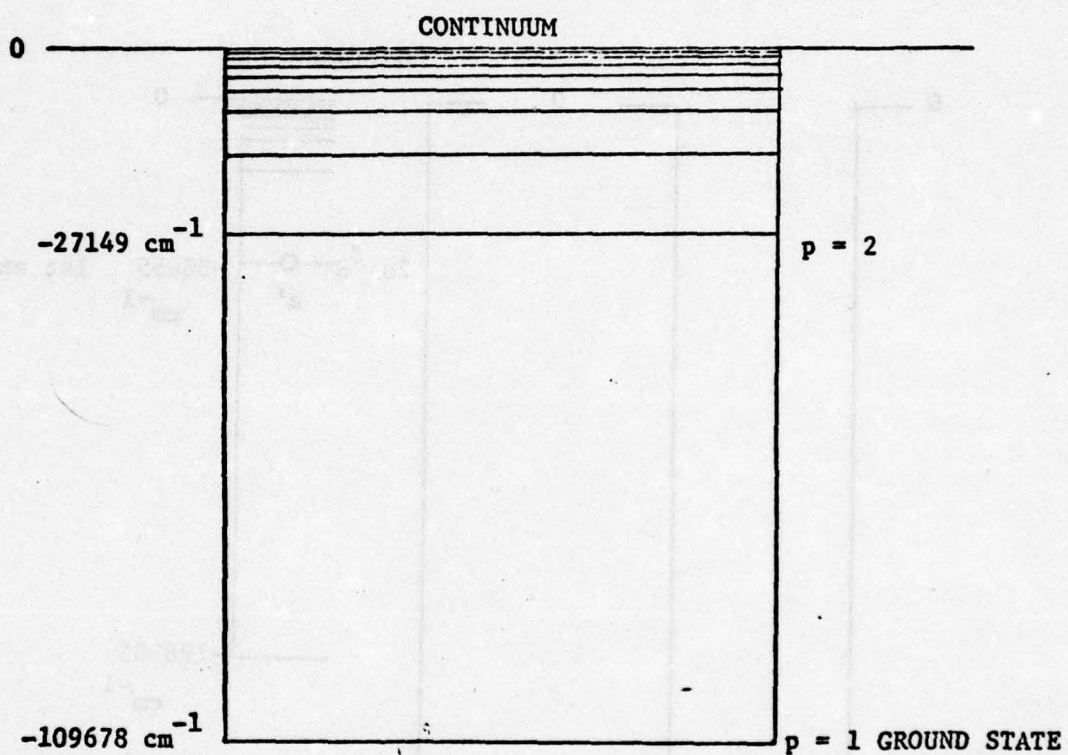
Figure 1.

ATOMIC HELIUM ENERGY LEVELS

CONTINUUM

0   0   0

2s ^{3}S —o— -38455 1st excited level
e'   cm^{-1}

-198305
cm^{-1}

e   e'
o   o -318066 cm^{-1}

GROUND STATE
ATOM
(a)

e
-437827 o
cm^{-1}

SINGLY EXCITED ATOM
(b)
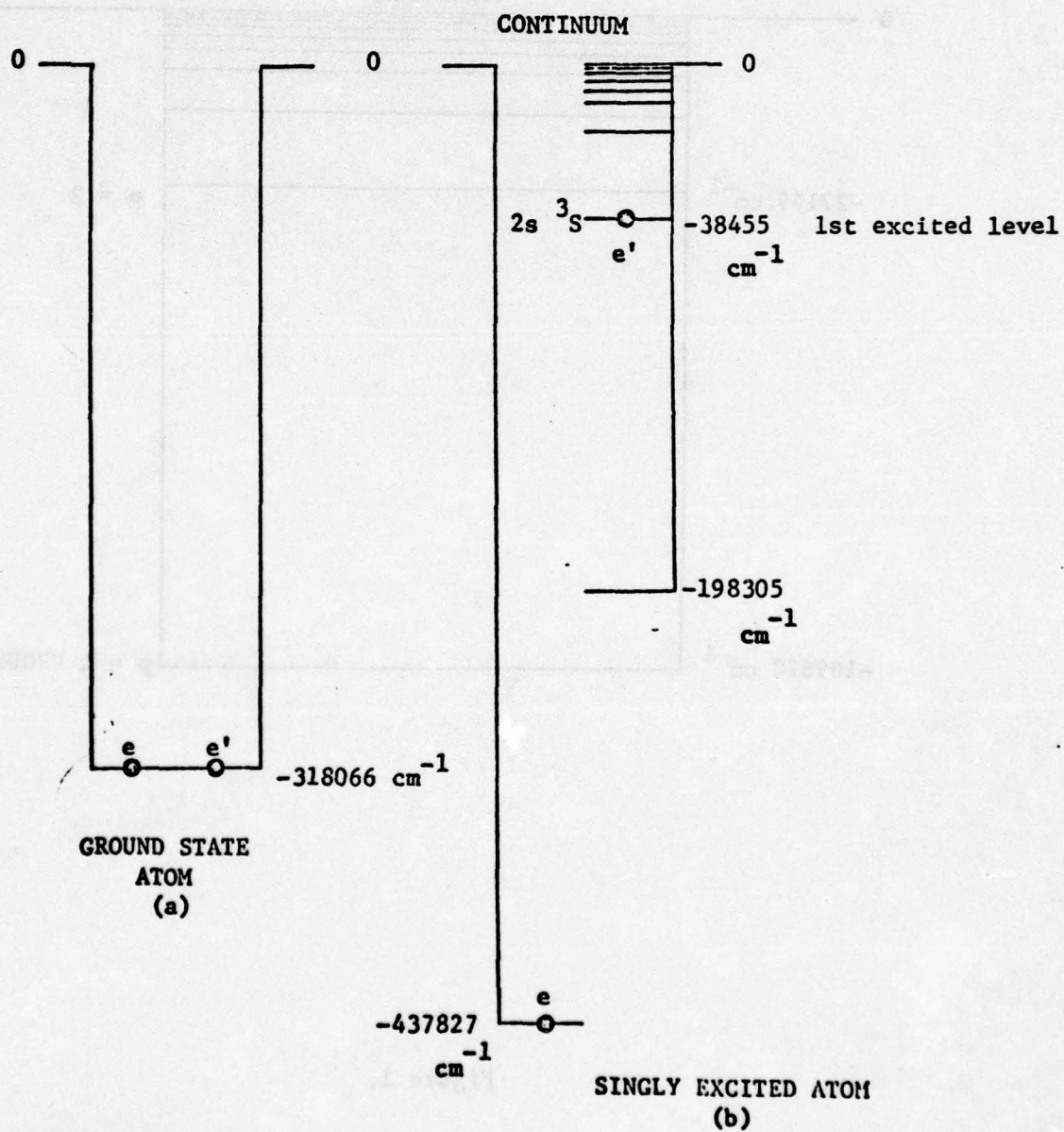
Figure 2.

II. METHOD OF CALCULATION OF DENSITIES

The calculation of light quenching requires precise predictions of population densities of excited states. The method used follows that given in [5] in presenting the collisional-radiative recombination theory for hydrogen and hydrogen-like ions. The following method is written for singly-charged positive ions. It is also restricted to situations in which the free electron density is equal to the ion density. Furthermore, in the following, p and q refer to principal quantum numbers for hydrogen and level numbers in the case of helium in which levels 2 and 3 are broken into their degenerate levels.

Let $K(c,p)$ be the rate coefficient for the three-body recombination process

$$N^+ + e + e \rightarrow N(p) + e \quad , \qquad (2.1)$$

where N^+ = the hydrogen or helium ion

$N(p)$ = excited neutral atom in state p

e = free electron.

For the reverse process of ionization, the rate coefficient $K(p,c)$ describes

$$N(p) + e \rightarrow N^+ + e + e \quad . \qquad (2.2)$$
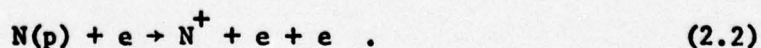
$K(p,q)$ is the rate coefficient for collisional excitation or de-excitation as described by

$$N(p) + e \rightarrow N(q) + e \quad , \qquad (2.3)$$

and $\beta(p)$ is the rate coefficient for radiative recombination into level p described by

$$N^+ + e \rightarrow N(p) + h\nu \ . \tag{2.4}$$
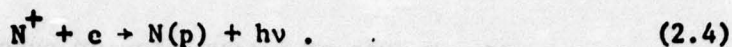
$A(p,q)$ is the spontaneous transition rate for the process

$$N(p) \rightarrow N(q) + h\nu \qquad p > q \ . \tag{2.5}$$
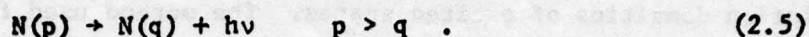
A uniform distribution among degenerate states of a level number is assumed.

Assuming electronic transitions due to heavy particle collisions are negligible, the plasma optically thin, and ignoring boundary effects, the rate of change of population of level p can be written as

$$\frac{dn(p)}{dt} = -n(p)[n(c)K(p) + a(p)] + n(c) \sum_{q \neq p} K(q,p)$$

$$+ \sum_{q>p} n(q)A(q,p) + n(c)^2 [K(c,p) + \beta(p)] \ , \tag{2.6}$$

where $n(p)$ = population density of level p

$n(c)$ = free electron density

$K(p) = K(p,c) + \sum_{q \neq p} K(p,q)$

$a(p) = \sum_{q<p} A(p,q) \ .$

Denoting by $n_E(p)$ the number density in level number p in Saha equilibrium, letting

$$\rho(p) \equiv n(p)/n_E(p) \ , \tag{2.7}$$

and using the relations required for detailed balancing

$$n_E(q)K(q,p) = n_E(p)K(p,q)$$

$$n(c)K(c,p) = n_E(p)K(p,c) \ , \tag{2.8}$$

Equation (2.6) can be put in the form

$$\frac{\dot{n}(p)}{n_E(p)} = -\rho(p)[n(c)K(p) + a(p)] + \sum_{q \neq p} \rho(q)n(c)K(p,q)$$

$$+ \sum_{q>p} \rho(q) \frac{n_E(q)}{n_E(p)} A(q,p) + n(c)K(p,c) + \frac{n^2(c)}{n_E(p)} \beta(p) : \qquad (2.9)$$

an infinite set of coupled differential equations.

For most levels and typical values of $n(c)$ and T,

$$n_E(p) \ll n(c) \qquad p \neq 1$$

and

$$\dot{n}(p) \ll n(c) \qquad p \neq 1 .$$

Provided that the temperature is not high enough to permit substantial electron pumping from the ground state, the total population density of excited states is much less than the free electron density. Under these conditions and using the fact that radiative and collisional processes are very rapid, the excited state population densities quickly reach an equilibrium value before $n(c)$, the free electron density, can change appreciably. Thus a given $n(c)$ and T uniquely determine the excited state populations. This simplifies the problem because $\dot{n}(p)$ for all excited levels in Equation (2.9) can be set to zero, resulting in a set of coupled linear equations instead of differential equations. Furthermore, when p is large enough, collisional processes dominate and $n(p)$ can be assumed to be equal to the Saha density. Designating this critical level s, it is then only necessary to work with s-1 equations, since $n(1)$ is assumed known, thus avoiding an infinite matrix. The initial choice for s is somewhat arbitrary and determines the accuracy of calculations. It is first assumed, then the

equations are solved and checked to see that $\rho(s)$, which is $n(s)/n_E(s)$, is sufficiently close to unity. The value of $s = 28$ was chosen for hydrogen and helium. Adding also a term for de-excitation into the ground state by collision with the walls of the discharge tube and loss due to photoionization due to infrared photons, the final form of Equation (2.9) to be solved is:

$$\rho(p)[n(c)K(p) + a(p) + D(p) + IR(p)]$$

$$- \sum_{\substack{q \neq p \\ \leq s}} \rho(q)n(c)K(p,q) - \sum_{\substack{q > p \\ \leq s}} \rho(q) \frac{n_E(q)}{n_E(p)} A(q,p)$$

$$= n(c)[K(p,\sigma) + K(p,c)] + \frac{n^2(c)\beta(p)}{n_E(p)} + \sum_{q > s} \frac{n_E(q)}{n_E(p)} A(q,p) \qquad (2.10)$$

for $p \neq 1$

$p \leq s = 28$,

where $K(p,\sigma) = \sum_{q > s} K(p,q)$

$D(p) =$ de-excitation rate with walls

$IR(p) =$ IR photoionization loss rate.

The percentage of light quenching that occurs is calculated for the levels from which the spontaneous emission is in the visible wavelength range. For hydrogen, these are levels 2 through 6, for helium, level numbers 11 through 14 which correspond to principal quantum numbers 3 - 6. Since the light from a level p is given by

$$I = n(p)A(p,q)h\nu_{pq} , \qquad (2.11)$$

where $I =$ intensity

$n(p) =$ density of level p

$$p,q = \text{levels, where } q < p$$

$$A(p,q) = \text{spontaneous transition rate}$$

$$h = \text{Planck's constant}$$

$$\nu_{pq} = \text{frequency of emitted light,}$$

the percentage quenching of light is proportional to the change in population density and is given by

$$\frac{n(p)\Big|_{IR=0} - n(p)\Big|_{IR\neq0}}{n(p)\Big|_{IR=0}} \times 100 = \begin{array}{l}\text{PERCENT} \\ \text{QUENCHING}\end{array} \quad . \quad (2.12)$$

The equations are solved by the Gauss-Seidel method for solving simultaneous linear equations. Consider an example of three equations,

$$A_{11}\rho_1 + A_{12}\rho_2 + A_{13}\rho_3 = C_1$$
$$A_{21}\rho_1 + A_{22}\rho_2 + A_{23}\rho_3 = C_2 \qquad (2.13)$$
$$A_{31}\rho_1 + A_{32}\rho_2 + A_{33}\rho_3 = C_3$$

arranged in the following form:

$$\rho_1 = \frac{C_1 - A_{12}\rho_2 - A_{13}\rho_3}{A_{11}} \qquad (2.14a)$$

$$\rho_2 = \frac{C_2 - A_{21}\rho_1 - A_{23}\rho_3}{A_{22}} \qquad (2.14b)$$

$$\rho_3 = \frac{C_3 - A_{31}\rho_1 - A_{32}\rho_2}{A_{33}} \quad . \qquad (2.14c)$$

It is assumed that $\rho_1^0 = \rho_2^0 = \rho_3^0 = 0$, where the subscript refers to the variable number and the superscript refers to the number of iterations.

These are put into (2.14a) giving ρ_1^1, then ρ_1^1 and ρ_3^0 are put into (2.14b) giving ρ_2^1, and finally ρ_1^1 and ρ_2^1 are put into (2.14c) giving ρ_3^1.

This process is repeated until

$$M^k \equiv \max \left| \rho_i^{(k)} - \rho_i^{(k-1)} \right| < 10^{-6} , \qquad (2.15)$$

i.e., the maximum value of the difference between successive iterations of the value of ρ for all ρ's is less than 10^{-6}.

III. ATOMIC COEFFICIENTS

The Saha equilibrium density of excited states is that density which is predicted for a closed system in thermodynamic equilibrium. From Fowler [7], the Saha density for an atom in state p is:

$$n_E(p) = \frac{n^2(c) g_0(p)}{2 g_1} \left(\frac{h^2}{2\pi m k T} \right)^{3/2} \exp \left(\frac{I_p}{kT} \right) \qquad (3.1)$$

where $n_E(p)$ = Saha density of state p

$n(c)$ = free electron density

$g_0(p)$ = degeneracy of atom in state p

g_1 = degeneracy of ion energy level

h = Planck's constant

m = electron mass

T = equilibrium temperature

k = Boltzmann's constant

I_p = energy needed to ionize the atom from state p

π = 3.1415 . . . .

Hydrogen has a degeneracy of $2p^2$ for an atom with its electron in level p, and the degeneracy of the positive ion is 1. The ionization energy from level p in inverse centimeters is

$$I_p = \frac{109678}{p^2} \text{ cm}^{-1} . \qquad (3.2)$$

Substituting these values and the constants into Equation (3.1) results in

$$n_E(p) = 4.2 \times 10^{-16} \times n^2(c) \times p^2 \times T^{-3/2} \exp[157859/p^2 T] . \qquad (3.3)$$

Thus, given an electron density and temperature, the Saha density for the various levels are computed.

The singly charged He$^+$ ion has a degeneracy of 2. The atom with one electron in the ground state and the other in state p has a degeneracy of $4p^2$ if p is taken as the group of degenerate states with principal quantum number p. For those degenerate levels which must be considered separately, the degeneracy is $2J + 1$, where J is the total angular momentun quantum number. Thus the formula for computing the Saha density for helium is

$$n_E(p) = 1.05 \times 10^{-16} \times n^2(c) \times g_0(p) \times T^{-3/2} \exp[I(p)/kT] \ . \qquad (3.4)$$

The values of $g_0(p)$ and $I(p)$ are stored in the array EHE(35,4) and are used in the program for calculating the Saha densities for helium – SAEQP, which is presented in the appendix. The calculated densities are fed into the main program at execution time.

The compilation of spontaneous transition probabilities for hydrogen is relatively straightforward. For transitions between levels less than twenty-one, the tabulated values [8] were used. Transitions from levels greater than twenty were calculated by use of the formula presented in [9] for the asymptotic oscillator strength

$$f(p,q) = \frac{2^6}{3\pi\sqrt{3}} \left(\frac{1}{p^2} - \frac{1}{q^2} \right)^{-3} \frac{1}{p^3} \frac{1}{q^3} \frac{1}{g_p} \qquad (3.5)$$

where p,q = the two levels

g_p = the degeneracy of level p = $2p^2$.

The spontaneous transition probability is then given by [8] as

$$A(q,p) = \frac{6.67 \times 10^{15}}{\lambda^2} \frac{g_p}{g_q} f(p,q) \ , \tag{3.6}$$

where g_p, g_q = degeneracy of levels p,q

$f(p,q)$ = oscillator strength

λ = wavelength of emitted light.

With the use of Equation (3.5), and the appropriate conversion from λ to energy, Equation (3.6) becomes

$$A(q,p) \simeq \frac{1.29 \ ^3 q(E_q - E_p)^2}{(q^2 - p^2)^3} \qquad q > 20 \ , \tag{3.7}$$

where $(E_q - E_p)$ = energy difference of levels q and p in cm^{-1}.

Helium presents a difficult problem due to the scarcity of published values for transitions between highly excited states. For transitions to level numbers eleven and below from higher levels up to fourteen or twenty, published values [8] and [10] were used. Transitions to these levels from higher excited states were calculated with the use of a form for the asymptotic oscillator strength as presented in [11]

$$f(p,q) \sim \frac{1}{q_3} \ . \tag{3.8}$$

This was then substituted into Equation (3.6) and normalized for each level to the rate for the highest level published.

This resulted in the following equations:

$$A(q,p) = C_p \times g_p \times (E_q - E_p)^2/q^5 \tag{3.9}$$

$$C_p = \frac{A'(q,p)q^5}{g_p(E_q - E_p)^2} \,, \tag{3.10}$$

where C_p = normalizing constant for level p

$A'(q,p)$ = rate from the highest of known levels

and g_p, E_q and E_p are as previously defined.

The calculated values of C_p are given in Figure 3.

The spontaneous transition rates between higher excited levels were assumed to be approximately the same as those for hydrogen. Use was made of the published and asymptotic values previously mentioned for hydrogen atoms. The rates for helium were tabulated and calculated and then stored by use of the program SPONA. This program punches the rates onto cards for use by the main program and is presented in the Appendix.

The radiative recombination coefficient describes the rate at which free electrons are captured into excited atomic states. Bates [5] gives the general formula for hydrogen as

$$\beta(a,T) = \frac{w_a}{w_i}\left\{\frac{\sqrt{2}\,\exp(I_a/kT)}{c^2\pi^{1/2}(mkT)^{3/2}}\right\}K \,, \tag{3.11}$$

where w_a, w_i = degeneracy of the atomic state a, and the ion

I_a = ionization energy from state a

$$K = \int_{I_a}^{\infty} (h\nu)^2\sigma_{ai}(\nu)\,\exp\left\{\frac{-h\nu}{kT}\right\}d(h\nu) \,,$$

with $h\nu$ = energy transferred to electron

$\sigma_{ai}(\nu)$ = photoionization cross section for state a

k = Boltzmann's constant.

m = electron mass

h = Planck's constant

T = temperature

c = speed of light.

Seaton [12] gives the photoionization cross section as

$$\sigma_{n1}(\nu) = \frac{2^6 \alpha \pi a_0^2 n}{3\sqrt{3}} (1 + n^2 \epsilon)^{-3} g_{11}(n, \epsilon) , \qquad (3.12)$$

with n = principal quantum number in hydrogen

α = fine structure constant

a_0 = Bohr radius

g_{11} = Kramers-Gaunt factor

ϵ = excess energy of ejected electron.

Using (3.11) and (3.12) for hydrogen, where $w_a/w_i = 2n^2$ results in

$$\beta(n, T) \approx \frac{D\lambda^{1/2}}{n} x_n S_n(\lambda) , \qquad (3.13)$$

where $D = \frac{2^6}{3} \left(\frac{\pi}{3}\right)^{1/2} \alpha^4 c a_0^2 = 5.197 \times 10^{-14} \text{ cm}^3 \text{ sec}^{-1}$

$\lambda = hRc/kT = 157890/T$

$x_n = \lambda/n^2 = 157890/n^2 T$.

and, $S_n(\lambda) \equiv \int_0^\infty \frac{g_{11}(n, \epsilon) \exp(-x_n U)}{(1 + U)} \, dU$

(where $U = n^2 \epsilon$).

For helium, the radiative recombination coefficient was approximated by (3.13) with w_a/w_i replaced with the appropriate helium ratios, and n replaced

with the effective quantum number resulting in

$$\beta(p,T) = \frac{Dg_p \lambda^{1/2} x_n S_n(\lambda)}{4n_{eff}^3} \qquad (3.14)$$

where now, p = level number

g_p = degeneracy of level number p

n_{eff} = effective quantum number for level p.

Seaton [12] gives an asymptotic expansion for g_{11}

$$g_{11}(n,\varepsilon) = 1 + 0.1728 \, n^{-2/3}(U + 1)^{-2/3}(U - 1)$$

$$- 0.0496 \, n^{-4/3}(U + 1)^{-4/3}(U^2 + 4U/3 + 1) + \ldots \qquad (3.15)$$

Substituting (3.15) into $S_n(\lambda)$ results in

$$S_n(\lambda) = S^{(0)}(x_n) + \lambda^{-1/3} S^{(1)}(x_n) + \lambda^{-2/3} S^{(2)}(x_n) + \ldots, \qquad (3.16)$$

where $S^{(0)}(x) = \exp(x) \, E_i(x)$

$$S^{(1)}(x) = 0.1728 \, X_1(x)$$

$$S^{(2)}(x) = -0.0496 \, x^{2/3} \, X_2(x)$$

and $\quad E_i(x) = \int_x^\infty \frac{e^{-\nu}}{\nu} \, d\nu$

$$X_1(x) = \int_0^\infty (U + 1)^{-5/3}(U - 1) \, e^{-xU} \, dU$$

$$X_2(x) = \int_0^\infty (U + 1)^{-7/3}(U^2 + 4U/3 + 1) \exp(-xU) \, dU \ .$$

For $0.02 \leq x_n \leq 20$, values for $xS^{(0)}$, $xS^{(1)}$, and $xS^{(2)}$ were interpolated from Seaton's table of calculated values. Values of $x_n > 20$ were calculated by his approximate formulas

$$xS^{(0)} \doteq 1 + 1/x + 2!/x^2 + 3!/x^3 + 4!/x^4$$

$$xS^{(1)} \doteq -0.1728 \; x^{1/3}\left[1 - \frac{8}{(3x)} + \frac{70}{(3x)^2} - \frac{800}{(3x)^3} + \frac{11440}{(3x)^4}\right]$$

$$xS^{(2)} \doteq -0.0496 \; x^{2/3}\left[1 - \frac{3}{3x} + \frac{32}{(3x)^2} - \frac{448}{(3x)^3}\right] \quad . \tag{3.17}$$

The values of $\beta(p,T)$ for hydrogen were calculated in the program BETA as shown in the Appendix and then by comparison with (3.14), converted to give those for helium.

Gryzinski [13] gives as the cross section for collisional ionization of an atom:

$$Q(p,c) = \int_0^\infty f^1(v_e)Q'(U) \; dv_e \; , \tag{3.18}$$

where $Q(p,c)$ = cross section for electron in orbit p

$f^1(v_e)$ = velocity distribution of the orbital electron

$Q'(U)$ = Gryzinski's derived formula

and, $\qquad f^1(v_e) = 2\delta[v_e - (2E_1/m)^{1/2}] \tag{3.19}$

where E_1 = kinetic energy of orbital electron

m = electron mass.

He gives $Q'(U)$ as

$$Q'(U) \equiv \frac{6.56 \times 10^{-14}}{U^2} \; g[E_2/U, \; E_1/U] \; , \tag{3.20}$$

where U = ionization energy from the level p

E_1 = kinetic energy of orbital electron in p

E_2 = energy of incident electron

and,

$$g[E_2/U_p, E_1/U_p] = \left(\frac{v_2^2}{v_1^2 + v_2^2}\right)^{3/2} \left\{\frac{2}{3}\frac{E_1}{E_2} + \frac{U_p}{E_2}\left(1 - \frac{E_1}{E_2}\right) - \left(\frac{U_p}{E_2}\right)^2\right\} \begin{array}{l} \text{for} \\ U + E_1 \leq E_2 \end{array}$$

$$= \left(\frac{v_2^2}{v_1^2 + v_2^2}\right)^{3/2} \left\{\frac{2}{3}\left[\frac{E_1}{E_2} + \frac{U_p}{E_2}\left(1 - \frac{E_1}{E_2}\right) - \left(\frac{U_p}{E_2}\right)^2\right]\right.$$

$$\times \left.\left[\left(1 + \frac{U_p}{E_1}\right)\left(1 - \frac{U_p}{E_2}\right)\right]^{1/2}\right\} \begin{array}{l} \text{for} \\ U + E_1 \geq E_2 \end{array}. \quad (3.21)$$

In plasmas, E_2 is not a single value but is a distribution which is assumed to be:

$$f(\epsilon)d\epsilon = \frac{2\pi}{(\pi kT)^{3/2}} \epsilon^{1/2} \exp(-\epsilon/kT)\,d\epsilon \quad (3.22)$$

which is the Maxwell-Boltzmann distribution of electron energies for temperature T. Simplification of equations results when the following change of variables is performed

$$x = E_2/U_p. \quad (3.23)$$

With the additional formula for conversion of the cross section into rate of ionization

$$K(p,c) = \int_0^\infty Q(p,c) v_2 f(\epsilon_2) d\epsilon_2 \qquad (3.24)$$

where K(p,c) = rate of ionization from level p

Q(p,c) = Equation (3.18)

v_2 = velocity of incident electron

$f(\epsilon_2)d\epsilon_2$ = Equation (3.22) ,

Equations (3.18) through (3.23) result in the following equation as presented in [5] for the rate of ionization from level p:

$$K(p,c) = 5.45\ T^{-3/2} \int_1^\infty I\ e^{-xU_p/kT}\ dx \ , \qquad (3.25)$$

where
$$I = \begin{cases} (x-1)^{3/2}/(x+1)^{3/2} & x \le 2 \\ (5x-6)x^{1/2}/3(x+1)^{3/2} & x \ge 2 \end{cases}$$

T = electron temperature

U_p = ionization energy of level p

k = Boltzmann's constant .

For helium the same formula was used with the p referring to level number and using the appropriate U_p.

Collisional excitation between discrete levels is calculated in a similar manner. In this case, the cross section for excitation from level p to level q is given by

$$Q(p,q) = \int_0^\infty f(v_e)\ Q'(U_{q+1},U_q)\ dv_e \qquad (3.26)$$

where $Q'(U_{q+1},U_q) \equiv Q'(U_q) - Q'(U_{q+1})$.

The other symbols are the same as for collisional ionization. In this instance, however, the classical cross section given by (3.26) must be modified by multiplying it by q^{-3} to give a quantum related cross section as shown by McCarroll [14], since excitation between discrete levels is alien to classical mechanics.

With this modification, the use of Equations (3.19) through (3.23), and the Bohr formula for hydrogenic energy levels, Equation (1.1), Equation (3.26) becomes that given in [5] for the collisional excitation rate between levels p,q:

$$K(p,q) = \frac{10.9}{T^{3/2}} \frac{\bar{p}^2}{\bar{q}(\bar{q}^2 - \bar{p}^2)} \int_1^\infty E \exp\left\{\frac{-157890(\bar{q}^2 - \bar{p}^2)y}{\bar{p}^2\bar{q}^2 T}\right\} dy \qquad (3.27)$$

$$E = \begin{cases} \dfrac{\{2 - a + y(1 + 4a)\}(y - 1)^{1/2}(a + 1)^{1/2}}{3a^{1/2}(a + y)^{3/2}} & y \leq 1 + a \\[4mm] \dfrac{\{-3a + y(3 + 4a)\}y^{1/2}}{3(a + y)^{3/2}} & y \geq 1 + a \end{cases}$$

$$a = \bar{q}^2/(\bar{q}^2 - \bar{p}^2) .$$

where in hydrogen,

$$\begin{aligned} p &= \bar{p} \\ q &= \bar{q} \end{aligned} \quad \text{principal quantum numbers} \qquad (3.28)$$

and in the helium approximation,

p,q = level numbers

$\bar{p},\bar{q}$ = effective principal quantum numbers corresponding to p,q. (3.29)

Collisional ionization and excitation rates, Equations (3.25) and (3.27), are evaluated by the Gaussian integration method. The integrals, by change

of variable, are put in the form

$$\int_{-1}^{1} f(x)dx \quad . \tag{3.30}$$

They are approximated by the sum

$$\sum_{i=1}^{n} a_i f(x_i) \quad , \tag{3.31}$$

where the x_i's are the zeros of the Legendre polynomial of order n. The a_i's satisfy

$$a_1 + \ldots + a_n = \int_{-1}^{1} dx = 2$$

$$a_1 x_1 + \ldots + a_n x_n = \int_{-1}^{1} x dx = 0$$

$$\begin{array}{ccc} \cdot & \cdot & \cdot \\ \cdot & \cdot & \cdot \\ \cdot & \cdot & \cdot \end{array}$$

$$a_1 x_1^{n-1} + \ldots + a_n x_n^{n-1} = \int_{-1}^{1} x^{n-1} dx = \begin{cases} 0 & n \text{ even} \\ \dfrac{2}{n} & n \text{ odd} \end{cases} \quad . \tag{3.32}$$

The tabulated values of x_i and a_i for n = 16 are used in the program for calculating K(p,c) and K(p,q). This program, found in the Appendix, stores the resulting rates in COLIZ and COLEX which are punched onto cards and read into the main program.

Collisional de-excitation rates are calculated by

$$n_E(q)K(q,p) = n_E(p)K(p,q) \quad , \tag{3.33}$$

as required by detailed balancing, where $n_e(q), n_e(p)$ = Saha density of levels q and p.

The loss from level p due to photoionization is given by

$$\frac{dn(p)}{dt} = -I\sigma(p,\nu) \, n(p) \,, \tag{3.34}$$

where $n(p)$ = density of level p

I = photon flux density

$\sigma(p,\nu)$ = photoionization cross section.

The equations for I and $\sigma(p,\nu)$ are given by

$$I = P\lambda/hc \tag{3.35}$$

where P = power density of infrared

λ = wavelength of infrared radiation

h = Planck's constant

c = speed of light

and,

$$\sigma(\nu,p)_{Hydrogen} = g \frac{32\pi^2 e^6 R \lambda^3}{3^{3/2} h^3 c^3 p^5} \qquad \text{for } I_p \leq h\nu \tag{3.36}$$

$$= 0 \qquad\qquad I_p > h\nu$$

where g = gaunt factor $\simeq 1$

e = electron charge

R = Rydberg

I_p = ionization energy for level p

ν = frequency of infrared radiation ,

as given in [15] for hydrogen and hydrogen-like ions. Equations (3.35) and (3.36), for a constant power density of 1 kW/cm^2, simplify to

$$I\sigma(\lambda,p) = \frac{5.25 \times 10^{31} \times \lambda^4}{p^5} = \text{loss rate (sec}^{-1}) . \qquad (3.37)$$

The value of the lowest level photoionized is given by

$$P_{min} = \left[\frac{U\lambda}{hc}\right]^{1/2} , \qquad (3.38)$$

where U = ionization energy for hydrogen
ground state

λ = wavelength of radiation.

Equation (3.38) was solved for the particular wavelength necessary to ionize levels 4, 5, 6, . . . , 20. For example, a λ slightly smaller than 15.39 μm will ionize levels 13 and above. A wavelength slightly larger will only ionize levels 14 and above. In this way calculations were made for λ from 1.46 μm to 32.88 μm. The wavelengths and corresponding p_{min} are stored in the main program. Since p_{min} for $\lambda \geq 1.46$ μm is ≥ 4, which has approximately the same ionization energy in both hydrogen and helium, the same values are used for both.

NORMALIZATION CONSTANTS
FOR HELIUM $\Lambda(q,p)$

level number p	actual level	c_p
1	$1s^2$	46.5
2	$2s\ ^3S$	9.54
3	$2s\ ^1S$	51.9
4	$2p\ ^3P$	16.6
5	$2p\ ^1P$	44.1
6	$3s\ ^3S$	1.27
7	$3s\ ^1S$	40.2
8	$3p\ ^3P$	17.7
9	$3d\ ^3D$	9.41
10	$3d\ ^1D$	27.76
11	$3p\ ^1P$	53.5

Figure 3.

IV. ARRAYS

The array EHE(35,4) is used in the calculation of most of the atomic coefficients for helium. It contains, for 35 levels: the energy difference between the level and the ground state, ionization energies, an "effective" principal quantum number, and the degeneracy of the level. A diagram of the array is shown in Figure 4. The rows denote the level number; the correspondence between the level number and the actual level in helium is shown in Figure 5. As shown in that figure, levels one through eleven are the first eleven degenerate levels, with twelve through thirty-five grouping the degenerate levels together. Level 12, for example, contains the 4s, 4p, 4d, and 4f energy levels.

Column one of EHE contains the energy difference between the level and the apparent ground level of 198305 cm^{-1}. The first eleven levels were obtained from tabulated values [6]; the rest were calculated using the hydrogen approximation

$$EHE(p,1) = 198305 - 109678/(p - 8)^2 , \tag{4.1}$$

where p denotes level number, not quantum number.

Column two holds the energy needed to ionize from that level number and was calculated by

$$EHE(p,2) = 198305 - EHE(p,1) . \tag{4.2}$$

Column three contains an "effective" principal quantum number. This makes the calculation of some coefficients which depend on energy level easier to calculate, and is the principal quantum number that an energy level would have in a hydrogen atom

$$EHE(p,3) = [109678/EHE(p,2)]^{1/2} , \qquad (4.3)$$

$$\text{where } 109678 \text{ cm}^{-1} = \text{Ionization energy of hydrogen.}$$

Column four contains the degeneracy of the level number. For one through eleven the degeneracy is

$$EHE(p,4) = 2J_p + 1 \qquad 1 \le p \le 11 , \qquad (4.4)$$

where J is the total angular momentum quantum number for the level. Eleven and up are groups of degenerate levels, and for helium,

$$EHE(p,4) = 4(p - 8)^2 , \qquad (4.5)$$

since a level number greater than eleven corresponds to a principal quantum number eight less. Array EHE is produced in the program for calculating spontaneous transition rates and is presented in the Appendix.

Figure 6 shows the calculated energy levels for atomic hydrogen using the Bohr formula

$$E(p) = 109678/p^2 . \qquad (4.7)$$

The values of the Saha densities are stored in the array SAEQP(35,4,7). The first subscript refers to level number and the second to temperatures of 300° K, 400° K, 500° K and 1000° K. The third refers to free electron densities of 10^8, 5×10^8, 10^9, 5×10^9, 10^{10}, 5×10^{10} and 10^{11} per cubic centimeter.

The rates of collisional ionization, K(p,c), are stored in array COLIZ(30,4). This array stores the rates for the first thirty levels, and the four temperatures.

The array COLEX(30,35,4) contains the rates of collisional excitation, $K(p,q)$, where $q > p$. The first subscript refers to the lower level, the second to the upper level, and the third to the four temperatures.

GSIRL(30,2) contains the infrared loss term for the equations for a possible use of up to thirty levels. The second subscript refers to the two cases: 1 for no incident infrared in which the loss term is zero, and 2 for the case with infrared radiation. This array is calculated in the main program.

SPONA(35,35) stores the spontaneous transition rates, $A(p,q)$, between the first thirty-five levels.

The array BETA(29,4) holds the radiative recombination rates for twenty-nine levels for the four temperatures.

ELECD(7) and TEMP(4), respectively, hold the values of the seven electron densities and four temperatures.

RLAMB(17,2), in the first column, stores seventeen wavelengths of infrared radiation, and in column two, the minimum quantum level effected by the radiation. This information is used to calculate the infrared loss terms in the rate equations.

COLDEX(35,30) stores the values of collisional de-excitation rates, $K(p,q)$, where $p > q$. These values are calculated from COLEX and SAEQP by Equation (3.33).

Arrays are also used to calculate and store the coefficients of Equation (2.10). AE(30) contains $a(p) \equiv \sum_{q<p} A(p,q)$, where q is, as before, the level above which the atoms are assumed to be in Saha equilibrium.

RKAPA(30) holds $K(p) \equiv K(p,c) + \sum_{q \neq p} K(p,q)$, which is the depopulation rate for level p by collisional processes.

ASUM(30) contains $\sum_{q>s} \frac{n_E(q)}{n_E(p)} A(q,p)$, and SIGMK(30) stores $K(p,\sigma) \equiv \sum_{q>s} K(p,q)$.

These atomic parameters are then arranged to form the coefficients of the rate equations and stored in GS(29,29,2) with the last subscript denoting one set with no infrared and one with infrared. The constant terms [the right-hand side of Equation (2.10)] are stored in GSC(29,2). RHO(29,2) holds the values of ρ and QUEN(30) stores percent light quenching on each level for printout. IITER(2) and EEPS(2) store the number of iterations performed and the final value of M^K in Equation (2.15).

EHE(35,4) ARRAY

LEVEL NUMBER	1	2	3	4	ACTUAL LEVEL
1	0.0	198305.0	0.74	1.0	$1s^2$
2	159850.3	38454.69	1.69	3.0	$2s\ ^3S$
3	166271.6	32033.31	1.85	1.0	$2s\ ^1S$
35	198154.5	150.45	27	2916	27

Figure 4.

Level number	level	Level number	level
1	$1s^2$	18	10
2	$2s\ ^3S$	19	11
3	$2s\ ^1S$	20	12
4	$2p\ ^3P$	21	13
5	$2p\ ^1P$	22	14
6	$3s\ ^3S$	23	15
7	$3s\ ^1S$	24	16
8	$3p\ ^3P$	25	17
9	$3d\ ^3D$	26	18
10	$3d\ ^1D$	27	19
11	$3p\ ^1P$	28	20
12	4	29	21
13	5	30	22
14	6	31	23
15	7	32	24
16	8	33	25
17	9	34	26
		35	27

Figure 5.

ATOMIC HYDROGEN ENERGY LEVELS

LEVEL	IONIZATION ENERGY (cm^{-1})	LEVEL	IONIZATION ENERGY (cm^{-1})
1	109678	15	487
2	27419	16	428
3	12186	17	380
4	6854	18	339
5	4387	19	303
6	3046	20	274
7	2238	21	248
8	1713	22	227
9	1354	23	207
10	1097	24	190
11	906	25	175
12	762	26	162
13	649	27	150
14	559	28	139

Figure 6.

V. RESULTS AND CONCLUSIONS

Figures 7 - 10 are the tabulated results of the computer analysis for atomic hydrogen and helium. Only one case of atomic hydrogen was run: $T = 300^\circ$ K and $n(c) = 10^{10}/cm^3$. It was run primarily to demonstrate the feasibility of the method of analysis and the programs. For atomic helium, the following cases were calculated: $T = 300^\circ$ K, 500° K, 1000° K and $n(c) = 10^8/cm^3$, $10^9/cm^3$, $10^{10}/cm^3$ and $10^{11}/cm^3$. As can be seen from the resultant values of $\rho(s)$ which should asymptotically approach 1.0, the cases of $n(c) = 10^8/cm^3$ and $10^9/cm^3$ are probably less accurate than the other cases since $\rho(s)$ for these cases was approximately 0.4 and 0.8, respectively. This indicates that more levels need to be considered in the equations. In these figures, the minus designates the results for λ slightly lower than that indicated and the plus slightly higher.

The tabulated results are shown graphically in Figures 11 - 23. As seen from the graphs, the percentage light quenching increases with increasing wavelength, since the loss term due to ionization is $\sim \lambda^4$, until the photon energy decreases to a value which photoionizes one less level. At this point there is a sharp drop. This is repeated, with the average quenching increasing, until the effect of the decreasing number of levels photoionized begins to predominate over the increasing value of cross section, and the average level of quenching begins to decrease. The results obtained provide a basis for further quantitative analysis of light quenching due to photoionization of highly excited states and also for analysis of the possible role of electron heating.

The present analysis provided insight into the atomic processes occurring and also pointed out important considerations for future work. First, the solution of the simultaneous equations must be performed in double precision arithmetic due to the large number of calculations involved in the iteration process.

Second, more equations must be used for the lower electron densities so that $\rho(s)$ approaches 1.0 more closely. This insures that the upper levels are very nearly in Saha equilibrium with the free electrons, one of the basic assumptions of the method.

Third, care must be taken when manipulating the equations to be solved. Operations which are permitted when solving equations exactly such as multiplying each term in an equation by a constant greatly influence the accuracy of the results and the efficiency of the program when solving the equations by an iterative method. This becomes increasingly important as the number of equations increases.

Finally, more cases of electron density, temperature and wavelength must be analyzed along with different values of infrared power density to obtain a more complete understanding of possible trends in the results.

HYDROGEN PERCENT QUENCHING

λ μm	$n(c) = 10^{10}$ −	+
1.46	1.00	.81
2.28	4.61	3.56
3.28	13.80	11.85
4.46	31.63	23.21
5.82	47.19	31.48
7.38	55.21	35.39
9.11	57.06	36.19
10.6	51.76	51.76
11.0	55.70	35.29
13.11	53.34	34.03
15.39	50.32	32.40
17,85	47.15	30.68
20.49	44.05	29.00
23.32	41.16	27.41
26.32	38.40	25.81
29.51	35.81	24.25
32.88	33.30	22.63

ρ(s) = .99

Figure 7.

HELIUM PERCENT QUENCHING
300° K

λ μm	ρ(s) = 0.35 $n(c) = 10^8$ –	+	ρ(s) = 0.74 10^9 –	+	ρ(s) = 0.92 10^{10} –	+	ρ(s) = 0.97 10^{11} –	+
1.46	.04	.02	.04	.02	.04	.02	.04	.03
2.28	.12	.05	.13	.06	.14	.07	.16	.09
3.28	.22	.02	.26	.05	.31	.10	.39	.18
4.46	.06	.05	.18	.17	.35	.34	.63	.60
5.82	.16	.15	.50	.49	.99	.97	1.71	1.58
7.38	.39	.38	1.25	1.24	2.45	2.40	3.94	3.32
9.11	.84	.83	2.74	2.71	5.28	5.15	7.29	5.42
10.6	1.44	1.44	4.66	4.66	8.79	8.79	9.41	9.41
11.0	1.64	1.62	5.29	5.24	9.95	9.46	10.72	6.96
13.11	2.87	2.85	9.16	9.07	16.46	15.08	12.99	7.77
15.39	4.49	4.44	14.03	13.74	23.56	19.68	13.70	7.55
17.85	6.27	6.19	19.15	18.54	28.78	22.41	12.82	6.78
20.49	7.95	7.82	23.82	22.65	31.53	22.94	11.17	5.70
23.32	9.34	9.13	27.48	25.42	31.70	21.37	9.19	4.49
26.32	10.30	9.92	29.73	26.19	29.33	17.80	7.06	3.20
29.51	10.79	10.01	30.14	23.99	24.56	12.48	4.95	1.94
32.88	10.64	8.58	27.71	16.56	17.45	5.97	2.95	.81

Figure 8.

HELIUM PERCENT QUENCHING
500° K

λ μm	$\rho(s) = 0.38$ 10^8		$\rho(s) = 0.77$ 10^9		$\rho(s) = 0.94$ 10^{10}		$\rho(s) = 0.98$ 10^{11}	
	−	+	−	+	−	+	−	+
1.46	.04	.02	.04	.02	.04	.02	.04	.02
2.28	.12	.05	.12	.06	.13	.07	.15	.08
3.28	.22	.02	.25	.04	.28	.08	.35	.14
4.46	.05	.04	.14	.13	.27	.26	.49	.46
5.82	.13	.12	.38	.37	.74	.73	1.32	1.19
7.38	.30	.29	.95	.93	1.83	1.78	2.97	2.41
9.11	.65	.64	2.07	2.05	3.94	3.80	5.32	3.77
10.6	1.11	1.11	3.52	3.52	6.53	6.53	6.62	6.62
11.0	1.26	1.24	3.99	3.95	7.40	6.94	7.56	4.72
13.11	2.21	2.18	6.93	6.85	12.23	10.98	8.95	5.22
15.39	3.44	3.39	10.64	10.36	17.50	14.28	9.34	5.10
17.85	4.79	4.71	14.54	13.98	21.36	16.24	8.78	4.64
20.49	6.06	5.94	18.11	17.07	23.39	16.66	7.73	3.98
23.32	7.11	6.92	20.90	19.12	23.52	15.57	6.46	3.20
26.32	7.83	7.51	22.57	19.62	21.76	13.00	5.06	2.33
29.51	8.18	7.55	22.79	17.84	18.21	9.15	3.62	1.44
32.88	8.04	6.43	20.81	12.15	12.92	4.39	2.20	.61

Figure 9.

HELIUM PERCENT QUENCHING

1000° K

λ µm	ρ(s) = 0.39 10^8		ρ(s) = 0.78 10^9		ρ(s) = 0.95 10^{10}		ρ(s) = 0.99 10^{11}	
	−	+	−	+	−	+	−	+
1.46	.04	.02	.04	.02	.04	.02	.04	.02
2.28	.12	.05	.12	.06	.13	.06	.14	.07
3.28	.22	.01	.24	.03	.26	.05	.31	.10
4.46	.04	.03	.10	.09	.18	.17	.35	.31
5.82	.10	.09	.27	.26	.50	.49	.90	.77
7.38	.22	.21	.65	.64	1.23	1.18	1.94	1.49
9.11	.47	.45	1.41	1.39	2.62	2.49	3.32	2.25
10.6	.78	.78	2.39	2.39	4.30	4.30	3.97	3.97
11.0	.89	.87	2.72	2.68	4.89	4.50	4.55	2.78
13.11	1.55	1.52	4.71	4.63	8.03	7.06	5.33	3.08
15.39	2.40	2.34	7.23	6.99	11.45	9.17	5.59	3.07
17.85	3.31	3.24	9.87	9.41	13.99	10.48	5.35	2.88
20.49	4.17	4.06	12.28	11.47	15.38	10.84	4.83	2.54
23.32	4.86	4.71	14.15	12.83	15.55	10.23	4.14	2.10
26.32	5.33	5.08	15.25	13.13	14.47	8.64	3.33	1.57
29.51	5.55	5.08	15.36	11.91	12.19	6.14	2.44	1.00
32.88	5.42	4.30	13.96	8.08	8.72	2.99	1.52	.43

Figure 10.

PERCENT QUENCHING VS WAVELENGTH IN HYDROGEN

TEMP=300 °K ELECTRON DENSITY=10^{10}/CM^3 INFRARED INTENSITY=1KW/CM^2

PERCENT QUENCHING

WAVELENGTH — 10^{-6} METERS
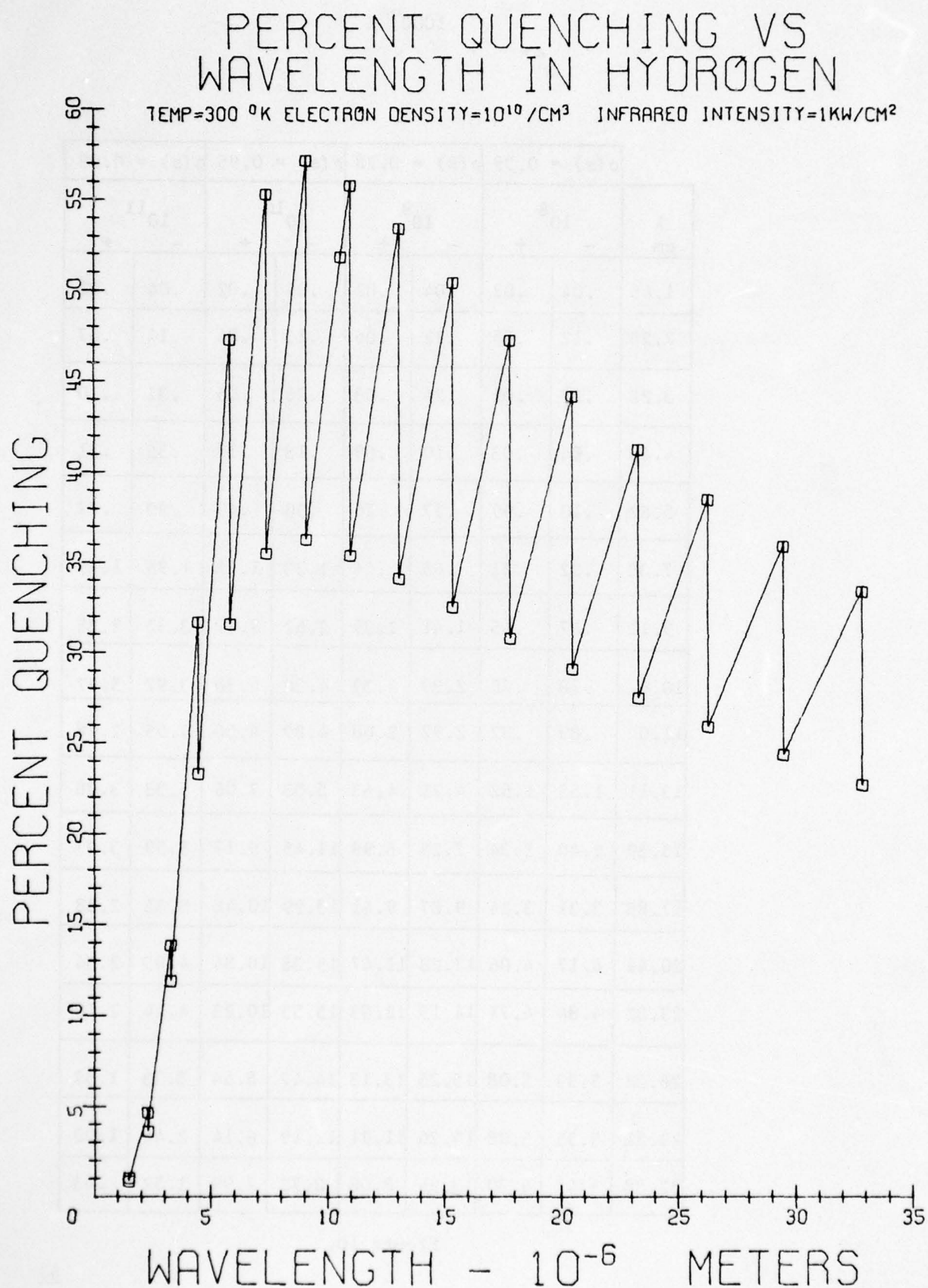
Figure 11.

PERCENT QUENCHING VS WAVELENGTH IN HELIUM

TEMP=300 °K ELECTRON DENSITY=10^8 /CM³ INFRARED INTENSITY=1KW/CM²

WAVELENGTH – 10^{-6} METERS
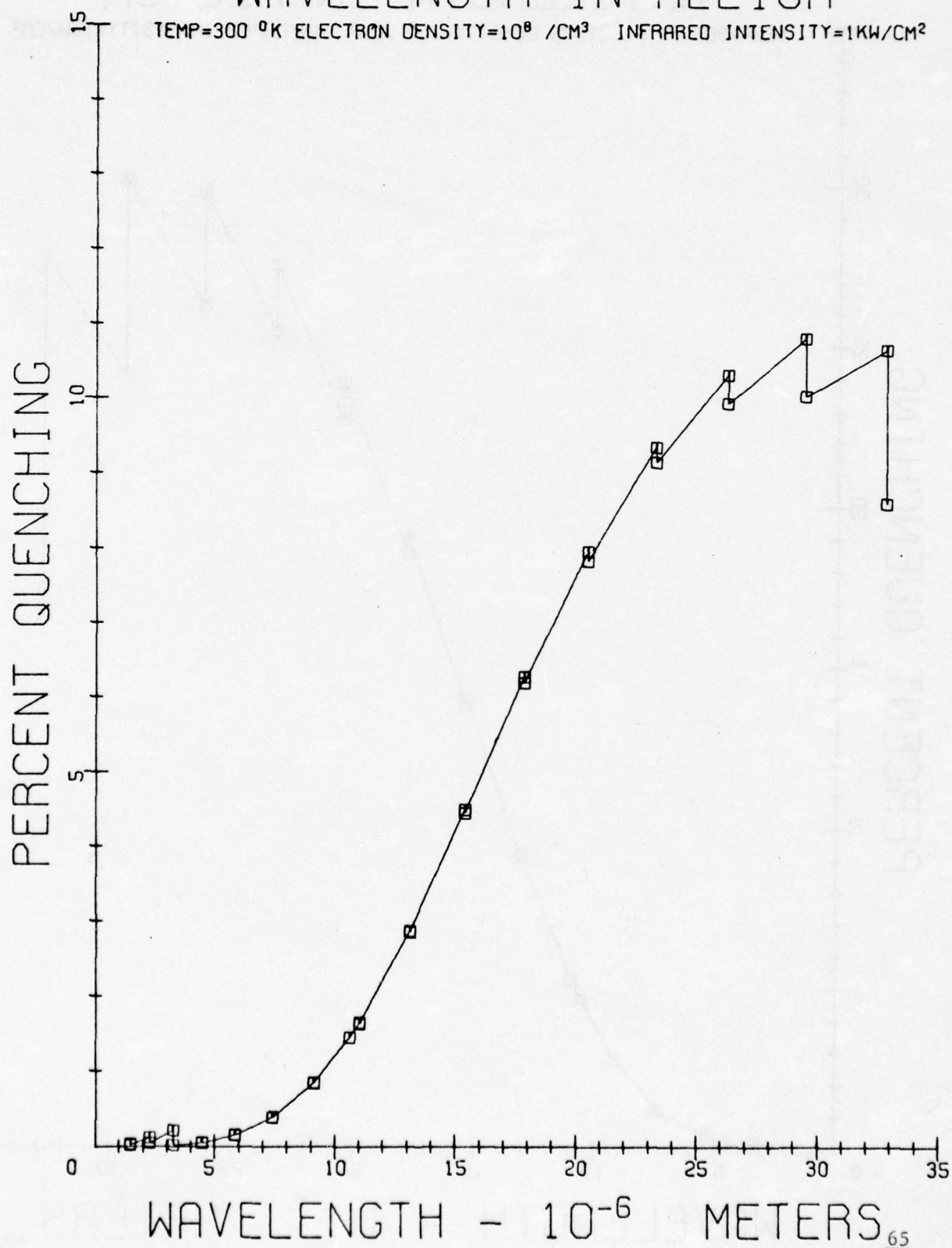
Figure 12.

PERCENT QUENCHING VS WAVELENGTH IN HELIUM

TEMP=300 ^{0}K ELECTRON DENSITY=10^9 /CM^3 INFRARED INTENSITY=1KW/CM^2
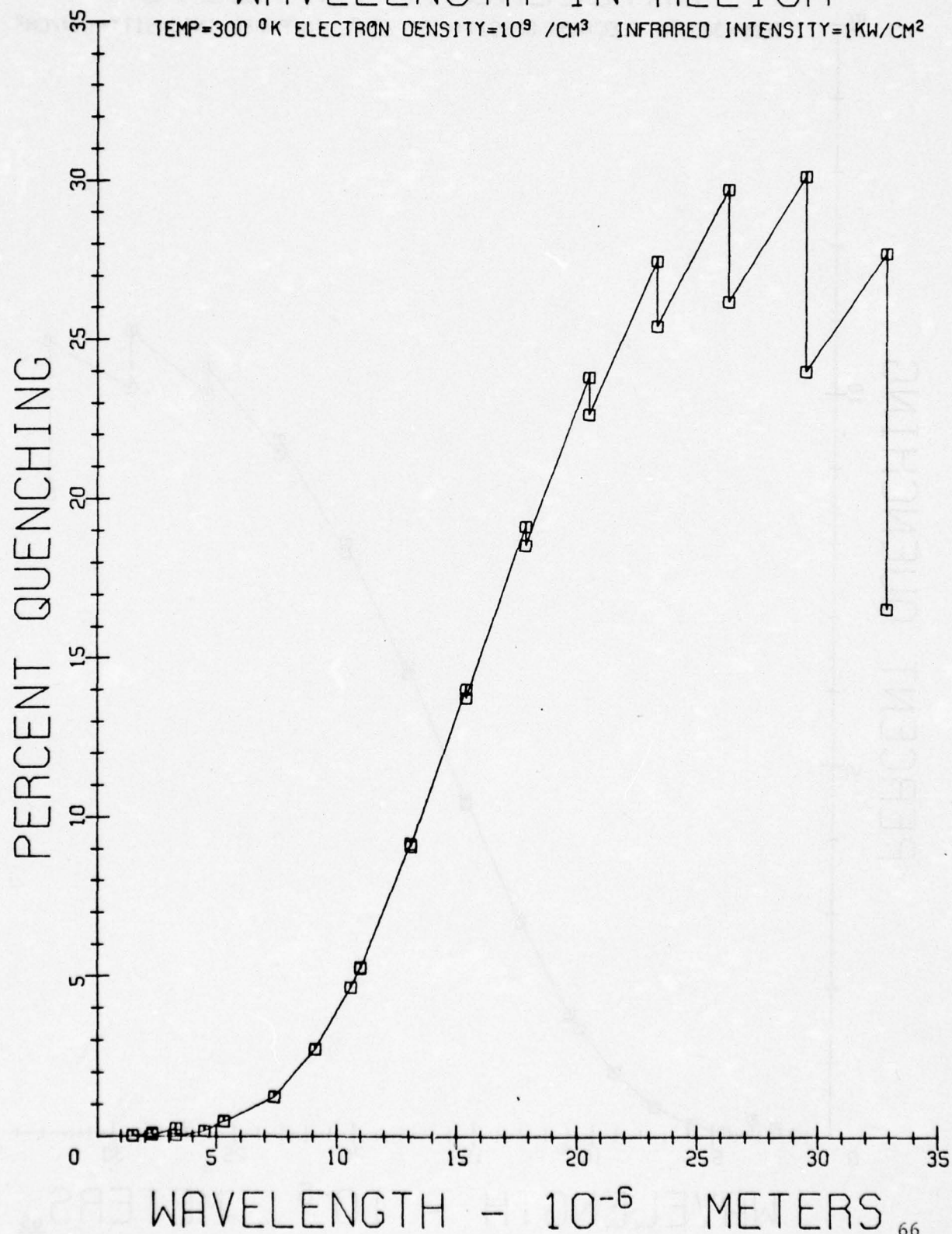
Figure 13.

PERCENT QUENCHING VS
WAVELENGTH IN HELIUM

TEMP=300 ^{0}K ELECTRON DENSITY=10^{10}/CM^3 INFRARED INTENSITY=1KW/CM^2

WAVELENGTH $-$ 10^{-6} METERS

Figure 14.

PERCENT QUENCHING VS WAVELENGTH IN HELIUM

TEMP=300 °K ELECTRON DENSITY=10^{11}/CM³   INFRARED INTENSITY=1KW/CM²

Figure 15.

PERCENT QUENCHING VS
WAVELENGTH IN HELIUM

TEMP=500 ^{0}K ELECTRON DENSITY=10^8 /CM^3 INFRARED INTENSITY=1KW/CM^2

WAVELENGTH — 10^{-6} METERS
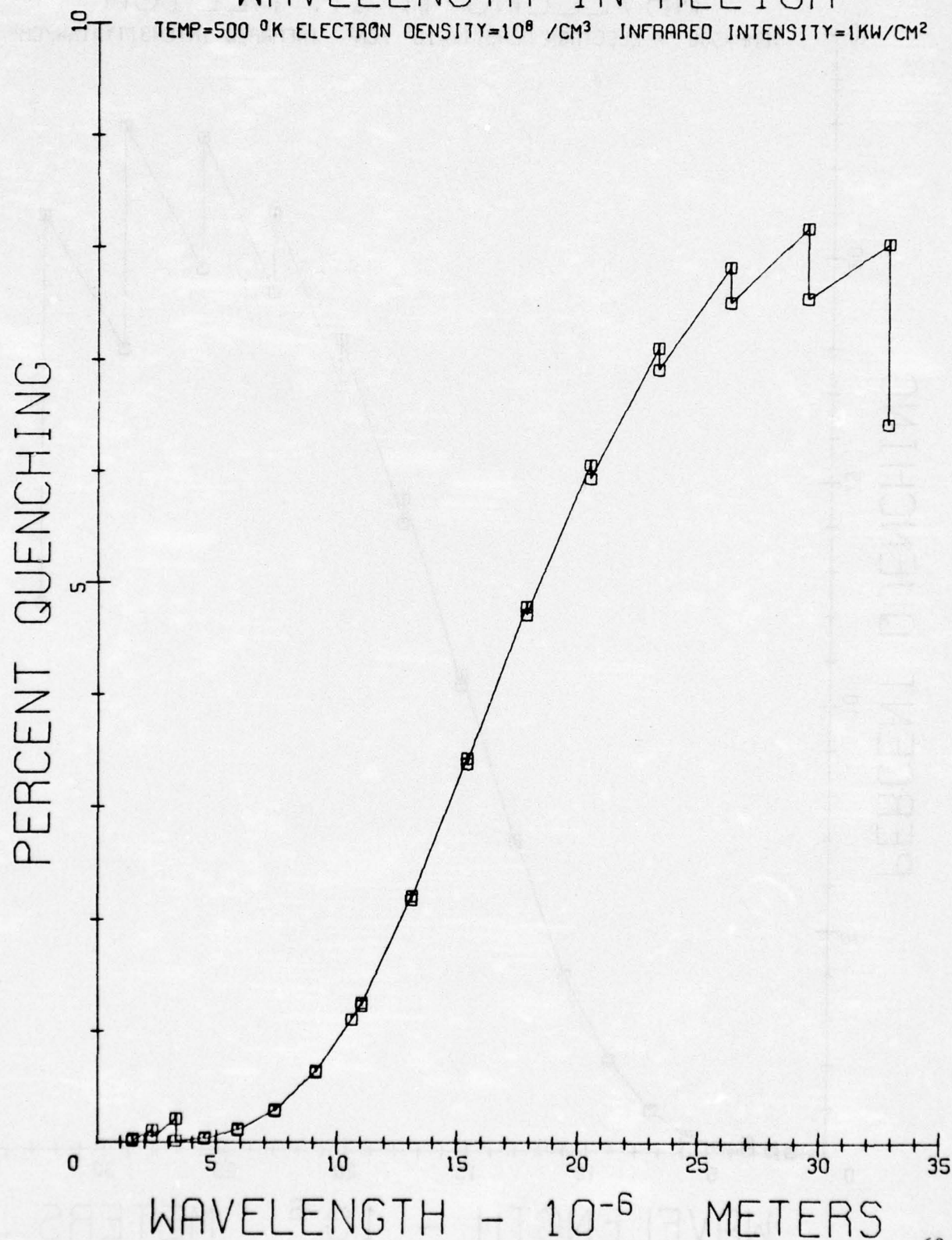
Figure 16.

PERCENT QUENCHING VS
WAVELENGTH IN HELIUM

TEMP=500 ^{0}K ELECTRON DENSITY=10^9 /CM^3 INFRARED INTENSITY=1KW/CM^2

PERCENT QUENCHING

WAVELENGTH $-$ 10^{-6} METERS

70

Figure 17.

PERCENT QUENCHING VS
WAVELENGTH IN HELIUM

TEMP=500 °K ELECTRON DENSITY=10¹⁰/CM³   INFRARED INTENSITY=1KW/CM²

WAVELENGTH – 10⁻⁶ METERS
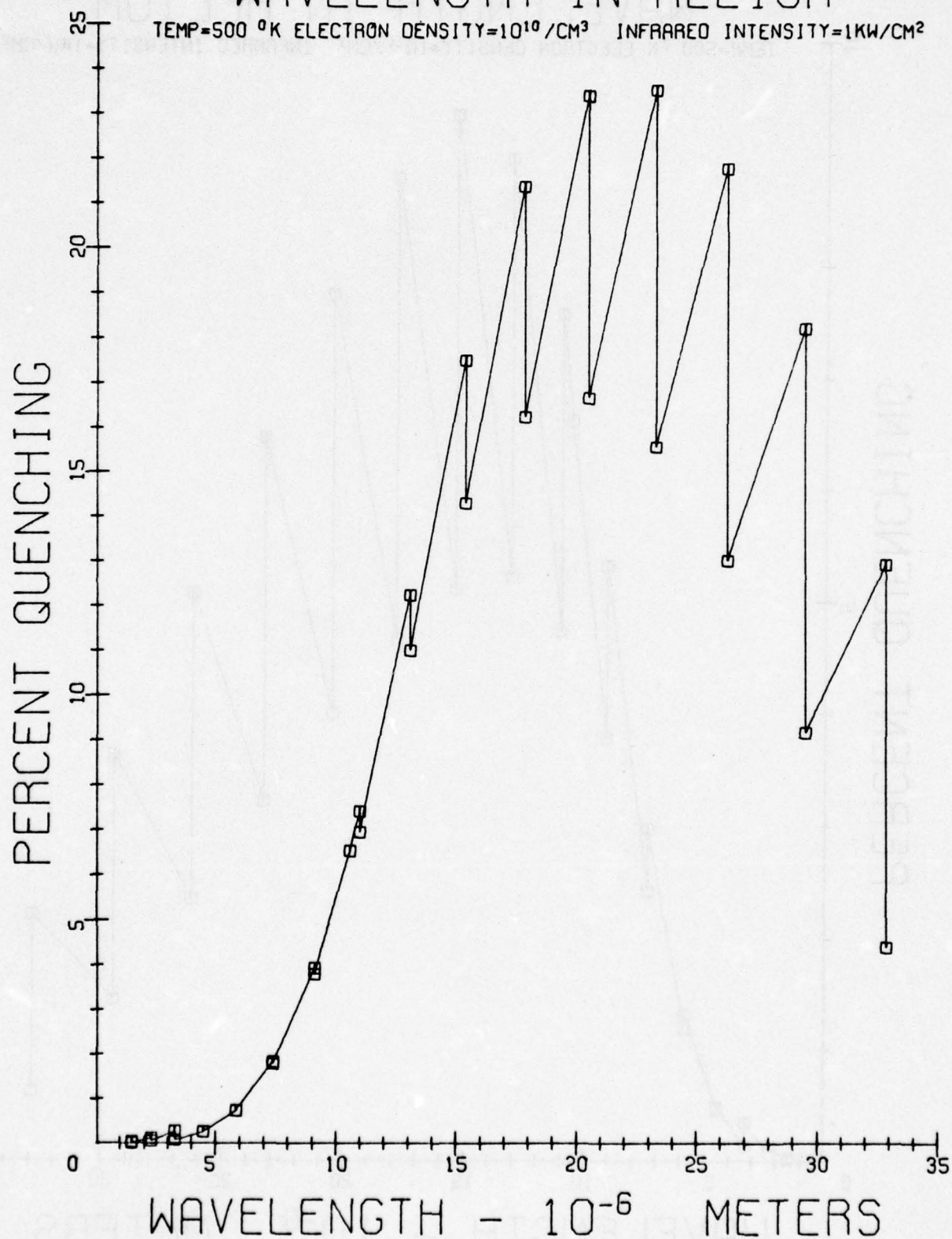
Figure 18.

PERCENT QUENCHING VS
WAVELENGTH IN HELIUM

TEMP=500 ^{0}K ELECTRON DENSITY=10^{11}/CM^3 INFRARED INTENSITY=1KW/CM^2

WAVELENGTH — 10^{-6} METERS   72
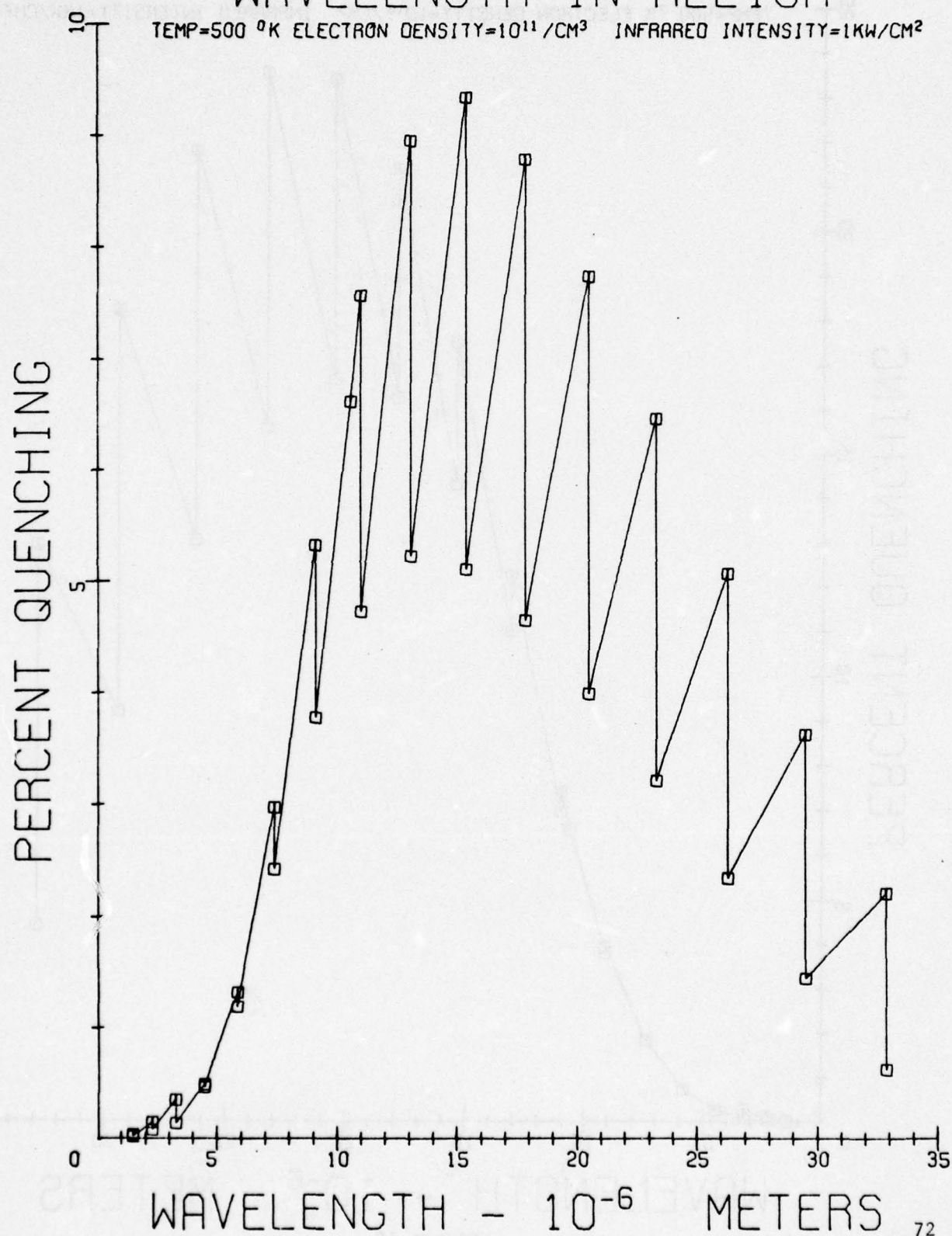
Figure 19.

PERCENT QUENCHING VS WAVELENGTH IN HELIUM

TEMP=1000°K ELECTRON DENSITY=10^8 /CM³   INFRARED INTENSITY=1KW/CM²

WAVELENGTH — 10^{-6} METERS
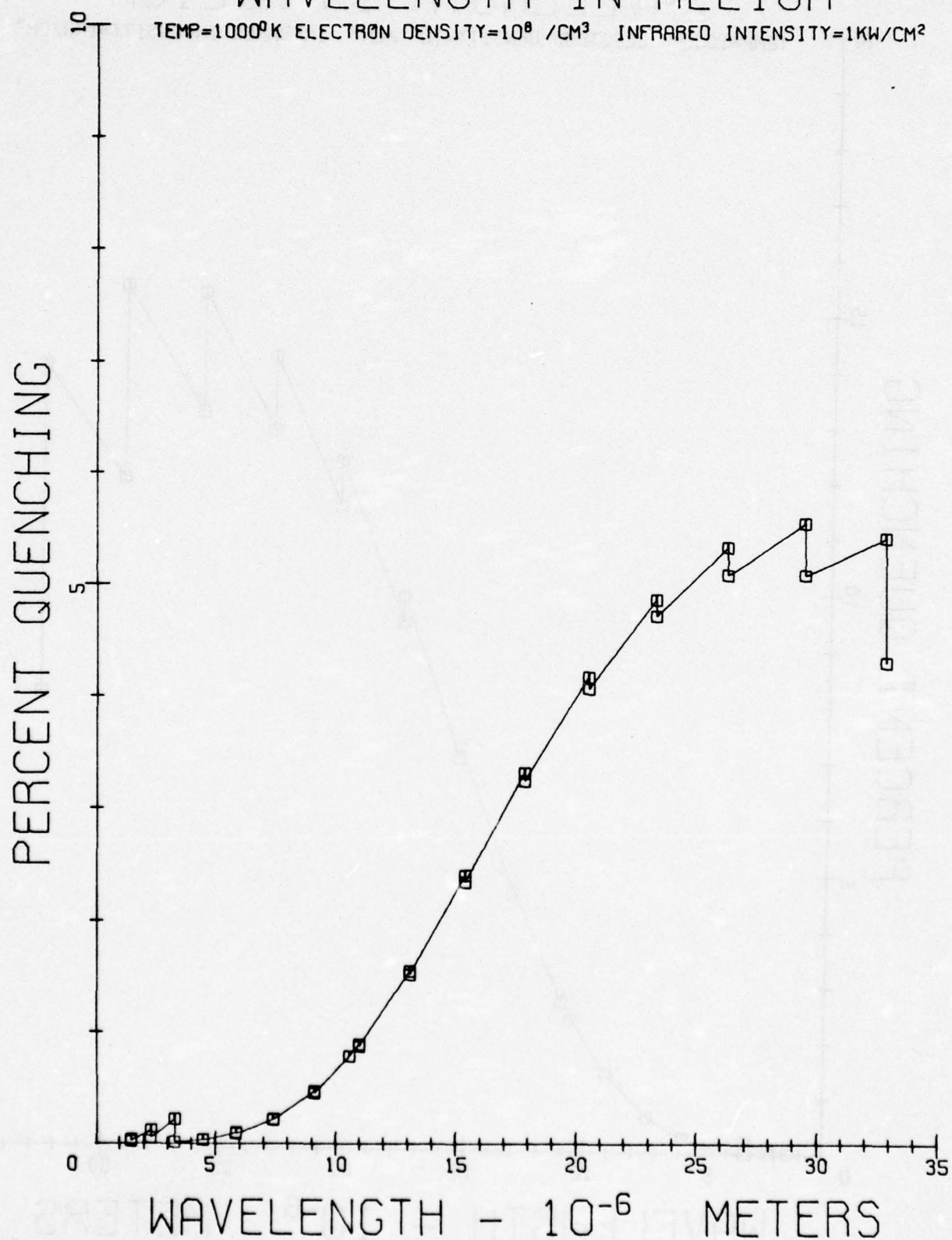
Figure 20.

PERCENT QUENCHING VS WAVELENGTH IN HELIUM

TEMP=1000°K ELECTRON DENSITY=10⁹ /CM³ INFRARED INTENSITY=1KW/CM²
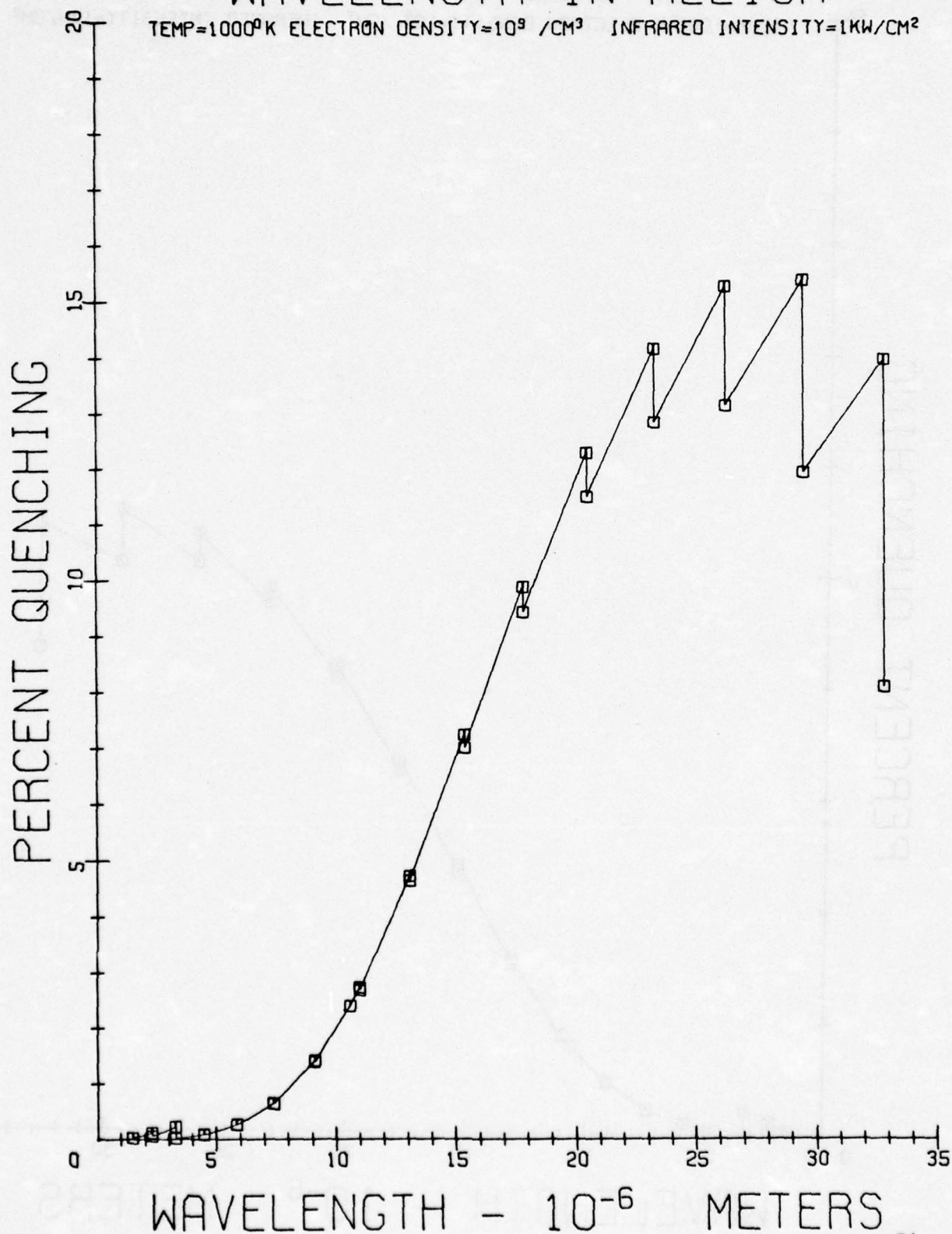
Figure 21.

PERCENT QUENCHING VS WAVELENGTH IN HELIUM

TEMP=1000°K ELECTRON DENSITY=10¹⁰/CM³   INFRARED INTENSITY=1KW/CM²
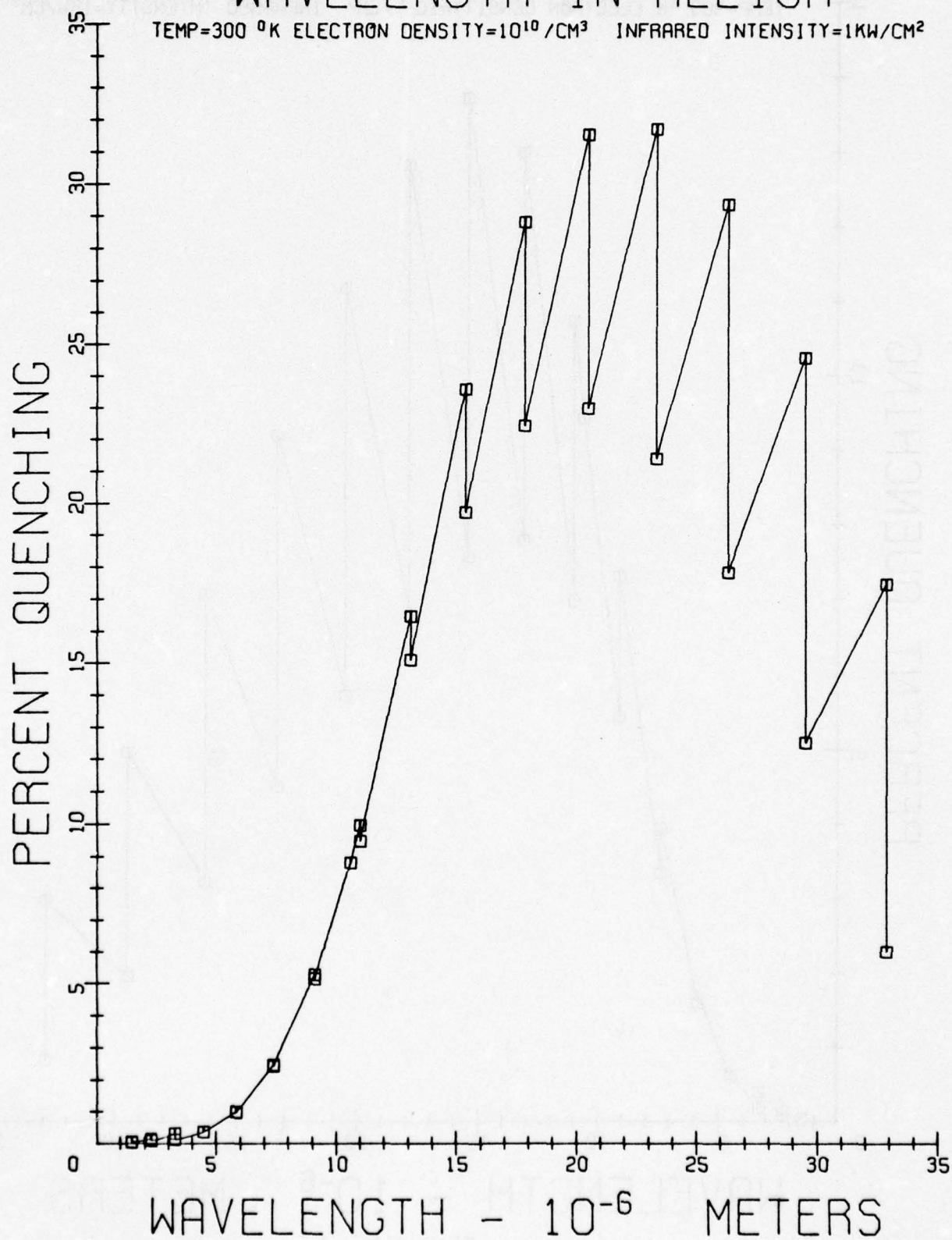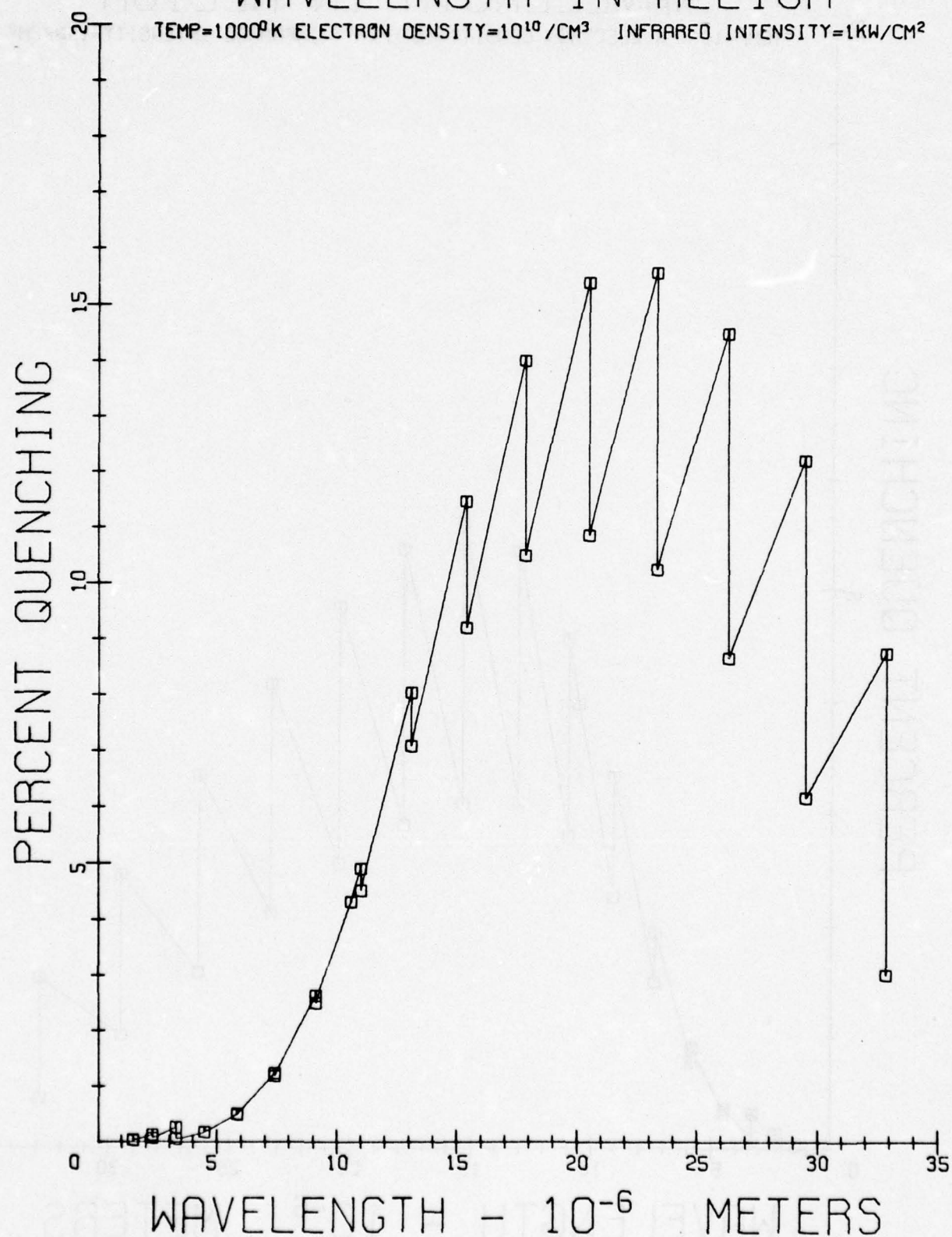

Figure 22.

PERCENT QUENCHING VS
WAVELENGTH IN HELIUM

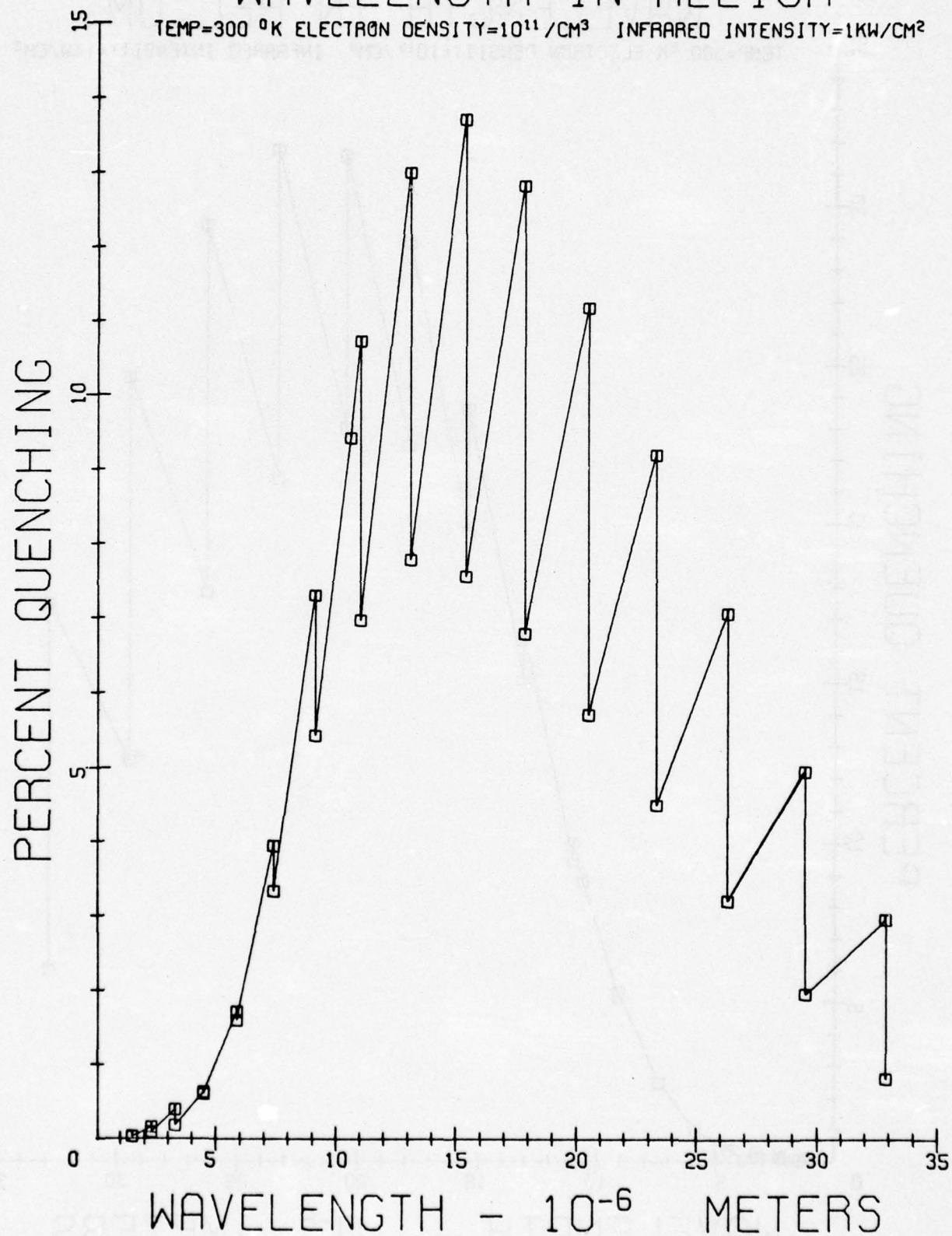TEMP=1000°K ELECTRON DENSITY=10^11/CM^3   INFRARED INTENSITY=1KW/CM^2

Figure 23.

APPENDIX
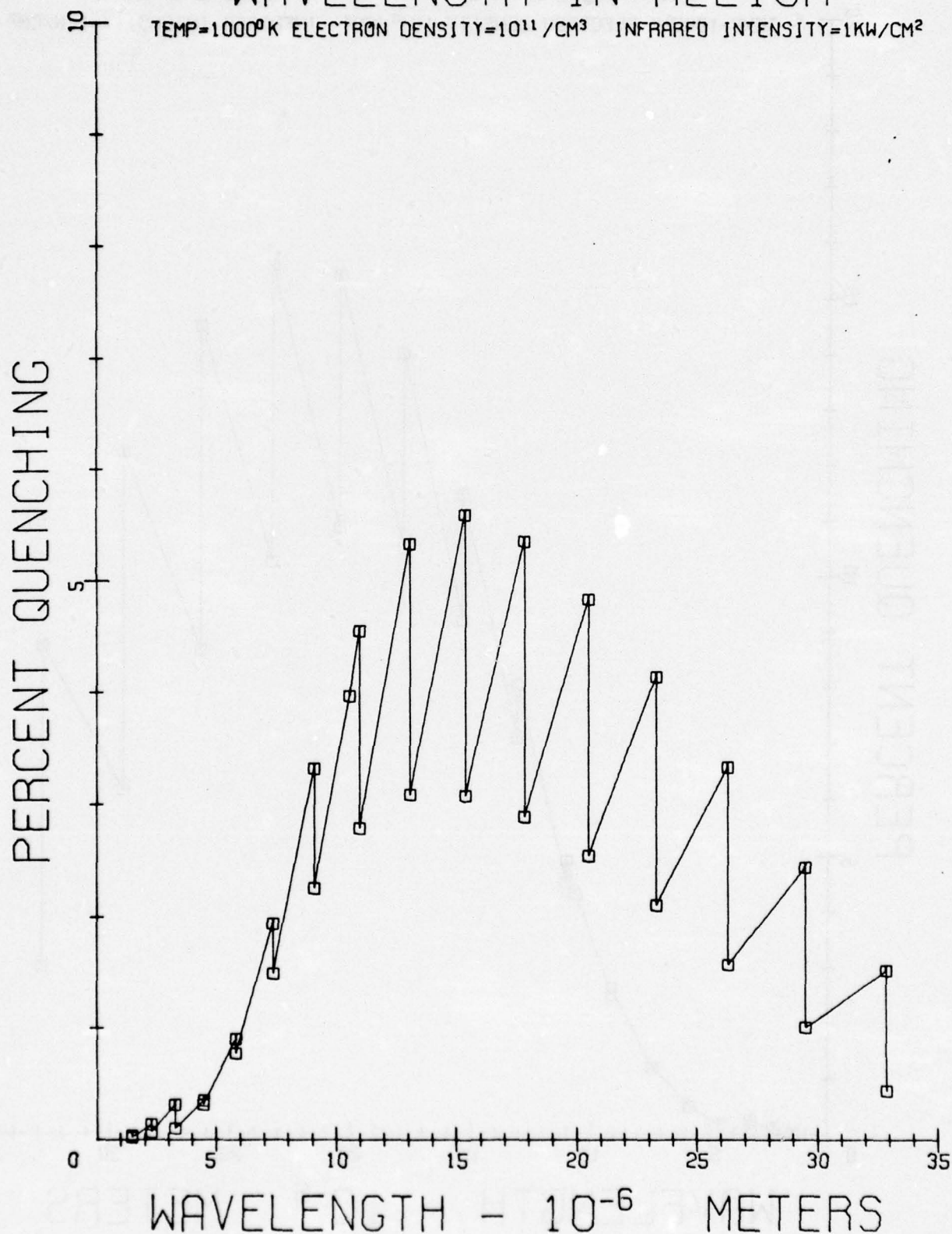
The following programs are those used in calculating the rate coefficients and percent quenching in hydrogen and helium.

The first two programs are the main programs for calculating densities and quenchings for hydrogen and helium. The third calculates the radiative recombination rates for hydrogen and the fourth takes these hydrogen results and converts them to helium rates. The fifth program calculates collisional excitation and ionization rates for helium. The sixth program calculates the Saha densities for helium, and the seventh program calculates the spontaneous transition rates.

```
C     CALCULATION OF EXCITED STATE POPULATIONS AND PERCENT QUENCHING
C               FOR HYDROGEN
C  CONSTANT INTENSITY 1 KW / CM**2
C                    VARIABLE NUMBER OF LEVELS
C NOLEV IS THE NUMBER OF LEVELS USED            MAXIMUM LEVEL=29
C
C
      DIMENSION SAEQP(60),COLIZ(30),COLEX(30,40),GSIRL(30,2),AE(30),
     1SPONA(35,35),BETA(2,30),RKAPA(30),SIGMK(30),ASUM(30),GS(29,29,2),
     1GSC(29,2),RHO(29,2),QUEN(30),IITER(2),EEPS(2),ELECD(4),TEMP(2),
     1RLAMB(16,2),COLDEX(40,30),E(35)
      DOUBLE PRECISION T,P,SUM,B,R,E1,E2,F1,F2,C(16),X(16),DSQRT,DEXP
C
      DATA SAEQP,COLIZ,COLEX,COLDEX,GSIRL,AE,SPONA,BETA,RKAPA,SIGMK,ASUM
     4,GS,GSC,RHO,QUEN,EEPS/ 5785*0.0/,IITER/ 2*0/,EPS/1.0E-6/,MAX/350/,
     5ELECD/5.0E8,1.0E9,5.0E9,1.0E10/,TEMP/300.0,400.0/,
     6(RLAMB(I,1),I=1,16)/1.46E-6,2.28E-6,3.28E-6,4.46E-6,5.82E-6,
     77.38E-6,9.11E-6, 11.E-6, 13.11E-6,15.39E-6,17.85E-6, 20.49E-6,
     823.32E-6, 26.32E-6,29.51E-6,32.88E-6/,(RLAMB(I,2),I=1,16)/4.,5.,
     96.,7.,8.,9.,10.,11.,12.,13.,14.,15.,16.,17.,18.,19./
C
C     IT=1=300      2=400
C     ID=1=5.E8     2=1.E9     3=5.E9     4=1.E10
C     IL=1=1.06     2=3.39     3=5.0      4=10.6      5=28.0
C     READ IN TEMP,DEN,LAMBDA DESIRED
      READ,IT,ID,IL
```

```
      ID=4
      IT=1
      READ,E
C
C
C     READ IN VALUES OF BETA(2,25)
C
      READ,(BETA(1,I),I=2,19)
      READ,(BETA(2,I),I=2,19)
      READ,(BETA(1,I),I=20,25)
      READ,(BETA(1,I),I=26,30)
C READ IN VALUES OF SPONA(20,20)
      DO 1 I=1,19
      II=I+1
    1 READ,(SPONA(J,I),J=II,20)
C CALCULATE HIGH VALUES OF SPONNA
      DO 501 J=21,35
      JJ=J-1
      DO 501 K=1,JJ
  501 SPONA(J,K)=(K**3)*J*((E(J)-E(K))**2)/(((J**2)-(K**2))**3)
C
C
      C(1)=.027152459411175400
      C(2)=.062253523938648D0
      C(3)=.095158511682493D0
      C(4)=.124628971255534D0
      C(5)=.149595988816577D0
      C(6)=.169156519395003D0
      C(7)=.182603415044924D0
      C(8)=.189450610455059D0
      C(9)=.189450610455069D0
      C(10)=.182603415044924D0
      C(11)=.169156519395003D0
      C(12)=.149595988816577D0
      C(13)=.124628971255534D0
      C(14)=.095158511682493D0
      C(15)=.062253523938648D0
      C(16)=.027152459411754D0
      X(1)=-.989400093499165D0
      X(2)=-.944575023073233D0
      X(3)=-.865631202387832D0
      X(4)=-.755404408355003D0
      X(5)=-.617876244402644D0
      X(6)=-.458016777657227D0
      X(7)=-.281603550779259D0
      X(8)=-.095012509837637D0
      X(9)=.095012509837637D0
      X(10)=.281603550779259D0
      X(11)=.458016777657227D0
      X(12)=.617876244402644D0
      X(13)=.755404408355003D0
      X(14)=.865631202387832D0
      X(15)=.944575023073233D0
      X(16)=.989400093499165D0
C
C
C     CALCULATION OF SAHA EQUILBRIUM
      DO 2 K=2,60
    2 SAEQP(K)=4.2E-16 *(ELECD(ID)**2)*(K**2)*(EXP(157890./((K**2)*
     1TEMP(IT))))/(TEMP(IT)**1.5)
C
```

```
C
C          CALCULATION OF K(P,C)
           T=TEMP(IT)
           DO 4 J=1,30
           P=J
           SUM=0.0
           DO 3 K=1,16
           B=C(K)
           R=X(K)
           E1=1.0D50*DEXP(-78945.D0*(P+3.D0)/(P**2.D0*T))
           E2=1.0D50*DEXP(-631560.0D0/(P**2*T*(1.0D0-R)))
           F1=2.0*1.4142D0*DSQRT(((R+1.D0)/(R+5.D0))**3.D0)/3.D0
           F2=16.D0*(7.D0+3.D0*R)/(3.D0*(1.D0-R)**2*DSQRT((5.D0-R)**3))
         3 SUM=SUM+B*(F1*E1+F2*E2)
           FINAL=5.45D0*SUM/(DSQRT(T**3)*1.0D50)
         4 COLIZ(J)=FINAL
C
C
C          CALCULATE K(P,Q)
           DO 5 J=1,30
           P=J
           JS=J+1
           DO 5 K=JS,40
           SUM=0.0
           A=(K**2)/(K**2-P**2)
           DO 6 L=1,16
           B=C(L)
           R=X(L)
           E1=DEXP(-78945.0D0*(R+1.0)/(P**2*T)-157890.0D0/(P**2*A*T))*1.0D30
           E2=DEXP(-315780.0D0*(1.0+A)/(P**2*A*T*(1.0-R)))*1.0D30
           F1=(4.0*A**2+7.0*A+5.0+4.0*A**2*R+A*R)*DSQRT((R+1.0)*(A+1.0))*A/
          4(6.0*DSQRT((3.0*A+2.0+A*R)**3))
           F2=(8.*A**2+11.*A+6.+3.*A*R)*DSQRT((2.D0*(1.D0+A))**3.D0)
          1/(3.D0*DSQRT((3.D0*A+2.D0-A*R)**3.D0)*(1.-R)**2)
         6 SUM=SUM+B*(F1*E1+F2*E2)
           FINAL=10.9D0*P**2*A*SUM/(DSQRT(T**3)*K**3)*1.0D-30
         5 COLEX(J,K)=FINAL
C
C
C          CALCULATE K(Q,P)
           DO 8 J=1,39
           K=41-J
           DO 7 L=1,30
           IF(L.GE.K)GO TO 8
         7 COLDEX(K,L)=SAEQP(L)*COLEX(L,K)/SAEQP(K)
         8 CONTINUE
C
C
C          CALCULATE A(P)
           DO 12 I=2,30
           II=I-1
           DSUM=0.0
           DO 11 J=1,II
        11 DSUM=DSUM+SPONA(I,J)
        12 AE(I)=DSUM
C
C
C          CALCULATE K(P)
           DO 13 I=1,30
        13 RKAPA(I)=COLIZ(I)
           DO 14 J=1,28
```

```
      DSUM=0.0
      JJ=J+1
      DO 15 K=JJ,29
   15 DSUM=DSUM+COLEX(J,K)
   14 RKAPA(J)=RKAPA(J)+DSUM
      DO 16 J=2,30
      DSUM=0.0
      JJ=J-1
      DO 17 K=1,JJ
   17 DSUM=DSUM+COLDEX(J,K)
   16 RKAPA(J)=RKAPA(J)+DSUM
C
C
      NOLEV=28
      NO1=NOLEV+1
      NO2=NOLEV-1
      NO3=NOLEV-2
      IF(NOLEV.LT.30)GO TO 801
      PRINT802
      STOP
  802 FORMAT('1',35X,'LEVELS EXCEED 29')
  801 NO1=NOLEV+1
C     CALCULATE K(P,SIGMA)
      DO 18 J=1,NOLEV
      DSUM=0.0
      DO 19 K=NO1,29
   19 DSUM=DSUM+COLEX(J,K)
   18 SIGMK(J)    =DSUM
C     CALCULATE ASUM
      DO 20 I=2,28
      DSUM=0.0
      DO 502 J=NO1,29
  502 DSUM=DSUM+(SAEQP(J)*SPONA(J,I)/SAEQP(I))
   20 ASUM(I)=DSUM
C
C
C     CALCULATE GSC
      DO 24 I=1,NO2
      N1=I+1
   24 GSC(I,1)   =ELECD(ID)*(SIGMK(N1)+COLIZ(N1))+((ELECD(ID)**2)*
     1BETA(IT,N1)/SAEQP(N1))+ASUM(N1)
      DO 27 I=1,NO2
   27 GSC(I,2)   =GSC(I,1)
C
C
C     CALCULATE IR LOSS TERM
      DO 1315 KMN=1,2
      DO 416 IL=1,16
      DO 10 I=1,30
      GSIRL(I,2)=0.0
   10 GSIPL(I,1)=0.0
      W=RLAMB(IL,1)
      IPM=RLAMB(IL,2)
      DO 9 J=IPM,30
    9 GSIRL(J,2)  =(5.252E31)*(W**4)/(J**5)
C
C
C     CALCULATE GS COEFFICIENTS
  709 DO 21 L=1,NO2
      N1=L+1
      K=ID
```

```
      GS(L,L,2)        =ELECD(K)*RKAPA(N1)      +AE(N1)+GSIRL(N1,2)
   21 GS(L,L,1)        =ELECD(K)*RKAPA(N1)      +AE(N1)
      DO 22 L=1,NO3
      N1=L+1
      DO 22 M=N1,NO2
      N2=M+1
      GS(M,L,1)        =-ELECD(K)*COLDEX(N2,N1)
   22 GS(M,L,2)        =-ELECD(K)*COLDEX(N2,N1)
      DO 23 L=1,NO3
      N1=L+1
      DO 23 M=N1,NO2
      N2=M+1
      DO 23 I=1,2
   23 GS(L,M,I)=-(ELECD(ID)*COLEX(N1,N2))-(SAEQP(N2)*SPONA(N2,N1)
     1/SAEQP(N1))
C       GAUSS SIEDEL METHOD TO SOLVE EQNS.
      DO 25 I=1,2
      ITER=1
   99 BIG=0.0
      DO 100 L=1,NO2
  102 DSUM=0.0
      IF(L.EQ.1) GO TO 105
      LAST=L-1
      DO 106 M=1,LAST
  106 DSUM=DSUM+GS(L,M,I)*RHO(M,I)
      IF(L.EQ.NO2)GO TO 103
  105 INITL=L+1
      DO 107 N=INITL,NO2
  107 DSUM=DSUM+GS(L,N,I) *RHO(N,I)
  103 TTEMP=( GSC(L,I)-DSUM)/GS(L,L,I)
      IF(ABS(TTEMP-RHO(L,I)).GT.BIG)BIG=ABS(TTEMP-RHO(L,I))
  100 RHO(L,I)=TTEMP
      EEPS(I)=BIG
      IITER(I)=ITER
      IF(BIG.LT.EPS)GO TO 25
  110 IF(ITER.GE.MAX)GO TO 25
      ITER=ITER+1
      GO TO 99
   25 CONTINUE
C
C
C     CALCULATE PERCENT QUENCHING
      DO 26 L=1,NO2
      LL=L+1
   26 QUEN(LL)=(RHO(L,1)-RHO(L,2))/RHO(L,1)*100.
      PRINT409,NOLEV
  409 FORMAT('1',55X,'RESULTS',10X,I2,2X,'LEVELS')
      PRINT410,TEMP(IT),ELECD(ID),RLAMB(IL,1)
  410 FORMAT('-','TEMPERATURE=',F7.0,25X,'ELECTRON DENSITY=',E12.1,25X,
     1'WAVELENGTH OF IR=',E10.3)
      PRINT411,IITER(1),IITER(2)
  411 FORMAT('-','ITERATIONS NO IR=',I3,60X,'ITERATIONS 1 KW IP=',I3)
      PRINT412,EEPS(1),EEPS(2)
  412 FORMAT(' ','EPSILON NO IR',E10.2,56X,'EPSILON-IR',E10.2)
      PRINT511
  511 FORMAT('-')
      DO 601 I=1,NO2
      II=I+1
      A1=SAEQP(II)*RHO(I,1)
      A2=SAEQP(II)*RHO(I,2)
  601 PRINT602,II,A1,II,A2
```

```
  602 FORMAT(' ','DENSITY (',I2,')= ',E16.7,40X,'IR DENSITY (',
     1I2,')= ',E16.7)
      DO 413 I=2,NOLEV
      II=I-1
  413 PRINT414,I,RHO(II,1),I,RHO(II,2)
  414 FORMAT(' ','RHO(',I2,')= ',E16.7,50X,'RHO IR (',I2,')= ',E16.7)
      PRINT418
  418 FORMAT('1')
      PRINT415
  415 FORMAT('-',50X,'PERCENT QUENCHING')
      DO 416 I=2,NOLEV
  416 PRINT417,I,QUEN(I)
  417 FORMAT('0',45X,'QUENCHING IN LEVEL ',I2,4X,F6.2)
      DO 1313 KB=1,16
 1313 RLAMB(KB,2)=RLAMB(KB,2)+1.
 1315 BUTT=2.
      STOP
      END
```

```
C    CALCULATION OF EXCITED STATE POPULATIONS AND PERCENT QUENCHING FOR HELIUM
C    CONSTANT INTENSITY 1 KW / CM**2
C                        VARIABLE NUMBER OF LEVELS
C NOLEV IS THE NUMBER OF LEVELS USED              MAXIMUM LEVEL=29
      IMPLICIT REAL*8(A-H,O-Z)
      DIMENSION SAEOP(35,4,7),COLIZ(30,4),COLEX(30,35,4),GSIRL(30,2),
     1AE(30),SPONA(35,35),BETA(29,4),RKAPA(30),SIGMK(30),ASUM(30),
     2GS(29,29,2),GSC(29,2),RHO(29,2),QJEN(30),IITER(2),EEPS(2),
     3ELECD(7),TEMP(4),RLAMB(17,2),EHE(35,4),COLDEX(35,30)
      DATA EPS/1.D-5/,MAX/350/,IITER/2*0/,ELECD/1.D8,5.D8,1.D9,5.D9,
     11.D10,5.D10,1.D11/,                        (RLAMB(I,1),I=1,17)/
     21.46D-6,2.28D-6,3.28D-6,4.46D-6,5.82D-6,7.38D-6,9.11D-6,1C.6D-6,
     311.D-6,13.11D-6,15.39D-6,17.85D-6,20.49D-6,23.32D-6,26.32D-6,
     429.51D-6,32.88D-6/,(RLAMB(I,2),I=1,17)/4.D0,5.D0,6.D0,7.D0,8.D0,
     59.D0,10.D0,11.D0,11.D0,12.D0,13.D0,14.D0,15.D0,16.D0,17.D0,18.D0,
     519.D0/.
     6COLDEX/1050*0.D0/,RHO/58*0.D0/,TEMP/300.D0,400.D0,500.D0,1000.D0/
      DO 200 I=1,4
  200 READ,(BETA(J,I),J=1,29)
      DO 201 K=1,7
      DO 201 J=1,4
  201 READ,(SAEOP(I,J,K),I=1,35)
      DO 202 I=1,4
  202 READ,(COLIZ(J,I),J=1,30)
      READ,COLEX
      READ,EHE
      READ,SPONA
      READ,(SAEOP(2,1,I),I=1,7)
C
C
C      CALCULATE A(P)
      DO 12 I=2,30
      II=I-1
      DSUM=1.D6
      DO 11 J=1,II
   11 DSUM=DSUM+SPONA(I,J)
   12 AE(I)=DSUM
      DO 1317 IT=4,4
      DO 1317 ID=7,7
C    CALCULATE COLDEX(35,30,4,7),K(P,Q)        P.GT.Q
      DO 1442 I=1,35
      DO 1442 J=1,30
 1442 COLDEX(I,J)=0.
      KK=IT
      JJ=ID
      DO 8 J=1,34
      K=35-J
```

```
      DO 7 L=1,30
      IF(L.GE.K)GO TO 8
    7 COLDEX(K,L)        =SAEQP(L,KK,JJ)*COLEX(L,K,KK)/SAEQP(K,KK,JJ)
    8 CONTINUE
      IF(IT.NE.1)GO TO 1500
      DO 1501 I=3,35
 1501 COLDEX(I,2)=COLDEX(I,2)*1.D20
 1500 BUT=1.
C
C
C      CALCULATE K(P)
      DO 13 I=1,30
   13 RKAPA(I)=COLIZ(I,IT)
      DO 14 J=1,28
      DSUM=0.0
      JJ=J+1
      DO 15 K=JJ,35
   15 DSUM=DSUM+COLEX(J,K,IT)
   14 RKAPA(J)=RKAPA(J)+DSUM
      DO 16 J=2,30
      DSUM=0.0
      JJ=J-1
      DO 17 K=1,JJ
   17 DSUM=DSUM+COLDEX(J,K)
   16 RKAPA(J)=RKAPA(J)+DSUM
C
C
      NOLEV=28
      NO1=NOLEV+1
      NO2=NOLEV-1
      NO3=NOLEV-2
      IF(NOLEV.LT.30)GO TO 801
      PRINT802
      STOP
  802 FORMAT('1',35X,'LEVELS EXCEED 29')
  801 NO1=NOLEV+1
C      CALCULATE K(P,SIGMA)
      DO 18 J=1,NOLEV
      DSUM=0.0
      DO 19 K=NO1,35
   19 DSUM=DSUM+COLEX(J,K,IT)
   18 SIGMK(J)        =DSUM
C      CALCULATE ASUM
      DO 20 I=2,28
      DSUM=0.0
      DO 502 J=NO1,35
  502 DSUM=DSUM+(SAEQP(J,IT,ID)*SPONA(J,I)/SAEQP(I,IT,ID))
   20 ASUM(I)=DSUM
      IF(IT.EQ.1)ASUM(2)=ASUM(2)*1.0-20
C
C
C      CALCULATE GSC
      K=ID
      DO 24 I=1,NO2
      N1=I+1
   24 GSC(I,1)=( ELECD(ID)*(SIGMK(N1)+COLIZ(N1,IT))+((ELECD(ID)**2)*
     1BETA(N1,IT)/SAEQP(N1,IT,ID))+ASUM(N1))*1.D45
      DO 27 I=1,NO2
      IF(IT.EQ.1)GSC(1,1)=(ELECD(ID)*(SIGMK(2)+COLIZ(2,1))*1.D45)+
     1((ELECD(ID)**2)*BETA(2,1)*1.D25/SAEQP(2,1,ID))+(ASUM(2)*1.D45)
   27 GSC(I,2)      =GSC(I,1)
```

```
C
C
C       CALCULATE GS COEFFICIENTS
        DO 22 L=1,NO3
        N1=L+1
        DO 22 M=N1,NO2
        N2=M+1
        GS(M,L,1)        =-ELECD(K)*COLDEX(N2,N1)*1.D45
     22 GS(M,L,2)        =-ELECD(K)*COLDEX(N2,N1)*1.D45

        DO 23 L=1,NO3
        N1=L+1
        DO 23 M=N1,NO2
        N2=M+1
        DO 23 I=1,2
        GS(L,M,I)=-(ELECD(ID)*COLEX(N1,N2,IT))-(SAEQP(N2,IT,ID)*SPONA(N2,N
     11)/SAEQP(N1,IT,ID))
     23 GS(L,M,I)=GS(L,M,I)*1.D45
        IF(IT.NE.1)GO TO 1502
        DO 1503 I=2,NO2
        II=I+1
   1503 GS(1,I,1)=GS(1,I,2)=-(ELECD(ID)*COLEX(2,II,1)*1.D45)-((SAEQP(II,
     11,ID)*SPONA(II,2)/SAEQP(2,1,ID))*1.D25)
   1502 BUT=2.
C       GS & GSC DIVIDED BY 10**45
        DO 68 K1=1,2
        DO 68 K2=2,NO2
     68 GSC(K2,K1)=GSC(K2,K1)*1.D-45

        DO 69 K1=1,2
        DO 69 K2=2,NO2
        DO 69 K3=2,NO2
        IF(K3.EQ.K2)GO TO 69
        GS(K3,K2,K1)=GS(K3,K2,K1)*1.D-45
     69 CONTINUE
C
C
C       CALCULATE IR LOSS TERM
        DO 1315 KMN=1,2
        DO 416 IL=1,17
        DO 10 I=1,30
        GSIRL(I,2)=0.0
     10 GSIRL(I,1)=0.0
        W=RLAMB(IL,1)
        IPM=RLAMB(IL,2)+8.
        DO 9 J=IPM,30
        JJ=J-8
      9 GSIRL(J,2) =(5.252D31)*(W**4)/(JJ**5)
    709 DO 21 L=1,NO2
        N1=L+1
        GS(L,L,2)=      (ELECD(K)*RKAPA(N1)     +AE(N1)+GSIRL(N1,2))
     21 GS(L,L,1)=      (ELECD(K)*RKAPA(N1)     +AE(N1) )
C       GAUSS SIEDEL METHOD TO SOLVE EQNS.
        DO 25 I=1,2
        IF(IL.NE.1.AND.I.EQ.1)GO TO 25
        DO 1504 J1=1,NO2
   1504 RHO(J1,I)=0.
        ITER=1
     99 BIG=0.0
        DO 100 L=2,NO2
    102 DSUM=0.0
        IF(L.EQ.2) GO TO 105
        LAST=L-1
```

```
      DO 106 M=2,LAST
 106  DSUM=DSUM+GS(L,M,I)*RHO(M,I)
      IF(L.EQ.NO2)GO TO 103
 105  INITL=L+1
      DO 107 N=INITL,NO2
 107  DSUM=DSUM+GS(L,N,I) *RHO(N,I)
 103  TTEMP=( GSC(L,I)-DSUM)/GS(L,L,I)
      IF(DABS(TTEMP-RHO(L,I)).GT.BIG)BIG=DABS(TTEMP-RHO(L,I))
 100  RHO(L,I)=TTEMP
      EEPS(I)=BIG
      IITER(I)=ITER
      IF(BIG.LT.EPS)GO TO 25
 110  IF(ITER.GE.MAX)GO TO 25
      ITER=ITER+1
      GO TO 99
  25  CONTINUE
      DEN1=DEN2=0.D0
      DO 67 K1=2,NO2
      DEN1=DEN1+GS(1,K1,1)*RHO(K1,1)
  67  DEN2=DEN2+GS(1,K1,2)*RHO(K1,2)
      AA1=1.D0
      IF(IT.NE.1)AA1=1.D-20
      DEN1=(GSC(1,1)-DEN1)*1.D-45*AA1*SAEQP(2,IT,ID)*1.D20/GS(1,1,1)
      DEN2=(GSC(1,2)-DEN2)*1.D-45*AA1*SAEQP(2,IT,ID)*1.D20/GS(1,1,2)
C
C
C
      CALCULATE PERCENT QUENCHING
      QUEN(2)=(DEN1-DEN2)*1.D2/DEN1
      DO 26 L=2,NO2
      LL=L+1
  26  QUEN(LL)=(RHO(L,1)*1.D6-RHO(L,2)*1.D6)/(RHO(L,1)*1.D4)
      PRINT409,NOLEV
 409  FORMAT('1',55X,'RESULTS',10X,I2,2X,'LEVELS')
      PRINT410,TEMP(IT),ELECD(ID),RLAMB(IL,1)
 410  FORMAT('-','TEMPERATURE=',F7.0,25X,'ELECTRON DENSITY=',E12.1,25X,
     1'WAVELENGTH OF IR=',E10.3)
      PRINT411,IITER(1),IITER(2)
 411  FORMAT('-','ITERATIONS NO IR=',I3,60X,'ITERATIONS 1 KW IR=',I3)
      PRINT412,EEPS(1),EEPS(2)
 412  FORMAT(' ','EPSILON NO IR',E10.2,56X,'EPSILON-IR',E10.2)
      PRINT511
 511  FORMAT('-')
      DO 601 I=1,NO2
      II=I+1
      A1=SAEQP(II,IT,ID)*RHO(I,1)
      A2=SAEQP(II,IT,ID)*RHO(I,2)
      IF(I.EQ.1)A1=DEN1
      IF(I.EQ.1)A2=DEN2
 601  PRINT602,II,A1,II,A2
 602  FORMAT(' ','DENSITY (',I2,')= ',E16.7,40X,'IR DENSITY (',
     1I2,')= ',E16.7)
      DO 413 I=2,NOLEV
      II=I-1
 413  PRINT414,I,RHO(II,1),I,RHO(II,2)
 414  FORMAT(' ','RHO(',I2,')= ',E16.7,50X,'RHO IR (',I2,')= ',E16.7)
      PRINT418
 418  FORMAT('1')
      PRINT415
 415  FORMAT('-',50X,'PERCENT QUENCHING')
      AVE=(QUEN(11)+QUEN(12)+QUEN(13)+QUEN(14))/4.
      PRINT,AVE
```

```
      DO 416 I=2,NOLEV
  416 PRINT417,I,QUEN(I)
  417 FORMAT('0',45X,'QUENCHING IN LEVEL ',I2,4X,F14.5)
      DO 1313 KB=1,17
 1313 RLAMB(KB,2)=RLAMB(KB,2)+1.
 1315 BUTT=2.
      DO 1316 KB=1,17
 1316 RLAMB(KB,2)=RLAMB(KB,2)-2.
 1317 CONTINUE
      STOP
      END
```

```
C   RADIATIVE RECOMBINATION OF HYDROGENIC IONS
      DIMENSION TAB(4,97),EL(40),BETA(40)
      READ,(TAB(1,I),TAB(2,I),TAB(3,I),TAB(4,I),I=1,97)
      PRINT 9,(I,TAB(1,I),TAB(2,I),TAB(3,I),TAB(4,I),I=1,97)
    9 FORMAT(' ',5X,I2,2X,F10.5,2X,F10.5,2X,F10.5,2X,F10.5)
      READ,T,N
      READ,(EL(I),I=1,N)
      D=5.197E-14
      C=157890./T
      C3=C**(-1./3.)
      CC=SQRT(C)
      DO 1 I=1,N
      X=C/EL(I)**2
      Z=3.*X
      IF(X.LT..02)GO TO 10
      IF(X.GT.20.)GO TO 20
      IF(X.LE..04)GO TO 31
      IF(X.LE..1)GO TO 32
      IF(X.LE..2)GO TO 33
      IF(X.LE..4)GO TO 34
      IF(X.LE.1.)GO TO 35
      IF(X.LE.2.)GO TO 36
      IF(X.LE.4.)GO TO 37
      IF(X.LE.10.)GO TO 38
```

```
      IF(X.LT.20.)GO TO 39
      XS0=.9544
      XS1=-.4147
    · XS2=-.350
      GO TO 2
 10   XS0=X*EXP(X)*(X-ALOG(X)-0.5772)
      XS1=0.4629*X*(1.+4.*X)-1.0368*X**1.333333*(1.+1.875*X)
      XS2=-0.0672*X*(1.+3.*X)+0.1488*X**1.666667*(1.+1.8*X)
      GO TO 2
 20   XS0=1.-1./X+2./(X*X)-6./(X*X*X)+24./(X*X*X*X)
      XS1=-0.1728*X**0.3333333*(1.-8./Z+70./(Z*Z)-800./(X*X*X)+11440./(Z
     **Z*Z*Z))
      XS2=-0.0496*X**0.6666667*(1.-3./Z+32./(Z*Z)-448./(Z*Z*Z))
      GO TO 2
 31   DI=500.
      J=1.+DI*(X-.02)
      GO TO 3
 32   DI=200.
      J=12.+DI*(X-.045)
      GO TO 3
 33   DI=100.
      J=24.+DI*(X-.11)
      GO TO 3
 34   DI=50.
      J=33.+DI*(X-.20)
      GO TO 3
 35   DI=20.
      J=44.+DI*(X-.45)
      GO TO 3
 36   DI=10.
      J=56.+DI*(X-1.1)
      GO TO 3
 37   DI=5.
      J=65.+DI*(X-2.0)
      GO TO 3
 38   DI=2.
      J=76.+DI*(X-4.5)
      GO TO 3
 39   DI=1.
      J=88.+DI*(X-11.)
  3   P=DI*(X-TAB(1,J))
      XS0=TAB(2,J)+P*(TAB(2,J+1)-TAB(2,J))
      XS1=TAB(3,J)+P*(TAB(3,J+1)-TAB(3,J))
      XS2=TAB(4,J)+P*(TAB(4,J+1)-TAB(4,J))
  2   BETA(I)=D*CC*(XS0+C3*XS1+C3*C3*XS2)/EL(I)
  1   CONTINUE
      PRINT 4,(I,BETA(I),I=1,N)
  4   FORMAT (' ',10X,'BETA(',I2,') = ',E17.7)
      STOP
      END
```

```
C      CALCULATION OF RADIATIVE RECOMBINATION COEFF. HELIUM
C      BETA(29)
C      READ IN BETA(29),EHE(35,4)
       DIMENSION BETA(29),EHE(35,4),T(4)
       READ,T
       READ,EHE
       DO 1 I=1,4
       READ,BETA
       DO 2 J=1,29
    2  BETA(J)=BETA(J)*EHE(J,4)/(4*EHE(J,3)*EHE(J,3))
       PRINT4,T(I)
    4  FORMAT('1',10X,'TEMP.= ',F7.1)
       DO 5 LL=1,29
    5  PRINT6,LL,BETA(LL)
    6  FORMAT(' ',10X,'BETA(',I2,')= ',E16.7)
       PUNCH,BETA
       DO 3 K=1,29
    3  BETA(K)=0.0
    1  CONTINUE
       PUNCH,EHE
       STOP
       END
```

END

DATE
FILMED
2-77

```
C       CALCULATION OF COLISIONAL EXCITATION AND IONIZATION HELIUM
C       COLIZ(30),COLEX(30,35),T(4),EHE(35,4)
        DIMENSION COLIZ(30),COLEX(30,35),      EHE(35,4)
        DOUBLE PRECISION   P,SUM,B,R,E1,E2,F1,F2,C(16),X(16),DSQRT,DEXP,Q,
       1T(4)
        READ,T
        READ,EHE
        EHE(9,3)=SQRT(109678./12210.)
        EHE(10,3)=SQRT(109678./12206.)
        C(1)=.02715245941754D0
        C(2)=.06225352391864BD0
        C(3)=.07515851168249300
        C(4)=.12462897125553400
        C(5)=.14959598881657700
```

```
      C(6)=.16915651939500JJDO
      C(7)=.1826034150449240D0
      C(8)=.1894506104550690D0
      C(9)=.1894506104550690D0
      C(10)=.18260341504492400
      C(11)=.1691565193959500300
      C(12)=.1495959888816577D0
      C(13)=.1246289712555340D0
      C(14)=.09515851168249300
      C(15)=.0622535239386480D0
      C(16)=.0271524594117540D0
      X(1)=-.9894009349991650D0
      X(2)=-.9445750230732330D0
      X(3)=-.8656312023878320D0
      X(4)=-.7554044083550030D0
      X(5)=-.6178762444026440D0
      X(6)=-.4580167776572270D0
      X(7)=-.2816035507792590D0
      X(8)=-.0950125098376370D0
      X(9)=.0950125098376370D0
      X(10)=.2816035507792590D0
      X(11)=.4580167776572270D0
      X(12)=.6178762444026440D0
      X(13)=.7554044083550030D0
      X(14)=.8656312023878320D0
      X(15)=.9445750230732330D0
      X(16)=.9894009349991650DD0
C                    CALCULATE K(P,C)
      DO 4 L=1,4
      DO 3 LL=1,30
    3 COLIZ(LL)=0.0
      DO 1 J=2,30
      P=EHE(J,3)
      SUM=0.0
      DO 2 K=1,16
      B=C(K)
      R=X(K)
      E1=1.0D50*DEXP(-78945.D0*(R+3.D0)/(P**2.D0*(T(L))))
      E2=1.0D30*DEXP(-631560.D0/(P**2*T(L)*(1.D0-R)))
      F1=2.*1.4142D0*DSQRT((((R+1.D0)/(R+5.D0))**3.D0))/3.D0
      F2=16.D0*(7.D0+3.D0*R)/(3.D0*(1.D0-R)**2*DSQRT((5.D0-R)**3))
    2 SUM=SUM+B*(F1*E1+F2*E2)
      FINAL=5.45D0*SUM/(DSQRT(T(L)**3)*1.D50)
    1 COLIZ(J)=FINAL
      PRINT10,T(L)
   10 FORMAT('1',10X,'TEMP.= ',F7.1)
      DO 11 NRT=1,30
   11 PRINT12,NRT,COLIZ(NRT)
   12 FORMAT(' ',10X,'COLIZ(',I2,')= ',E16.7)
    4 PUNCH,COLIZ
C                    CALCULATE K(P,O)
      DO 7 N=1,4
      DO 8 NN=1,30
      DO 8 NM=1,35
    8 COLEX(NN,NM)=0.
      DO 5 J=2,30
      P=EHE(J,3)
      JS=J+1
      DO 5 K=JS,35
      Q=EHE(K,3)
      SUM=0.0
```

```
      A=(Q**2)/(Q**2-P**2)
      DO 6 L=1,16
      B=C(L)
      R=X(L)
      E1=DEXP(-78945.D0*(R+1.)/(P**2*T(N))-157890.D0/(P**2*A*T(N)))*
     11.0D30
      E2=DEXP(-315780.D0*(1.+A)/(P**2*A*T(N)*(1.-R)))*1.D30
      F1=(4.*A**2+7.*A+5.+4.*A**2*R+A*R)*DSQRT((R+1.)*(A+1.))*A/
     4(6.*DSQRT((3.*A+2.+A*R)**3))
      F2=(8.*A**2+11.*A+6.+3.*A*R)*DSQRT((2.D0*(1.D0)+A))**3.D0)
     1/(3.D0*DSQRT((3.D0*A+2.D0-A*R)**3.D0)*(1.-R)**2)
    6 SUM=SUM+B*(F1*E1+F2*E2)
      FINAL=10.9D0*P**2*A*SUM/(DSQRT(T(N)**3)*K**3)
      IF(FINAL.LT.1.E-40)FINAL=0.
      FINAL=FINAL*1.E-30
    5 COLEX(J,K)=FINAL
      PRINT10,T(N)
      DO 13 NOC=1,30
      NOC1=NOC+1
      DO 13 NAC=NOC1,35
   13 PRINT14,NOC,NAC,COLEX(NOC,NAC)
   14 FORMAT(' ',10X ,'COLEX(',I2,',',I2,')= ',E16.7)
    7 PUNCH,COLEX
      STOP
      END
```

```
C     SAHA EQUILIBRIUM DENSITIES-HELIUM
C SAEOP(2) SET TO 0. SINCE>1.E75-CORRECTED IN M.P.
C     SAEOP(35)-READ IN  EHE
      DIMENSION SAEOP(35),EHE(35,4),T(4),ELECD(7)
      DATA T/300.,400.,500.,1000./,ELECD/1.E8,5.E8,1.E9,5.E9,1.E10,
     15.E10,1.E11/,F/4.2E-16/
      READ,EHE
      AND=9.99999
      DO 1 K=1,7
      DO 1 J=1,4
      DO 8 KK=1,35
    8 SAEOP(KK)=0.
      DO 2 I=2,35
      IF(J.EQ.1.AND.I.EQ.2) GO TO 2
      SAEOP(I)=F*(ELECD(K)**2)*(EXP(EHE(I,2)/(.695*T(J))))*
     1(EHE(I,4)/4.)/(SQRT(T(J)**3))
    2 CONTINUE
      PRINT3,T(J),ELECD(K)
    3 FORMAT('1',10X,'TEMP= ',F7.1,10X,'ELEC. DEN. = ',E12 .4)
      DO 4 LL=1,35
```

```
4 PRINT5,LL,SAEQP(LL)
5 FORMAT(' ',10X,'SAEQP(',I2,')= ',E16.7)
1 PUNCH,SAEQP
  STOP
  END
```

```
C     CALCULATE SPONTANEOUS TRANSITION PROB. - HELIUM
      DIMENSION EHE(35,4),SPONA(35,35),C(11)
      READ,(EHE(I,1),I=1,11)
      READ,(EHE(I,3),I=1,11)
      READ,(EHE(I,4),I=1,11)
      DO 1 I=1,11
    1 EHE(I,2)=198305.-EHE(I,1)
      DO 2 I=12,35
      J=(I-8)**2
      EHE(I,1)=198305.-(109678./J)
      EHE(I,2)=109678./J
      EHE(I,3)=I-8
    2 EHE(I,4)=4*J
      DO 3 J=1,35
      DO 3 I=1,35
    3 SPONA(I,J)=0.0
      READ,(SPONA(I,1),I=1,20)
      DO 4 J=2,5
    4 READ,(SPONA(I,J),I=1,18)
      DO 5 J=6,11
    5 READ,(SPONA(I,J),I=1,14)
      DO 6 J=12,27
      K=J+1
    6 READ,(SPONA(L,J),L=K,28)
      READ,C
      DO 7 I=21,35
      J=I-8
    7 SPONA(I,1)=C(1)*EHE(1,4)*(EHE(I,1)**2)/(J**5)
      DO 8 K=2,5
      DO 8 I=19,35
      J=I-8
    8 SPONA(I,K)=C(K)*EHE(K,4)*((EHE(I,1)-EHE(K,1))**2)/(J**5)
      DO 9 K=6,11
      DO 9 I=15,35
      J=I-8
    9 SPONA(I,K)=C(K)*EHE(K,4)*((EHE(I,1)-EHE(K,1))**2)/(J**5)
      DO 10 I=29,35
      J=I-8
      DO 10 K=12,29
      IF(I.EQ.K) GO TO 10
      L=K-8
      SPONA(I,K)=1.29*(L**3)*J*((EHE(I,1)-EHE(K,1))**2)/
     1(((J**2)-(L**2))**3)
   10 CONTINUE
      DO 11 I=1,34
      II=I+1
      DO 11 J=II,35
   11 PRINT12,J,I,SPONA(J,I)
   12 FORMAT(' ',14X,'A(',I2,',',I2,') = ',E16.7)
      PRINT15
      DO 13 I=1,35
   13 PRINT14,(EHE(I,J),J=1,4)
   14 FORMAT(' ',4F16.2)
   15 FORMAT('1')
      PRINT,EHE
      PUNCH,EHE
      PUNCH,SPONA
      STOP
      END
```

REFERENCES

[1] H. Merkelo, J. H. Hammond and B. G. Grossman, "Interaction of infrared radiation with weakly ionized plasmas," Bulletin of The American Physical Society, vol. 17, p. 1067, 1972.

[2] H. Merkelo, J. P. Kaplafka and L. Goldstein, "Effects of infrared radiation on gaseous plasmas," Proceedings of the Special Meeting on Unconventional Infrared Detectors, 1971.

[3] J. P. Kaplafka, H. Merkelo and L. Goldstein, "Quenching of radiation from ionized gases by infrared photons," Applied Physics Letters, vol. 19, 1971.

[4] J. P. Kaplafka, H. Merkelo and L. Goldstein, "Quenching of helium afterglow by infrared photons," Applied Physics Letters, vol. 15, p. 113, 1969.

[5] D. R. Bates, A. E. Kingston and R. W. P. McWhirter, "Recombination between electrons and atomic ions - I. Optically thin plasmas," Proceedings of the Royal Society (London), vol. A267, p. 297, 1962.

[6] C. E. Moore (ed.), Atomic Energy Levels, vol. I, National Bureau of Standards. Washington, D. C.: U.S. Government Printing Office, 1949.

[7] R. H. Fowler, Statistical Mechanics, 2nd edition. Cambridge, England: Cambridge University Press, 1936, p. 726.

[8] W. L. Wiese, M. W. Smith and B. M. Miles (eds.), Atomic Transition Probabilities, vol. I, National Bureau of Standards. Washington, D. C.: U.S. Government Printing Office, 1966.

[9] R. W. P. McWhirter and A. G. Hearn, "A calculation of instantaneous population densities of the excited levels of hydrogen-like ions in a plasma," Proceedings of the Physical Society (London), vol. 82, 1963.

[10] A. H. Gabriel and D. W. O. Heddle, "Excitation processes in helium," Proceedings of the Royal Society (London), vol. A258, 1960.

[11] A. Dalgarno and A. E. Kingston, "Properties of the metastable helium atoms," Proceedings of the Physical Society (London), vol. A72, p. 1053, 1958.

[12] M. F. Seaton, "Radiative recombination of hydrogenic ions," Monthly Notices of the Royal Astronomical Society, vol. 119, 1959.

[13] M. Gryzinski, "Classical theory of electronic and ionic inelastic collisions," Physical Review, vol. 115, p. 374, 1959.

[14] R. McCarroll, "The excitation of discrete levels of atomic hydrogen by fast electrons," Proceedings of the Physical Society (London), vol. A70, p. 460, 1957.

[15] D. H. Menzel and C. L. Pekeris, "Absorption coefficients and hydrogen line intensities," Monthly Notices of the Royal Astronomical Society, vol. 96, p. 77, 1935.

B-I
Picosecond Dynamics of Photoelectric Emission

Detailed study of the time evolution of the photoelectric emission has never been investigated experimentally with adequate time resolution. Without even taking into account the difficult and long standing problem of the time dependence of the probability of photoelectric emission on time scales on which the oscillations of the optical field are resolved, as considered for example by Mandel and Meltzer,[1] one can state that the response time of a finite thickness photoactive surface can be significantly affected by lattice scattering, carrier lifetimes, pair production, and formation and destruction of exciton and impurity states. Therefore, the evolution of emission can conceivably range from 10^{-15} to 10^{-9} sec. In the literature, estimates for the response time of photocathodes include such values as "instantaneous," $\sim 10^{-12}$ sec for conventional materials in which the threshold for pair production is large compared with the electron affinity,[2] 10^{-11} to 3×10^{-11} sec for similar materials in different circumstances,[3] $\sim 10^{-10}$ sec for some negative-electron-affinity materials,[4] and, surprisingly, entirely outside of the microwave modulation region for the specific case of cesium-antimony deposited on beryllium-oxide.[5] Finally, a result of a different nature but not unrelated was reported by Gabriel[6] who showed that, in photon counting, given the emission of a first photoelectron at t = o, the probability of emission of a second photoelectron is significantly enhanced at $t \simeq 15 \times 10^{-9}$ sec; the work was carried out with $\sim 10^{-9}$ sec resolution.

It is true that studying photoemission on picosecond time scales is extremely difficult and requires the most modern high-speed instruments

available in the laboratories. In section B-V, we introduce the method for picosecond sampling of photoelectrons both as a high-speed optical detector and as the only technique known to us that would be adaptable to study photoelectric emission on adequate time scales. The adaptation of optoelectronic sampling to the study of energy-separated time evolution of photoelectric emission is given in Section B-VI.

The emphasis in these studies is placed on the physical characterization of materials and on the identification of principal processes controlling the rate of emission from surfaces. It is anticipated that fully understanding the physics of the time evolution of photoemission with and without field-enhancement will provide the basis for new generations of high data rate processing optoelectronic devices.

REFERENCES

1. L. Mandel and D. Meltzer, "Theory of Time-Resolved Photoelectric Detection of Light," Phys. Rev., vol. 188, pp. 198-212, December 5, 1969.

2. W. E. Spicer and F. Wooten, "Photoemission and Photomultipliers, Proc. IEEE, pp. 1119-1126, August 1963.

3. R. C. Miller and N. C. Wittwer, "Secondary-Emission Amplification at Microwave Frequencies," IEEE J. of Quantum Electronics, QE-1, 49-59, April 1965.

4. H. Sonnenberg, "Negative-Electron Affinity Photoemitters," IEEE J. of Solid-State Circuits SC-5, 272-275, October 1970.

5. O. L. Gaddy and D. F. Holshouser, "Photomultiplier Detection of Microwave Modulated Light," Proc. IRE (Corresp.), 50, 1525, June 1962.

6. G. J. Gabriel, "Intrinsic and Extrinsic Statistical Dependence in Photoemission," Phys. Rev. A9, 976-988, February 1974.

UNIVERSITY OF ILLINOIS

DISCLOSURE OF INVENTION AND
LETTER OF TRANSMITTAL

To the University of Illinois
Patent Committee: **Date:** February 16, 1973

Entered herein and attached hereto is information concerning a potentially patentable invention, for your consideration.

1. Description Title of Invention

2. Inventor

   Name: Henry Merkelo   Office Address and Telephone Number:
                                 155 Electrical Engineering Bldg., 333-2482

   Rank and Department: Permanent Address:
   Associate Professor of Electrical Engineering

3. Name and Address of Co-inventor (if any)

4. Description of Invention (In as simple and brief language as possible, describe invention, clearly pointing out what parts thereof are novel and which are old features, and which features were invented or suggested by colleagues. Attach two sets of drawings, sketches, photos and reports of invention, and any parts which will be used in the description, referring to by number, if necessary. Attach additional sheets, if needed.)

(a) Description:

High speed sampling of photoelectrons is demonstrated and applied to the construction of a high resolution "sampling photomultiplier".

The outstanding feature of devices built on the sampling principle lies in the attainment of extremely high time resolution of periodic signals. Opto-electronic sampling as developed here is analogous to that used in conventional sampling electronic instrumentation (oscilloscopes, counters, etc.); however, the sampling of photoelectrons is distinct and technologically different from conventional electronic sampling. Signal producing (sampled) electrons are physically separated with high time resolution in a specially designed, electrically broadband, photoemissive structure.

A device has been built and tested on light pulses of ~300 psec rise (10 to 90%) fully resolving this time variation; the actual speed limit of the device is not known yet. Work continues which is aimed at establishing experimentally the limiting resolution which, on the basis of quantum mechanical arguments, should lie in the $10^{-11} - 10^{-12}$ sec range.

The remarkable feature of this high resolution sampling photomultiplier is that high time resolution of periodic signals can be obtained with slow auxiliary instrumentation (oscilloscopes, counters, etc.)

*See attached technical description design drawings and performance tests.

(b) **Earliest date and place invention was conceived. (Brief outline
of circumstances.)**
Summer 1972; proposed M.S. thesis to Sid Kaiser; Department of Electrical
Engineering (Undergraduate Laboratory of Quantum Electronics)

(c) **Date and place of first sketch, drawing or photo.**
January 1973, Electrical Engineering Publications Office, M.S. Thesis
S. Kaiser in preparation.

(d) **Date and place of first written description, if available.**
January 1973, Electrical Engineering Publications Office, M.S. Thesis,
S. Kaiser, in preparation.

5. **Disclosure**

(a)   Disclosure of Invention to Others

Name, Title and Address	Form of Disclosure (including theses and other publications)	Date and Place of Disclosure	Was Signature Obtained (Yes or No)
Jamie Wiczer, Res. Asst., Univ. of Ill.	Verbal	January 1973 267 Elec. Eng. Bldg.	No; Mr. Wiczer new M.S. thesis candidate.
E. H. Eberhardt*, Physicist	Verbal during visit to University of Illinois.	Nov. 18, 1971	No; only concepts were discussed.
Members of Gaseous Electronics Lab	Verbal: Seminar	Jan. 19, 1973, Seminar	No
See attached for	remainder of Disclosure of Invention to Others		

(b) **Date and Place of Completion of first operating model or full size
device.**
January 11, 1973; 267 Electrical Engineering Building.

(c) **Present Location of Model.**
267 Electrical Engineering Building.

(d) **Date, place, description and results of first test or operation.**
Results: Jan. 11, 1973; 267 Elec. Engrg. Bldg., Description: S. Kaiser
M.S. Thesis (in preparation)

6. **Support of the University of Illinois** (Complete explanation, with dates,
of University of Illinois facilities and support utilized, in whole or
in part, in development of this invention.)
Department of Electrical Engineering
Undergraduate Quantum Electronics Laboratory
Special Processes Laboratory
Gaseous Electronics Laboratory
Waiver of indirect costs on N00014-67-A-0305-0017

---

*ITT, Electron Tube Division, Fort Wayne, Indiana

Disclosure of Invention to Others Continued

O. L. Gaddy, Professor & Associate Head, Dept. of Elect. Engrg., University of Illinois, Urbana	Verbal	January 1973 & during construction	No
S. Kaiser, Research Assistant University of Illinois	Assisted in construction	Summer 1972-January 1973	No
J. Merkelo, Manager Hewlett Packard Co. Santa Clara, California	Participated in design	Fall 1972	No

Harry Merkelo 5/2/73
Inventor   **Date**

O L Gaddy 2 May '73
Witness   **Date**

104

7. This invention was [X] was not [ ] made while working on research sponsored by an agency outside the University. If so,

[X] Name of Sponsoring Agency: Office of Naval Research

[X] Description of contract: Research in Infrared and Optical Quantum Electronics

[X] Number: N00014-67-A-0305-0017

8. If decision of Patent Committee is to recommend release of interest of the University in this invention, the following is recommended:

[ ] Outright release to sponsoring agency, retaining no rights for inventor.

[X] Release to inventor, with recognition of contractual obligations of the University to sponsoring agency.

[ ] Other.

Respectfully submitted,

_____ 2/16/73
Inventor   Date

_____
Inventor   Date

It is certified that the statements made herein are correct, to the best of my knowledge and belief.

_____
Department Head,
or Other Administrative
Officer

RECOMMENDATIONS

It is my/our opinion and recommendation(s) that the potentially patentable invention described herein:

☐ Has little or no commerical value and should be released by the University to ☐ inventor(s) or ☐ sponsoring agency.

☒ Definite possibility of commercial value and retention by the University of Illinois or University of Illinois Foundation for development, with partial distribution of any net income to the inventor(s).

☐ Other.

E. C. Jordan   2/16/73
Department Head   Date
or Other Administrative
Officer

C. L. Dedy   2 May '73
                                       Date

_____
Other Individuals   Date
Who Have Knowledge
of this Invention

High Speed Opto-Electronic Sampler and High Resolution
Sampling Photomultiplier

Design Criteria and Results

The high resolution sampling photomultiplier consists of a high speed head, designed to sample photoelectrons at its own photocathode, and of a conventional electron multiplier section with no special requirements. The sampling head thus converts any conventionally designed electron multiplier into a photomultiplier capable of high time resolution of periodic, low-level optical signals. The first complete system was built and tested on light signals of ~300 psec rise (3×10^{-10} sec, 10 to 90% amplitude) fully resolving this time dependence; sufficiently short pulses were not available to test the device to its limit of time resolution. Whereas the sampling structure was driven up to 10 GHz bandwidth for a corresponding pulse resolution of ~35 psec, the maximum bandwidth requirement on the auxiliary instruments, including the electron-multiplier structure was only 100 KHz (~3.5×10^{-6} sec rise time).

Figure 1 shows the assembly of the sampling head and the modified electron multiplier. The electron multiplier is that of an RCA 7102 photo-tube. The multiplier is installed in a new glass press and housing which is flanged in order to accommodate the sampling head. Figure 2 shows the detailed components of the sampling head.

The flange which is labeled with O-ring groove #1 accommodates a glass window; the housing, #2, is made of cold rolled steel; high frequency, 50Ω feedthroughs, #3, connect to a perforated strip, #6, which, in combination with insert #5, forms a 50Ω microstrip transmission section terminated in a 50Ω load;

insert #5 is gridded with a mesh, #4, for photoelectron ejection; moreover, accurate positioning of insert #5 with respect to strip #6 is accomplished with a gauged spacer, #7. The assembly of these components mounts on the flange of the multiplier section as shown in Figure 1. Although many construction details are important in producing this device, the most significant feature of this design is that the opto-electronic sampling section (photocathode, strip, ground plane, feedthroughs) form a broadband, non-dispersive electrical system; this was accomplished with an opto-electronically adapted microstrip design suitable for ultra high vacuum construction. Scaling of the microstrip section for electromagnetic matching was carried out following considerations applicable to broadband microstrip design for reflectionless and dispersionless fundamental mode propagation; a 300 μm strip-ground plane spacing and a 1.58 mm strip width were chosen as suitable geometric parameters; a cesium antimony photocathode was used in all experiments.

When properly biased and driven with ultrashort pulses, Figure 3, the strip-grid section (#6 and #4) is capable of sampling photoelectrons with a time resolution which depends both on sampling pulse amplitude and pulse shape. Conventional photoelectron ballistics analysis predicts that currently available technology of sampling electronics is capable of achieving pico-second resolution and possibly reach the limiting resolution which, on the basis of quantum mechanical arguments, should lie in the $10^{-11} - 10^{-12}$ sec range.
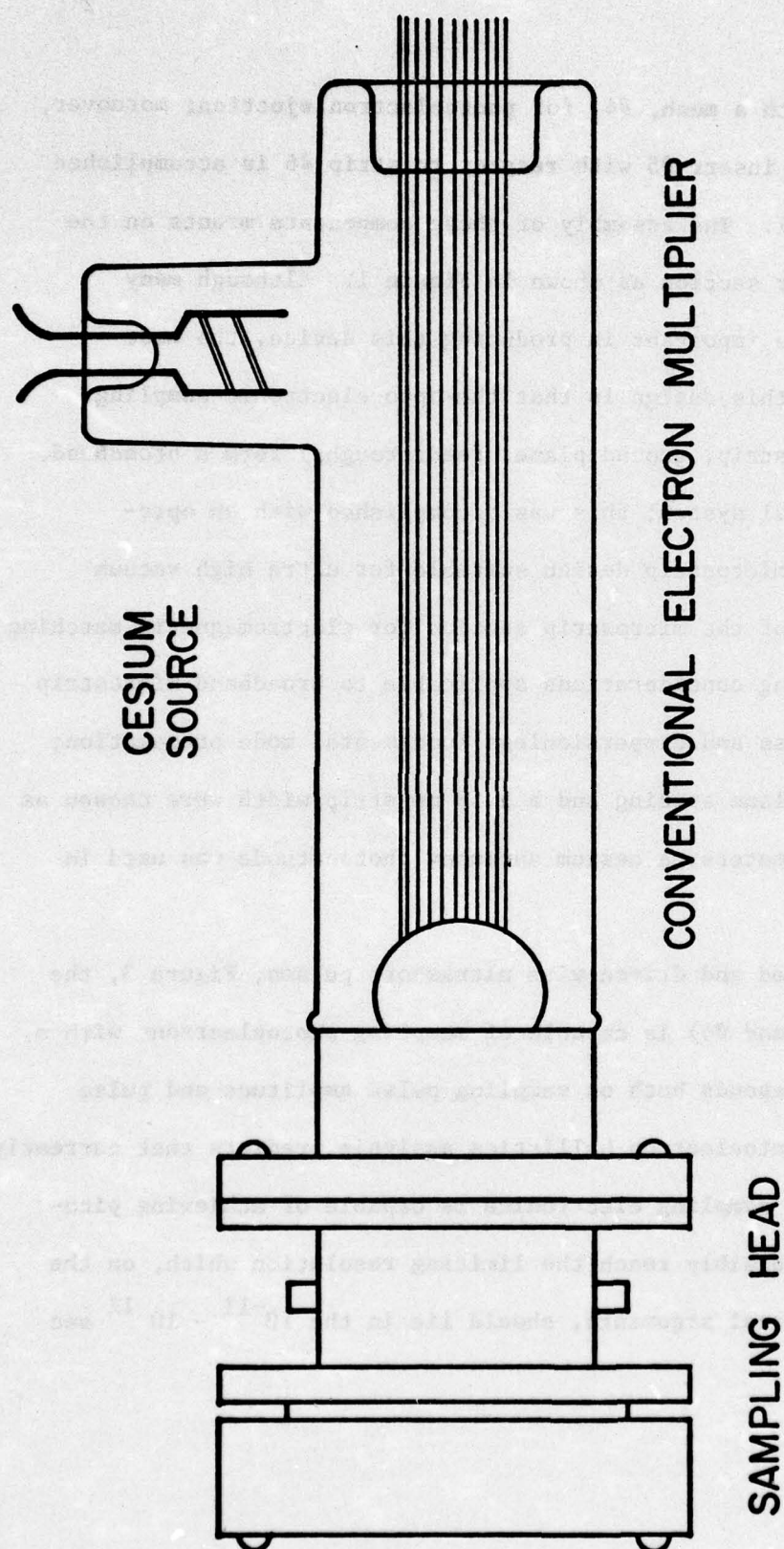
CESIUM SOURCE

CONVENTIONAL ELECTRON MULTIPLIER

SAMPLING HEAD

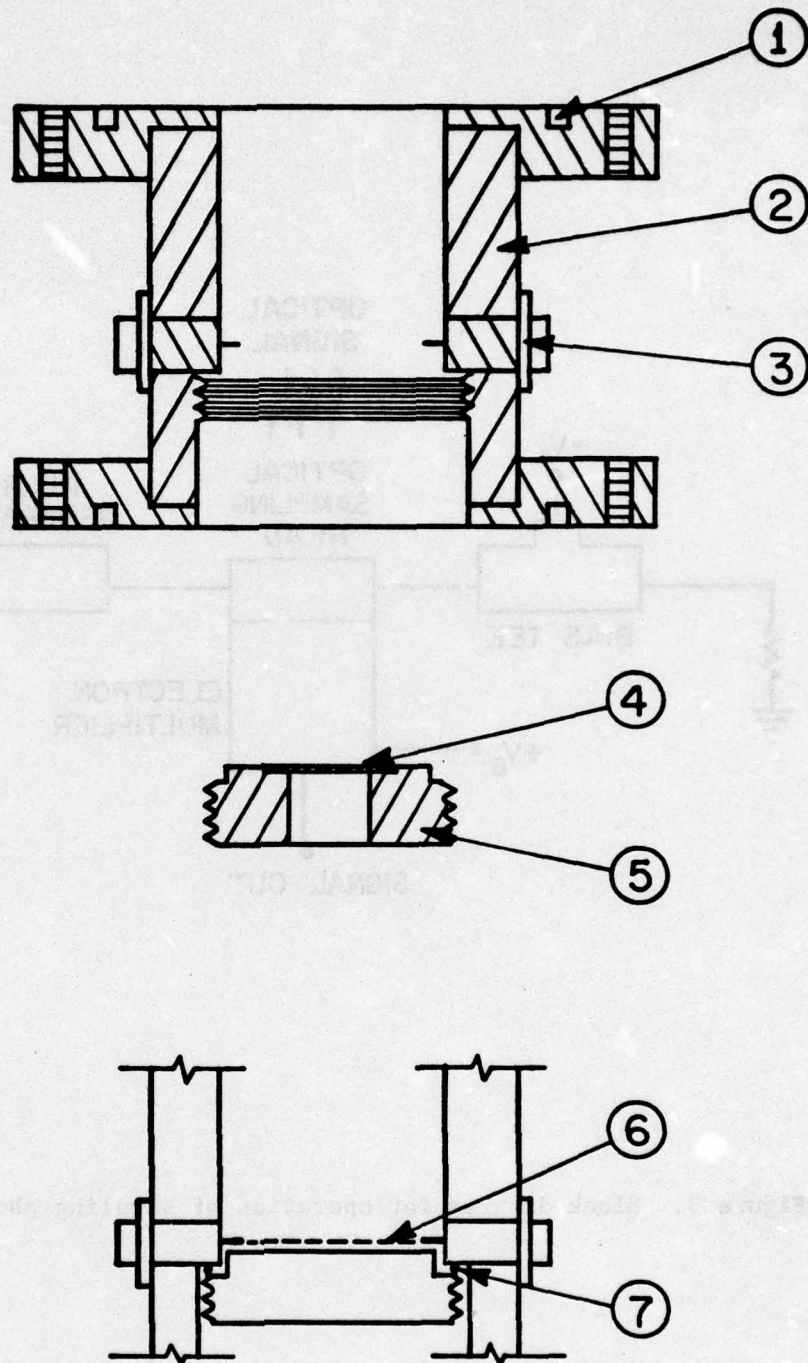Figure 1. High speed opto-electronic sampling photomultiplier. Assembly of sampling head and electron multiplier.

Figure 2. Components of the opto-electronic sampling head:

1 O-ring seal for glass window
2 Cold rolled steel housing
3 Broadband feedthroughs
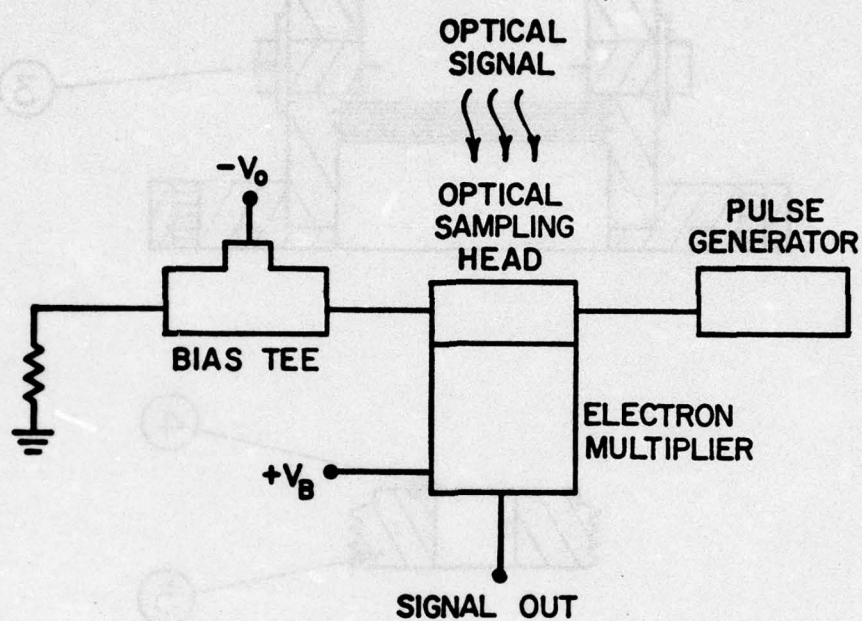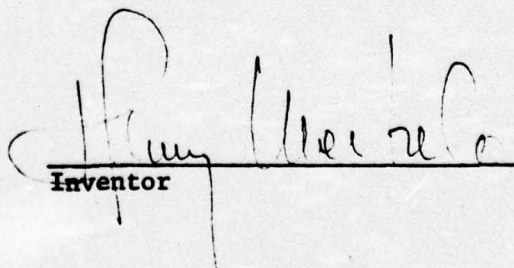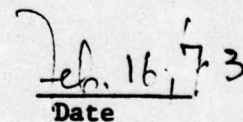4 Fine mesh
5 Insert (ground plane)
6 Perforated strip
7 Spacer

OPTICAL
SIGNAL

OPTICAL
SAMPLING
HEAD

PULSE
GENERATOR

$-V_o$

BIAS TEE

ELECTRON
MULTIPLIER

$+V_B$

SIGNAL OUT

Figure 3. Block diagram for operation of sampling photomultiplier.

Optical pulses of ~300 psec risetime (tested at high intensity with a fast photodiode and a sampling oscilloscope) were derived from a mode-locked He—Ne laser and detected with the reported device. Only ~7 V, 250 psec wide sampling pulses with a 2.2 V back-bias were necessary to achieve full time resolution of the mode-locked laser pulses. Figure 4 shows opto-electronically sampled light pulses as displayed on an ordinary oscilloscope. The equivalent horizontal scale is 200 psec/div (200×10^{-12} sec/div). The risetime (10% to 90%) of the pulse shown is ~300 psec, as measured independently, and the fall time is identical, demonstrating for the first time (to our knowledge) the symmetry of mode-locked laser pulses. Shorter optical pulses will be needed to establish the true limit of the device.

_____   _____
Inventor   Date

_____   _____
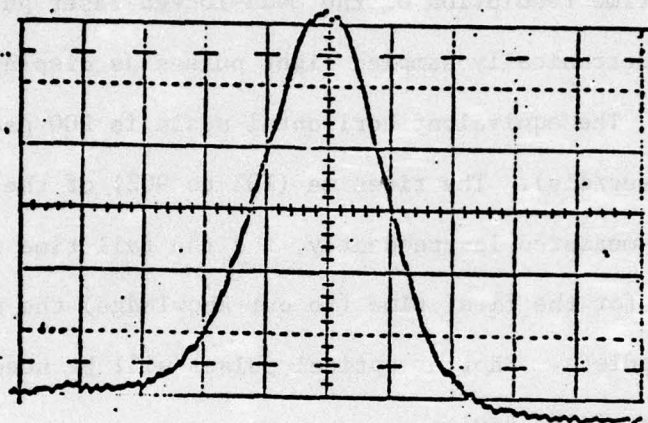Inventor   Date

Figure 4. Optoelectronically sampled mode-locked laser pulses displayed on an ordinary oscilloscope. Horizontal equivalent scale: 200psec/div (200 x 10⁻¹²sec/div)

RECORD AND DISCLOSURE OF INVENTION
NAVEXOS 2374 (Rev. 5-62)

B-III.
DEPARTMENT OF THE NAVY
OFFICE OF NAVAL RESEARCH
WASHINGTON 25, D.C.

INSTRUCTIONS. A Navy employee or an employee of a Navy contractor should use this form when submitting an invention disclosure to the Department of the Navy. Original and two copies should be printed or typed and forwarded to the Navy Patent representative in the area or directly to the Office of Naval Research at the above address. Where space on form is inadequate, enter "see attached page", identify item by number and use plain pages as needed. When completely executed, this form becomes an important legal document useful in proving priority of invention.

FOR USE BY NAVY PATENT ACTIVITY	
PATENT ACTIVITY (Name)	NAVY CASE NO.
DATE DISCLOSURE RECEIVED	LOCAL CASE NO.

PART 1. RECORD OF INVENTION

1. INVENTOR(S)	ADDRESS	POSITION TITLE	EMPLOYER (Activity & Code No., or Company & address)
Henry Merkelo		Associate Professor	University of Illinois, Dept. of Elect. Engrg., Urbana, IL 61801

2. DESCRIPTIVE TITLE OF INVENTION (Disclose details of invention in Part II on reverse)

High Speed Opto-Electronic Sampler and High Resolution Sampling Photomultiplier

RECOMMENDED SECURITY CLASSIFICATION ON INVENTION DISCLOSURE

3. CONCEPTION, INITIAL RECORDS AND RESULTS OF FIRST MODEL

a. EARLIEST DATE AND PLACE INVENTION WAS CONCEIVED (Identify persons and records to support date and place)

November 1971; Section II of proposal to Office of Naval Research (Physics Program) entitled "Research in Infrared and Optical Quantum Electronics"

b. DATE AND PRESENT LOCATION OF FIRST SKETCH, DRAWING OR PHOTO AND FIRST WRITTEN DESCRIPTION (Such as notebook entries, etc.)

January 1973, Electrical Engineering Publications Office, M.S. Thesis (in preparation)

c. DATE AND PLACE OF COMPLETION OF FIRST OPERATING MODEL OR FULL SIZE DEVICE AND ITS PRESENT LOCATION

January 11, 1973, 267 Electrical Engineering Building (Undergraduate Quantum Electronic Laboratory)

d. DATE AND PLACE OF FIRST TEST OR OPERATION AND THE RESULTS (Give name and address of witnesses, and present location of records)

January 11, 1973; 267 Electrical Engineering Building; M.S. Thesis (in preparation).
Those present: Henry Merkelo, Inventor
         Sidney Kaiser, Graduate Student
         S. William Merritt, Graduate Student

4. OTHER RECORDS (Notebook entries, descriptions, reports, drawings, etc.)

IDENTIFICATION	DATE OF DOCUMENT	PRESENT LOCATION
Laboratory Notebook: Sid Kaiser Quantum Electronics Lab. Used from November 1971	Used from November 1971; dated pages	267 Electrical Engineering Bldg

5. OTHER INDIVIDUALS TO WHOM INVENTION WAS DISCLOSED

NAME	ACTIVITY OR COMPANY INDIVIDUAL REPRESENTS	DATE DISCLOSED	TYPE (Oral or written disclosure)
Jamie Wiczer	University of Illinois	Jan. 1973	Oral
E. H. Eberhardt	ITT, Electron Tube Div.	Nov. 18, 1971	Oral
O. L. Gaddy	University of Illinois	Jan. 1973	Oral
Gaseous Elec. Lab.	University of Illinois	Jan. 19, 1973	Oral
J. Merkelo (over)	Hewlett Packard	Jan. 1973	Oral

6. DATE AND PLACE OF OTHER TESTS OR OPERATIONS, AND THE RESULTS (List name and address of witnesses and identify present location of records)

Continued operation by J. J. Wiczer since January 11, 1973 (Graduate student and M.S. candidate
S. W. Merritt, September 1972 (Graduate student and M.S. candidate)
G. Metze, January 1973 (Graduate student and M.S. candidate)

7. IDENTIFY ANY PAST, PRESENT OR CONTEMPLATED USE OR PUBLICATION OF THE INVENTION

M.S. Thesis in preparation (S. Kaiser)
Article in preparation (H. Merkelo, S. Kaiser, J. Merkelo)
Article in preparation (H. Merkelo, J. J. Wiczer)

8. CLOSELY RELATED PATENTS, PATENT APPLICATIONS AND PUBLICATIONS

PATENT OR APPLICATION NO. AND DATE	TITLE OR PUBLISHED ARTICLE	PUBLICATION NAME AND DATE
None		

114

9. ROYALTY-FREE GOVERNMENT LICENSE UNDER INVENTION

In the event that the Government is not entitled to the entire right, title and interest in the above described invention by law or regulation, and inventor(s) desires the Government to file a patent application at Government expense in the name of the inventor(s), it is required that the following statement be signed by the inventor(s):

I HEREBY AGREE THAT IF A PATENT APPLICATION ON THE INVENTION DESCRIBED HEREIN IS FILED FOR ME BY THE GOVERNMENT, THE INVENTION MAY BE MANUFACTURED AND USED BY OR FOR THE GOVERNMENT WITHOUT PAYMENT OF ROYALTIES OR OTHER COMPENSATION TO ME.

SIGNATURE	DATE	SIGNATURE	DATE	SIGNATURE	DATE
	2-28-73				

PART II. DISCLOSURE OF INVENTION

Describe the invention fully and completely, using the outline given below. Sketches, prints, photos and other illustrations should be attached to this disclosure. Use additional plain pages as needed to complete the disclosure.

1. **GENERAL PURPOSE.** State in general terms the purpose and objects of the invention.

2. **BACKGROUND.** Describe the old methods, materials or apparatus used to perform the objects of the invention and give their limitations and disadvantages.

3. **DESCRIPTION AND OPERATION.** Describe clearly and completely the construction of the invention and give a detailed description of its operation and use. In the description, use reference characters to refer to components in attached illustrations.

4. **ADVANTAGES AND NEW FEATURES.** State the advantages of the invention over the old methods described in paragraph #2 above, and the features believed to be new.

5. **ALTERNATIVES.** Indicate any alternative methods, materials or constructions of the invention.

6. **CONTRIBUTIONS BY INVENTORS.** If this is a joint invention, indicate what contribution was made by each inventor.

7. **EXECUTION OF DISCLOSURE.** The end of the disclosure should be signed and dated by the inventor(s), - in addition to any signatures in Part I. The disclosure should then be read and understood by two technically qualified witnesses. Under inventor(s) signatures, enter the statement: "Disclosed to and understood by me on (date)." The two witnesses should sign under this statement.

Other individuals to whom invention was disclosed:

S. Kaiser University of Illinois (presently with Hewlett Packard), Sept. 1971-Jan. 1973 (Research Assistant)

A HIGH SPEED SAMPLING PHOTOMULTIPLIER[*]

Henry Merkelo, James J. Wiczer

Quantum Electronics Research Laboratory, University of Illinois,

Urbana, IL, 61801

ABSTRACT

A sampling approach to low-level optical signal detection is reported and the advantages of sampler based instruments for the analysis of complex, high-harmonic content signals are re-examined for optoelectronic considerations. A sampling head, constructed for high speed sampling and processed for an S-4 photosensitivity is described. The sampling head, adapted to an electron multiplier section, is tested for sequential sampling on HeNe, mode-locked laser pulses showing good resolution and signal to noise ratio. The influence of parameter variation on the sampling function is assessed on the basis of photoelectron ballistics; discussion includes optimum and limiting resolutions which extend into the picosecond regime.

The development of photodetectors which are capable of microwave modulation-frequency response and which operate in the visible or near-infrared portion of the optical spectrum has received a considerable amount of attention. The need for detectors in this category, particularly for low-level signal monitoring, exists in both communication and analytical instrumentation areas. However, in spite of the significant progress that has been made, low-level optical phenomena of picosecond (10^{-12} sec) and even tens of picoseconds duration cannot be monitored routinely today as it is possible in some cases in microwave signal processing (1,2). In relation to analytical instrumentation, where not only good signal-to-noise ratio and high bandwidth are required for satisfactory detection, pulse fidelity requirements limit time resolution to several hundred picoseconds if signal deconvolution is to be avoided; the shortcomings of the current detector status are particularly acute in view of the existence of tunable optical excitation sources capable of continuously emitting pulses of picosecond duration, suitable for many studies and applica-

tions. Moreover, high time resolution studies that are currently being carried out at high intensities, by the necessity of indirect detection methods, do not always establish low intensity behavior.

The application of sampling principles have long been used on periodic waveforms to achieve wide bandwidths in oscilloscopes, phase-locked loops, random sampling voltage detectors and other rf systems. Resolution of 10^{-10} sec is routinely achieved and, with thin-film samplers, bandwidths better than 18GHz can be reached (2).

A sampling approach to low-level optical signal processing is reported and the advantages of sampler based instruments for complex, high-frequency signal analysis are re-examined for optoelectronic consideration.

A sampling system generally consists of a broadband sampler, an integrating section, an if-amplifier and, for display purposes, some clock network correlating high speed events to the if representation of the original signal such that the output spectrum, $S_O(\omega)$, is the convolution of the signal spectrum, $S(\omega)$, with the sampling function spectrum, $A(\omega)$, multiplied by the frequency response of the integrator-amplifier block. The low-pass portion of this spectrum is that of a periodic signal similar in spectrum to that of the input signal but with modulation harmonics $n\omega_O = 2\pi n f_O$ substituted for $n\omega = 2\pi n f$ where f_O, f are fundamental frequencies of the output spectrum $S_O(\omega)$ and the original signal $S(\omega)$ respectively. Since spectral components also appear centered about each harmonic of the sampled output, the harmonic sampling extension of the classical sampling theorem requires that $mf_O < f_A/2$ where m is the highest harmonic component in the high-frequency waveform. For example, sequential sampling will take place with high signal fidelity reproduction if the sampling function consists of equal harmonic components and unity efficiency. Then, a signal

$$S(\omega) = \sum_{k=1}^{\infty} (A_k \sin k\omega t + B_k \cos k\omega t)$$

when sampled at a fundamental frequency, f_A, and low-pass filtered, becomes

$$S_o(\omega) = \sum_{k=1}^{\infty} (A_k \sin k\Delta\omega t + B_k \cos k\Delta\omega t)$$

where $\Delta\omega = 2\pi(f_A \pm f)$. If the sampler deviates from the ideal situation of equal harmonic components, the reconstructed component amplitudes will be also modified by the rf frequency response of the sampler. It is interesting to note that the requirement for equal harmonic amplitudes in the sampling function only applies to the terms that exist in the signal, i.e. the first m terms. Any additional components in the sampling function do not serve a useful function.

Adaptation of these fundamental concepts to photoelectric devices requires application of broadband design considerations of components which are, at least partly, assembled and/or processed under vacuum. It is shown, in particular that tolerances significantly affect both the sampling efficiency and the form of the sampling function. In this sense, optoelectronic sampling is analogous in principle to the sampling used in conventional sampling electronic instruments, but implementation of the sampling of photoelectrons is technologically different from electronic sampling.

Given that the sampling process for photoelectrons consists of electrons traversing a drift space of dimension Δx under the influence of a sampling voltage, $V(t)$, the sampling function $A(t)$ is arrived at on the basis of the ballistics for photoelectrons which are distributed in initial velocity according to a function, $g_\lambda(v_o)$, which is dependent on the type of photocathode material and on the wavelength, λ, of the optical signal. A photoelectron is considered sampled if, as a result of the drift space potential, $V(t) - V_r$, where V_r is a constant retarding potential (at least equal to the most energetic photoelectrons), the electron traverses the drift space, Δx. The displacement of photoelectrons is given by

$$x(t) = \frac{q}{m\Delta x} \iint V(t) dt^2 - \frac{qV_r t^2}{2m\Delta x} + v_o t + x_o$$

where q, m are the electronic charge and mass respectively and v_o, x_o are the initial velocity and displacement respectively. Unlike in conventional electronic sampling where the duration of the sampling bridge forward bias and therefore of the sampling function is controlled by the time the strobe pulse exceeds a fixed reverse bias, the sampling voltage on photoelectrons enters nontrivially in

determining the duration of the sampling function, $A(t)$. In fact, due to nonzero initial velocities of photoelectrons, the potential $V(t)$ is affecting the position of electrons well before $V(t) - V_r = 0$. Moreover, the sampling function $A(t)$, bears no resemblance to $V(t)$ since application of $V(t)$ at $t=0$ can effect the transversal of Δx by photoelectrons emitted at $t<0$. The sampling function $A(t)$, the sampling voltage $V(t)$, and the actual waveform of sampled photoelectrons are all shifted in time with respect to each other but retain the enumerated chronological order. For the simple case of $g_\lambda(v_o) = \delta(v_o - v_{oo})$ where δ is the Dirac delta function (i.e. monoenergetic photoelectrons corresponding to initial velocity v_{oo}),

$$A(t) = \begin{array}{l} 0 \text{ if } x_t(t') < \Delta x \text{ for all } t' \\ A \text{ if } x_t(t') \geq \Delta x \text{ for some } t' \end{array}$$

where $x_t(t')$ designates displacement of those photoelectrons which are emitted from the photocathode at time t; note that it is irrelevant at what time, t', the electron traverses the drift space Δx. That is, if $V(t)$ is sufficiently large to effect displacements such that $x_t(t') \geq \Delta x$ for some t' and $V(t)$ is monotonically increasing and then monotonically decreasing, then $A(t)$ is a square pulse; the width, τ, of $A(t)$ is, however, a function of the form of $V(t)$. When the initial velocities of photoelectrons obey a relatively narrow distribution function, $A(t)$ will be still flat-topped but with rounded corners.

Extensive analysis aimed at determining the sampling function, $A(t)$, and the sampling efficiency for various geometrical configurations and velocity distributions, $g_\lambda(v_o)$, show that a practical optoelectronic sampling device effecting a sampling time $\tau \approx 80$psec can be routinely achieved. For illustration, adapting a specially designed sampling head on a conventional electron multiplier cage (RCA 7102), HeNe, mode-locked laser pulses were monitored in the optoelectronic sequential sampling mode and displayed on an ordinary (real time) oscilloscope as shown on the photograph of Figure 1 (equivalent horizontal scale: 200 psec/div). For a square wave sampling function, $A(t)$, the magnitudes of the harmonics of order k are proportional to

$$(\sin\frac{k\omega\tau}{2})/\frac{k\omega\tau}{2}$$

Typical HeNe, mode-locked laser pulses consist of only approximately 15 harmonics and since the value of the amplitude of the fifteenth term of the sampling function drops to only 0.987 of the amplitude of the fundamental, it is consistent that good sampled waveforms exhibiting the

expected symmetry observed. Since only the sampling head is subjected to the input signal and sampling high-frequencies and all the amplification takes place at relatively low-frequencies, the performance of the sampling system is not dependent on the gain-bandwidth limitation of conventional amplifiers. The signal-to-noise ratio is significantly better than in any fast photomultiplier/sampling oscilloscope combination and ample gain is available for detecting low-level radiation.

Unlike many photoelectric gated devices, which operate at high voltages, low-level signal design suitable for broadband and high sampling rate operation was stressed in this development. The resulting disadvantage is that the system is sensitive to initial velocity distribution, $g_\lambda(v_o)$, of photoelectrons and therefore, the sampling function, $A(t)$, is wavelength dependent. For many photocathode materials, best resolution will be obtained on the red end of the spectrum. The choice of cesium antimonide photocathode and 6328 Å operation, although fortuitous here, is particularly suitable for obtaining good resolution. In spite of the dispersion effects introduced by initial photoelectron velocities, extensive computations show that with high precision design and select use of thin and thick film technologies, a sampling width, τ, of less than 10psec can be realized with currently available methods.

Finally, the possibility of large area photocathodes in high speed optoelectronic sampling devices has also been explored with indication that significant improvements, with respect to any other known designs suitable for high speed application, are realizable. Again, this bears on the fact that arrival of photoelectrons to the first dynode is already part of the slow structure operation and, therefore, does not require stringent timing considerations.
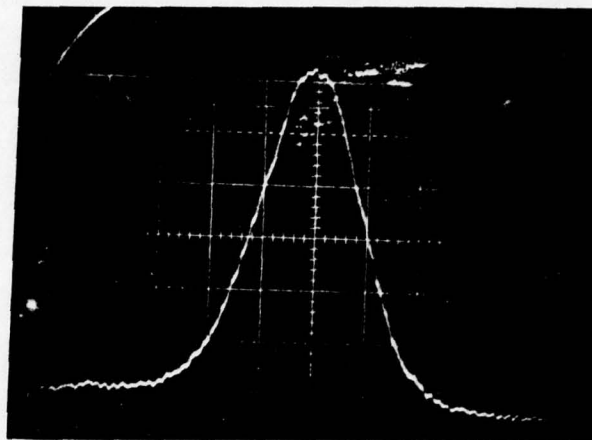

Figure 1. Optoelectronically sampled laser pulses displayed on an ordinary oscilloscope. Horizontal equivalent scale: 200 psec/div.

[1] W. M. Grove, IEEE Transactions on Microwave Theory and Techniques, MTT-14, 629 (1966).

[2] J. Merkelo, R. D. Hall, IEEE Journal of Solid-State Circuits, Special Issue on Microwave Integrated Circuits, (1971).

OPTOELECTRONIC SAMPLING—I.   PARAMETERS FOR PICOSECOND RESOLUTION

Henry Merkelo, James J. Wiczer, and Paul R. Buttinger

Quantum Electronics Research Laboratory

University of Illinois, Urbana, Illinois   61801

ABSTRACT

Sampling of photoelectrons by rapidly varying electric fields is for-
mulated for configurations suitable for high-speed detection of optical
signals. The dynamics of photoelectrons near the surface of the emitter is
taken into account in the modeling and the numerical analysis designed to
characterize the sampling process. The influence of delays in the photoelec-
tric emission on the resolution and efficiency of optoelectronic sampling
is given particular attention. It is shown that such sampling can form the
basis for high-gain detectors capable of picosecond resolution of optical
signals. Sequential sampling is especially adaptable to studies involving
the periodic emission of continuously operated, mode-locked lasers.
Quantum efficiencies being comparable to those existing in conventional
photodetectors, the sampling approach is suitable for detection at low
signal levels; in the limit, picosecond resolution counting of photons
should be possible. Moreover, it is demonstrated that high resolution
optoelectronic sampling is effective at low sampling voltages and, there-
fore, can be made compatible with conventional electronic signal processing
instruments for applications in low light-level picosecond spectroscopy
and optical pulse dispersion studies.

I. INTRODUCTION

Optical studies requiring picosecond resolution have taken a new direction with the advent of broadband, mode-locked lasers. The new methods for generating, controlling, and monitoring picosecond optical events have led to significant results in photophysics, photochemistry, photobiology, and optical communication studies and applications.[1] Currently, however, the techniques for generating, amplifying, frequency doubling, isolating and chirping picosecond optical pulses are far more advanced than the methods used for accurately and conveniently monitoring such processes. Whereas a wide variety of sources exists for generating ultrashort pulses of various durations and of adjustable intervals, detection methods suitable for picosecond resolution of optical events are not yet sufficiently routine for widespread usage. In particular, difficulties arise at low signal levels and with incoherent radiation when frequency doubling or multiphoton interactions are ineffective.

The development of photodetectors that are capable of microwave bandwidth modulation response and that operate in the visible or near infrared portion of the optical spectrum has received considerable attention as evident, for example, from the extensive bibliography documenting the review written by Anderson and McMurtry.[2] It is recognized that the need for detectors in this category, particularly for low-level signal monitoring, exists in both communication and analytical instrumentation areas. However, in spite of the significant progress that has been made, some low-level optical phenomena of picosecond and even tens of picoseconds

duration cannot be recorded today with adequate time resolution. In relation to analytical instrumentation, where not only good signal-to-noise ratio and large bandwidth are required for satisfactory detection of low signal levels, pulse fidelity requirements limit time resolution of optical waveforms to several hundred picoseconds if signal deconvolution is to be avoided. The shortcomings of the current detector status are particularly acute in view of the existence of tunable optical excitation sources, capable of continuously emitting pulses of picosecond duration, suitable for many studies and applications. Moreover, some high-time resolution studies that are currently being carried out at high intensities do not always determine low intensity parameters. This is particularly the case with luminescence in semiconductors and biological, optically active materials. For instance, saturation occurs at modest illumination levels (< 1 mW cm^{-2}) in biological systems of the important, photosynthetic group[3] in which the dynamics of fluorescence has picosecond characteristics. Other than indirect methods[4], means do not exist for studying picosecond dynamics of reactions taking place in these materials at illumination intensities below the luminescence saturation limit[3].

The aim of this study is to examine the basic characteristics of photo-detectors in a new configuration suitable for high-time resolution and adaptable—in sampling operating modes—to high-gain multipliers and signal averaging instruments. Motivation for this work was provided by the successful preliminary testing of the basic optoelectronic sampling configuration which was previously reported[5,6]; the operation of the sampling prototype was compared to the performance of the most developed, high-speed, commercial phototube suitable for low-level signal detection, which at that time was the Sylvania #502 Static Crossed Field Photomultiplier rated at beyond 3.0

2

GHz bandwidth. Even without the application of thin- and thick-film technologies in the construction of the prototype, the advantages of optoelectronic sampling were demonstrated on both signal quality and signal fidelity. Since electric ringing in the waveform trailing edge is frequently encountered in high-speed photodetectors--rendering signal comparison or deconvolution analysis unreliable--signal fidelity will be an important consideration in this text.

It is well known that the evolution of sampling principles enabled significant advances to take place in the design of wide-band oscilloscopes, phase-locked loops, random sampling voltage detectors and other microwave systems suitable for periodic waveform analysis. Resolution of a hundred picoseconds is routinely achieved in conventional electronic devices designed for sampling mode operation[7]; with thin-film samplers, bandwidths better than 20 GHz have been attained[8]. Sampling methods sidestep both the gain-bandwidth and display-size limitations of auxiliary devices by translating the input signal to a much lower frequency domain where conventional methods for amplifying, recording or displaying are more effective. For these reasons, a high-speed sampling approach to low-level, optical signal monitoring has been devised and the advantages of sampler based instruments for complex, high-frequency signal analysis are evaluated in optoelectronic applications. Although only coherent, sequential sampling of periodic waveforms will be formally treated here, many other aspects of signal processing by sampling methods will remain within the context of this paper.

II. HIGH-SPEED OPTOELECTRONIC SAMPLING

Generally, a sampling system consists of a broadband sampler, an integrating section which stretches the samples into a continuous signal, an intermediate frequency (IF) amplifier which provides signal gain, and some clock network correlating high-speed events to the IF simulation of the original signal[7]. Thus, a sampling system can be viewed as a series of separate processes, in which the final output can be determined by bandwidth considerations. Photoelectric devices, being current sources, illustrate particularly well the direct dependence of signal level on load resistance and the inverse relationship between signal amplitude and bandwidth. For these reasons, the advantages of down-converting operating frequencies afforded by sampling are immediately apparent.

The family of optoelectronic devices related to this study includes sampling photomultipliers, sampling photon counters, adapting sampling heads, array detectors, as well as demultiplexing and decoding samplers, all suitable for high-speed operation. In this text, the analysis will be limited only to the basic sampling configuration which is common to all designs. The sampling geometry consists of an electrically broadband, vacuum-spaced,* suspended microstrip[9] in which photoelectrons are sampled by rapidly varying accelerating electric fields created by ultrashort electrical sampling pulses. These pulses, which are generated in thin-film, ultrabroadband circuits, propagate along the photoemissive thin-film microstrip line. The coordinates necessary for the analysis of optoelectronic sampling

---

*For achieving higher tolerances, the vacuum-spaced configuration can be replaced with a microchanneled design. Precision fabrication of photoelectrically active, microstrip samplers, which involves both thin- and thick-film technologies, will be described elsewhere.

123

are indicated in Figure 1. Photoelectrons created at the emitter E are swept through the drift space D of dimension Δx. The surface and near-surface kinetics of these charges which are influenced by the energies of quantum origin and by forces induced by propagating electric fields, significantly affect the resolution and the efficiency of sampling. For these reasons, the analysis of high-speed optoelectronic sampling takes into account the following considerations:

1) Electrons originating at the emitter E are accelerated in the drift space D by rapidly varying, electric fields $E(t,z)$ of the form $[v(t,z) - V_r]/\Delta x$ where V_r is the retarding potential which is transiently counteracted by the propagating potential $v(t,z)$ traveling along the z-direction with time dependence t. Although constituting moderate potentials these fields are allowed to exceed rates of change $\frac{\partial E(t,z)}{\partial t}$ of 500 V cm^{-1} psec$^{.}$ An example of such rapidly varying potentials $v(t,z_o)$ (where z_o is an arbitrary point), generated for optoelectronic sampling, is illustrated in Figure 2. These waveforms are represented quite well by the following relations:

$$v(t,z_o) = \begin{cases} 0 & \text{for } t < 0 \\ V_o \sin^2(\frac{\pi}{\Gamma}t) & \text{for } 0 \leq t \leq \Gamma \\ 0 & \text{for } t > \Gamma \end{cases} \qquad (1)$$

where V_o and Γ are convenient parameters for numerical analysis. Superimposed on the oscilloscope trace of Figure 2, the dotted line is a graph of (1) for V_o = 14.2 V and Γ = 68 psec. The generation of such broadband signals is essential for realizing effective high-speed sampling. However, we will show on the basis of the properties of surface emission of photoelectrons that the characterization of the actual optoelectronic sampling function is more informative than a detailed discussion of the fields responsible for the sampling. since, for example, the waveform of Figure 2 can give values for sampling resolution ranging from a hundred to a few picoseconds depending on the choice of other parameters.

5

2) The displacement x of photoelectrons in the drift space depends
on their x-directed, initial velocities v_x. Corresponding to each wavelength
λ of the incident radiation, the photoelectrons emitted by each material will
be distributed in velocity, at x = 0, according to a function designated as
$g_\lambda(v_x)$. Experimentally determined velocity distributions will be used in
specific numerical examples.

3) Whereas a reasonable amount of experimental data exists on $g_\lambda(v_x)$,
the time of emission γ of photoelectrons, which establishes the response time
of the emitter, remains sparsely documented. Without even taking into account
the long standing problem of the time dependence of the probability of photo-
electric emission on time scales on which the oscillations of the optical
field are resolved, as considered for example by Mandel and Meltzer[10], the
response time of a finite thickness photoactive surface can be significantly
affected by lattice scattering, pair production, formation and destruction of
exciton and impurity states, and free carrier lifetimes. For instance, by
assuming that lattice scattering determines the escape depth in all useful
photoemitters in which the threshold for pair production is large compared
with the electron affinity, it is possible to construct arguments which give
an upper range for response time such that 1 < γ < 10 psec for surface thick-
nesses on the order of 500Å. Photoemitting layers substantially thinner
than average escape depth will be characterized by smaller γ's. For opto-
electronic sampling considerations, it is important to know more than just
an average response time. In particular, since ejection velocities are
taken into account in detail, ideally, the time evolution of photoelectric
emission should be established for each velocity. The time evolution of
emission should be principally controlled by the escape mechanism and the
interactions concomitant with escape. On that basis, it can be concluded
from the observations of Methfessel[11] that the low energy tail of $g_\lambda(v_x)$

125

6

will have a greater time of emission dispersion than the high energy group
and that this dispersion will be smaller for a front-illuminated than for
a back-illuminated (semitransparent) photocathode. At present, only an
upper limit of approximately 30 psec can be deduced for γ from the existing
literature[12].

4) Photoelectric emission is enhanced by electric fields in the kV cm^{-1}
range[13,14]; of course, only static measurements exist. Similar quantum
efficiency improvements are expected with rapidly propagating fields and,
moreover, both $g_\lambda(\nu_x)$ and γ are expected to be altered by sampling fields
which, for the cases considered, may be as high as 3kV cm^{-1}. It is expected
that both resolution and sampling efficiency would be favorably affected
by such field enhancement but, due to the lack of data, this consideration
will not be taken into account quantitatively at this time.

The waveforms shown in Figure 3 are useful in discussing optoelectronic
sampling. Only sequential sampling is considered in this analysis. The
intensity envelope of optical radiation (incident on the detector) which is
illustrated in Figure 3A, is represented by a periodic waveform $f_1(t)$ of
period T. Electrons injected into the drift space are under the influence
of fields $E(t,z)$, of period $T + \Delta t$, created by propagating potentials
$[v(t,z) - V_r]$. The sampling function $f_s(t)$, which effects sampling of the
form $f_1(t)f_s(t)$, is constructed on the basis of the effectiveness of the
fields $E(t,z)$ to extract electrons from the drift space as a function of
time; i.e., a photoelectron emitted as a result of a photon interaction at
some time t is considered to have been sampled if it has completely
traversed the dimension Δx of the drift space within one period. Note
that the time reference is that of the photon striking the emitter and not
the potentially delayed time $t + \gamma$, nor is it the time at which the dis-
placement Δx is completed. In fact, unlike in a conventional high-speed

photodiode, the time $t_{\Delta x}$ at which $x = \Delta x$ is entirely irrelevant as long as $t_{\Delta x} - t < T$. The duration of any one pulse of $f_s(t)$ -- full width at half maximum -- is designated by τ and is shown in Figure 3C. It is determined by establishing the duration of sampling effected by $E(t,z)$ at a single point z_0. This type of stationary analysis is valid for any photoactive length, Δz, such that $\Delta z \ll \tau c$ where c is the propagation velocity of $E(t,z)$. For all such cases, voltages and fields are simply designated by $v(t)$, as in Figure 3B, and $E(t)$, respectively. The effect of progressively delaying each sample by an increment Δt with respect to the relative position of the preceding sample on $f_i(t)$ results in a replication of the original signal $f_i(t)$ by $f_o(t)$ such that $f_o(t') = G f_i(t)$ where G is a constant and $t' = \frac{T}{\Delta t} t$ is a scaling transformation illustrated in Figure 3D. Although over-simplified, this conceptualization asserts that bandwidth requirements for auxiliary subsystems (apart from the principal sampler) are reduced by a factor of $\frac{\Delta t}{T}$ where, generally, $\Delta t \ll T$.

It is important to note that the instantaneous sampling is of the form $f_i(t) f_s(t)$ but that, prior to amplification and low pass filtering, the amplitude contribution to $f_o(t)$, corresponding to any period n is given by

$$\int_{(n-1)T}^{nT} f_i(t) \, f_s(t) \, dt \quad . \tag{2}$$

The intuitive understanding is further enhanced in the limiting case for which every period n of $f_s(t)$ is a Dirac delta function $\delta(t - t_n)$. Sampling could be considered perfect since (2) becomes

$$\int_{(n-1)T}^{nT} f_i(t) \, \delta(t - t_n) \, dt = f_i(t_n) \quad . \tag{3}$$

Clearly, the requirement that $f_i(t)$ be a slowly varying function during the time $t_n - \frac{\tau}{2} < t < t_n + \frac{\tau}{2}$, where τ again designates the duration of any one pulse

8

of $f_s(t)$, will be an important consideration. Accurately characterizing $f_s(t)$ and, therefore, establishing τ and the efficiency of sampling for various para-meters is clearly the key factor to be considered in appraising the effective-ness of optoelectronic sampling. The procedure for obtaining $f_s(t)$ involves solving the photoelectron displacement equation, which is of the form

$$x(t,\alpha) = \frac{q}{m\Delta x} \int_o^\alpha d\alpha' \int_o^{\alpha'} v(\alpha'') \, d\alpha'' - \frac{qV_r\alpha^2}{2m\Delta x} + v_x\alpha \qquad (4)$$

where q and m are the electronic charge and mass, respectively; t is the time of light interaction at the emitter; α is a time reference such that the origin of α corresponds to the light interaction time t (i.e., $x(t,\alpha) = 0$ for $\alpha = 0$); and, α' and α'' are simply variables of integration. If complete traversal of the drift space is effected then $x(t,\alpha) = \Delta x$ for $\alpha = \alpha_{\Delta x}$. This takes place at time $t_{\Delta x} = t + \alpha_{\Delta x}$. For optoelectronic sampling, it is only necessary to establish whether or not $t_{\Delta x}$ exists, and the duration of time τ for which it exists, for any given $v(t) - V_r$, $g_\lambda(v_x)$ and Δx. For the potential differences allowed here, τ is significantly smaller than $\alpha_{\Delta x}$ -- wherein lies another advantage of optoelectronic sampling for high-speed detection.

The fidelity with which the sampling process replicates $f_i(t)$ can be analyzed on the basis of bandwidth and phase relationship requirements. For simplicity, we continue assuming that the requirement for correlating the high-speed input signal with the IF representation of the signal is implicitly included in a sequential sampling mode of operation. The sampling process can be stated as the product of two Fourier series; one series representing the optoelectronic sampling function $f_s(t)$, and the other representing the periodic intensity of the input optical signal $f_i(t)$. Thus, in general,

$$f_i(t) = \sum_{k=0}^{K} a_k \cos(k\omega_i t + \phi_k) \qquad (5)$$

9

where, for a band-limited signal, K is finite. Similarly, the sampling function $f_s(t)$ can be written as

$$f_s(t) = \sum_{m=0}^{M} b_m \cos(m\omega_s t + \psi) \quad . \quad (6)$$

The output signal $f_o(t)$ can be represented as the product of the sampling function $f_s(t)$ and the incident signal $f_i(t)$. The resulting product can be simplified greatly by considering the amplifier as a low pass filter which rejects high frequency components such as ω_i and ω_s as well as their harmonics, passing only those terms containing the difference $\omega_i - \omega_s$:

$$f_o(t) = C \sum_{n=0}^{N} a_n b_n \cos[n(\omega_i - \omega_s)t + \theta_n] \quad (7)$$

where $\theta_n = \phi_n - \psi$, C is a constant, N is equal to K or M, whichever is smaller. Then, choosing $f_s(t)$ such that $M \geq K$ and, therefore, $N = K$ and requiring that $b_j = b_o$ for all $j \leq K$, we see that $f_o(t)$ fully replicates $f_i(t)$ at a greatly reduced frequency (for $\Delta t << T$) with a new amplitude and phase reference:

$$f_o(t) = Cb_o \sum_{n=0}^{K} a_n \cos[n(\omega_i - \omega_s)t + \theta_n] = Cb_o f_i(\frac{\Delta t}{T} t) \quad . \quad (8)$$

It is interesting to note that the requirement for equal harmonic amplitudes, $b_j = b_o$, applies only to the terms that correspond to the terms that exist in the incident signal. Any additional components in the sampling function, such as $b_j \neq 0$ for $j > K$, do not serve any useful purpose. Therefore, the ideal sampling waveform corresponds, in the frequency domain, to a flat-topped comb function, band-limited at $K\omega_s/2\pi$ Hz; the phases of its harmonics are equal to ψ as in (6). This insures not only absolute signal fidelity but also minimum

sampling power requirements. The importance of accurately characterizing $f_s(t)$ for picosecond resolution at maximum efficiency is evident from these conclusions.

III. CHARACTERIZATION OF THE SAMPLING FUNCTION

Whereas in conventional electronic sampling the width of the sampling function is determined simply by the interval during which the sampling bridge is forward biased by a "strobe" pulse, in optoelectronic sampling the sampling pulse $v(t)$ and other parameters affect the value of τ nontrivially. In fact, due to nonzero initial velocities of photoelectrons, the potential $v(t)$ can affect the position of electrons that are emitted well before $v(t) - V_r \geq 0$. Moreover, the sampling function $f_s(t)$ does not always resemble $v(t)$, since even if $v(t) = 0$ for $t < 0$ it can effect complete traversal of Δx by photoelectrons emitted at $t < 0$. The sampling function $f_s(t)$, the sampling voltage $v(t)$, and the actual waveform of current flowing at $x = \Delta x$ are all shifted chronologically with respect to each other in the above order. Again, a limiting case can serve as a convenient illustration. For the special case of $\gamma = 0$ and $g_\lambda(v_x) = \delta_\lambda(v_x - v_{xo})$, where δ is the Dirac delta function (i.e., monoenergetic photoelectrons corresponding to initial velocity v_{xo}), we find that, regardless of the exact waveform of $v(t)$,

$$f_s(t) = \begin{cases} 0 \text{ if } x(t,\alpha) < \Delta x \text{ for all } \alpha \\ S_o \text{ if } x(t,\alpha) \geq \Delta x \text{ for some } \alpha < T \end{cases} \qquad . \qquad (9)$$

That is, if $v(t)$ is sufficiently large to effect displacements such that $x(t,\alpha) \geq \Delta x$ for some α and if $v(t)$ monotonically increases to a peak V_o which is followed by a monotonic decrease then, remarkably, $f_s(t)$ is a rectangular waveform! The width τ of $f_s(t)$, but not the amplitude S_o, is a function of the form of $v(t)$. When the initial velocities of photoelectrons obey a relatively narrow distribution function, which is generally true near

11

the photoelectric threshold, $f_s(t)$ is still flat-topped but with rounded corners.

For the exact determination of $f_s(t)$—both its waveform and amplitude—specific values of parameters are chosen and included in a numerical analysis prepared on the basis of the considerations developed earlier.

It should be recognized that, since the displacement law is an integral equation, the quantitative characterization of $f_s(t)$ can be given only for specific cases. A computer analysis was formulated such that all important variables could be suitably incorporated. The obvious parameters to be scanned over chosen ranges of values are the drift space dimension Δx, the retarding potential V_r, and the coefficients specifying the accelerating potential $v(t)$. Moreover, for each optical wavelength, each time reference must be incremented over the range of initial velocities given by $g_\lambda(v_x)$.

Choosing the cesium-antimony photocathode as an example, parameter ranges commensurate with picosecond resolution and corresponding to driving waveforms described by (1) were determined. Standard assumptions were made with regard to spatial uniformity of fields and negligible space charge effects. Only the trends that best illustrate the concepts of optoelectronic sampling and the manifestation of parameter values are included in this text. Figure 4 shows a typical result, demonstrating the time relationship between $v(t)$ and $f_s(t)$ for two values of V_r; for this example, the parameter values are: $V_o = 14.2V$, $\Delta x = 10\mu m$, $\lambda = 6200\overset{o}{A}$, $\gamma = 0$ and $\Gamma = 68$ psec; values for $g_\lambda(v_x)$ were taken from Khlebnikov and Melamid[15]. It should be noted that the electronic waveforms illustrated in Figs. 2 and 4 could be instrument limited since the best commercial electronic sampling components are designed for 20 psec rise time which is accompanied by several picoseconds of jitter in display; when specially tuned, the performance can be somewhat better. Both rise time and fall time (10% to 90%) of the pulse shown in Figure 2 are

close to the standard ratings of the instruments. Other than complete spectral analysis, which requires accurate phase measurements of all harmonics, no other standards were available to settle the issue. If waveforms $v(t)$ could not be represented analytically by the form of (1), the time-resolution results for optoelectronic sampling established in this work would represent only conservative estimates vis-à-vis the values corresponding to a $v(t)$ with a higher time rate of change than that of $\sin^2 \frac{2\pi}{T} t$.

The example of $f_s(t)$ corresponding to $V_r = 12.3V$, illustrated in Figure 4, is shown to approach a peak value S_o which is the theoretical maximum corresponding to the extraction of all photoelectrons created by $f_i(t)$. Frequently, in real devices, as in the above example but unlike in the example expressed by (9), $f_s(t)$ will not reach the peak value S_o. In general, $f_s(t)$ is not a rectangular waveform and, in addition, for any given $v(t)$, its shape changes with V_r, Δx, γ, and $g_\lambda(v_x)$. For these reasons, two quality parameters, η_E and η_F, designating sampling efficiency and sampling fidelity, respectively, were defined and computed on the basis of the following relations:

$$\eta_E = \frac{1}{S_o \tau} \int_{t_o}^{t_o + \tau} f_s(t)\, dt \tag{10}$$

$$\eta_F = \frac{\displaystyle\int_{t_o}^{t_o + \tau} f_s(t)\, dt}{\displaystyle\int_{(n-1)T}^{nT} f_s(t)\, dt} \tag{11}$$

where, as illustrated in Figure 5, S_o is the theoretical maximum of $f_s(t)$; S, the actual maximum of $f_s(t)$; and, t_o and τ are such that $f_s(t_o) = f_s(t_o + \tau) = \frac{S}{2}$.

13

132

Clearly, the sampling efficiency parameter η_E quantifies the effectiveness of the sampling fields in extracting (from the drift space) photoelectrons created within the time interval τ. Thus, η_E relates to signal strength. As stated earlier, the need for defining the sampling fidelity parameter η_F arises from the fact that, for any given sampling waveform $v(t)$, the analytical form of $f_s(t)$ changes for different parameters. For this reason, the characterization of $f_s(t)$ by τ only is inadequate, particularly when $v(t)-V_r$ is small. It is noted that if $g_\lambda(\nu_x) = \delta_\lambda(\nu_x - \nu_{xo})$, both η_E and η_F would be unity and characterization of $f_s(t)$ by τ would suffice. It can be said also that the proximity of η_F to unity is a measure of the squareness of $f_s(t)$ and, therefore, the applicability of the familiar line spectrum relationship $\sin\chi/\chi, \chi = n\omega_s\tau/2$, to the estimation of the fidelity of the rendition of $f_i(t)$ by $f_o(t)$, (i.e., for the verification of the condition $b_j \simeq b_o$, $j \leq K$).

Retaining the same values for V_o and Γ as before and continuing to keep $\gamma = 0$, the effect of changing the drift space dimension is shown in Figures 6 and 7 for two portions of the visible spectrum: $\lambda = 6200\text{\AA}$ and $\lambda = 4047\text{\AA}$, respectively. Although both η_E and η_F were computed, for clarity, only η_E is shown; η_F was determined to remain always greater than 0.75. Typically, the sampling efficiency η_E drops off well before the sampling fidelity η_F indicating that, under conditions of marginal signal level, resolution may be limited to approximately 5 psec in the red and 10 psec in the violet. (τ decreases monotonically with increasing wavelength for cesium-antimony photocathodes.) However, under conditions of ample signal level, picosecond resolution sampling, exhibiting good fidelity, is attainable. Figures 6 and 7 are also useful for showing that, given any desired τ, no optimum drift space dimension exists. Electron extraction efficiency monotonically increases with decreasing Δx. A sample curve, labeled 7 psec in the space corresponding to η_E values, has been constructed in Figure 6, indicating the at $\lambda = 6200\text{ \AA}$ nearly 70% extraction is possible

14

for 7 psec resolution. For τ = 4.5 psec, η_E is still ~ 0.30 for $\Delta x = 10$ μm. Finally, the effect of varying Γ is shown in Figure 8. As should be expected, it is confirmed that, corresponding to any given efficiency $\eta_E < 1.0$, τ increases with Γ and the minimum τ is attainable with minimum Γ when V_o is kept constant.

The effect of a finite delay in photoelectric emission, also referred to as photocathode response time γ, can be significant in optoelectronic sampling under certain conditions. Analytically, a delay between the time the emitting surface is illuminated and the time electrons are ejected from the surface is equivalent to a coordinate translation such that the displacement process described by (4) is not initiated until $\alpha = \gamma$. Letting $\beta = \alpha - \gamma$, $d\beta = d\alpha$, we can continue describing the displacement of electrons with (4) if β is substituted for α everywhere. Again, because it is not important when $t_{\Delta x}$ occurs, if it occurs, (other than $t_{\Delta x} - t < T$ as before) an equal delay on all photoelectrons at any given wavelength has neither an effect on resolution nor on any other parameter previously computed, unless the detector is simultaneously monitoring signals at several wavelengths. However, even for the monochromatic case, the more general condition will be that corresponding to each velocity v_x there will be a different emission delay and, moreover, that these delays will be described by distribution functions in time. Letting γ designate a time variable with origin at t of $f_i(t)$, we write the said distribution function as $G_\lambda(v_x, \gamma)$ such that

$$g_\lambda(v_x) = \int G_\lambda(v_x, \gamma) \, d\gamma \quad . \tag{12}$$

Then, for any given t, the contribution to $f_s(t)$ is expressed as

$$\int \int U_1 U_2 G_\lambda(v_x, \gamma) \, d\gamma \, dv_x \tag{13}$$

15

where $U_1 = U_1(\gamma - \gamma_1)$ and $U_2 = U_2(\gamma_2 - \gamma)$ are unit step functions such that $\gamma_2 \geq \gamma_1$ and

$$U_1 = \begin{array}{l} 0 \text{ for } \gamma < \gamma_1 \\ 1 \text{ for } \gamma \geq \gamma_1 \end{array}$$

$$U_2 = \begin{array}{l} 0 \text{ for } \gamma > \gamma_2 \\ 1 \text{ for } \gamma \leq \gamma_2 \end{array} \qquad (14)$$

The values for γ_1 and γ_2 are found by establishing the range of delays, $\gamma_1 \leq \gamma \leq \gamma_2$, for which $t_{\Delta x}$ exist. Equation (13) is integrated over the ranges $\gamma_1 \leq \gamma \leq \gamma_2$ and $0 \leq \nu_x \leq \nu_{x,max}$ where $\nu_{x,max}$ is the maximum velocity in $g_\lambda(\nu_x)$. Equation (4) is solved for each velocity. The solution requires the use of the coordinate translations $\beta = \alpha - \gamma$, analogous to the translation corresponding to the simple case of a single, non-zero delay γ. Thus, in the general case of emission, the analytical treatment in the evaluation of the displacement of photoelectrons for each given ν_x and γ can be reduced to the simple case of a single, non-zero delay. And, although it was noted that a single delay on all ν_x did not influence any sampling parameters, the influence of emission delays described by $G_\lambda(\nu_x, \gamma)$ will be generally manifested on the sampling function $f_s(t)$ by virtue of (13). For example, the following general observation can be made. When the high energy side of $g_\lambda(\nu_x)$ is delayed with respect to the low energy portion, the lagging edge of $f_s(t)$ becomes more abrupt and the leading edge rises more progressively than for $\gamma = 0$; the converse is true when low energy photoelectrons are delayed with respect to those described by the high energy portion of $g_\lambda(\nu_x)$--which is the expected behavior for real materials. For illustration and for an appraisal of the magnitude of the influence of delayed emission on the sampling

16

parameters, the following description of photoemission was considered. Let

$$G_\lambda(\nu_x, \gamma) = g_\lambda(\nu_x) \, \delta[\gamma - \gamma(\nu_x)] \tag{15}$$

and

$$\gamma(\nu_x) = \gamma_0 \left(1 - \frac{\nu_x}{\nu_{x,max}}\right) \quad . \tag{16}$$

The delay in emission corresponding to $\nu_x = 0$ is γ_0 and, as before, the maximum velocity in $g_\lambda(\nu_x)$ is $\nu_{x,max}$. Although simple in form, this representation of emission describes a real material better than a single average delay by specifying an average delay, $\gamma(\nu_x)$, for each velocity ν_x. The effect of emission delays on the characteristics of $f_s(t)$ for this case was investigated on the basis of (13)-(16) by solving (4) in accordance with the coordinate translations $\beta(\nu_x) = \alpha - \gamma(\nu_x)$. Figure 9 summarizes the results of the study corresponding to $v(t)$ of (1), $g_\lambda(\nu_x)$ of cesium-antimony, and the following parameters: $0 < \gamma_0 < 54$ psec, $\Gamma = 68$ psec, $V_0 = 14.2$ V, $\Delta x = 10$ μm, and $\lambda = 6200\text{Å}$. For this form of $G_\lambda(\nu_x, \gamma)$, even small values of emission delays markedly affect the efficiency of sampling without significantly altering resolution. This suggests that the sampling function broadens at the base without commensurately increasing at half-amplitude. The value of the integral corresponding to the denominator of (11) retains approximately the same value. At higher values of γ_0, both the base of $f_s(t)$ and τ increase but still disproportionately as evidenced, for example, by only a 10% increase in τ for a 50% loss in η_E when γ_0 is as large as 54 psec. In addition to changes in η_E and τ, emission delays also affect the waveform of $f_s(t)$. Of course, only complete frequency spectra of $f_s(t)$ with detailed phase information corresponding to (6) would determine accurately the effect of waveform change on sampling resolution.

17

136

IV. CONCLUSIONS

The formalism required for the analysis of optoelectronic sampling is fully developed on the basis of the dynamics of electrons produced as a result of photoelectric interaction. It is shown that the sampling of such electrons at the photocathode surface can be effected with high efficiency within time intervals as short as a few picoseconds provided certain conditions are satisfied. For maximum time resolution at maximum sampling efficiency, the general guidelines deduced from the analysis of optoelectronic sampling indicate the need for ultrashort sampling voltage waveforms, small dimensions, thin photocathodes—preferably designed for front-illumination, and operation at wavelengths near the photoelectric threshold. Of course, only special geometries, such as microstrip configurations, are compatible with the propagation of such ultrashort voltage waveforms. These qualitative observations are supported by numerical examples which illustrate the potential performance of optoelectronic samplers both under ideal conditions and under limitations existing with real materials. In particular, characteristics describing optoelectronic sampling are fully specified for some select dimensions, material parameters, and driving waveforms. Sampling widths of a few picoseconds are obtained for several combinations of parameter values. Given that sufficient intensity exists to overcome considerable losses in sampling efficiency, single picosecond structures of optical signals can be resolved provided geometrical constraints are observed. It should be noted that small fractions of a millimeter in path length difference are important in picosecond detection, both when considering the extent of the optical source and the extent of the photocathode.

The possibility of implementing relatively large area photocathodes in high-speed optoelectronic sampling devices is only implicitly included

<u>137</u>

in this text with the statement of the condition $\Delta z \ll \tau c$. For example, whereas a commercial high-speed crossed field photodetector is limited in photocathode area to 4 mm^2 and in risetime to $\sim$ 150 psec[16], a detector equivalent in speed but designed on the optoelectronic sampling principle could have a photoactive area ten times that value. Geometrical comparisons are not possible for detectors suitable for picosecond resolution since no fully electronic devices exist to the best knowledge of the authors. However, it is clear that even for 10 psec resolution, geometrical considerations will play an important role.

Finally, it is important to emphasize that the dynamics of photoelectric emission is inadequately documented at present for the purpose of accurate optoelectronic sampling design. A complete specification of emission parameters, expressed here by $G_\lambda(\upsilon_x, \gamma)$, is required for each material for a complete quantitative analysis of the sampling of photoelectrons.

REFERENCES

1. I. Prigogine and S. A. Rice, ed., _Advances in Chemical Physics_. New York: Wiley & Sons, 1973, pp. 189-225.

2. L. K. Anderson and B. J. McMurtry, "High-Speed Photodectectors," _Proc. IEEE_, vol. 54, pp. 1335-1349, October 1966.

3. A. Müller, R. Lumry and M. S. Walker, "Light-Intensity Dependence of the In Vivo Fluorescence Lifetime of Chlorophyll," _Photochemistry and Photobiology_, vol. 9, pp. 113-126, 1969.

4. H. Merkelo, J. H. Hammond, S. R. Hartman and Z. I. Derzko, "Measurement of the Temperature Dependence of Depolarization Time of Luminescence," _J. Luminescence_, vol. 1,2, pp. 502-512, 1970.

5. H. Merkelo and J. J. Wiczer, "A High-Speed Sampling Photomultiplier," Technical Digest, _1973 International Electron Devices Meeting_, Washington, D.C., pp. 217-219, December 1973.

6. H. Merkelo, S. V. Kaiser and J. Merkelo, "High-Speed Optoelectronic Sampling," _Appl. Phys. Lett._, to be published.

7. W. M. Grove, "Sampling for Oscilloscope and Other RF Systems: Dc Through X-Band," _IEEE Trans. Microwave Theory and Techniques_, vol. MTT-14, pp. 629-635, December 1966.

8. J. Merkelo and R. D. Hall, "Broad-Band Thin-Film Signal Sampler," _IEEE J. Solid-State Circuits_, vol. SC-7, pp. 50-54, February 1972.

9. See, for Example, the "Special Issue: Symposium on Microwave Strip Circuits," _IRE Trans. on Microwave Theory and Techniques_, vol. MTT-3, March 1955.

10. L. Mandel and D. Meltzer, "Theory of Time-Resolved Photoelectric Detection of Light," _Phys. Rev._, vol. 188, pp. 198-212, December 5, 1969.

11. S. Methfessel, "Zum Äusseren Lichtelektrischen Effekt Der Alkalimetalle," _Z. Physik_, vol. 147, pp. 442-464, 1957.

12. N. C. Wittwer, "Detection of Higher Order Ruby Optical Maser Modes," _Appl. Phys. Lett._, vol. 2, pp. 194-196, May 15, 1963.

13. K. R. Crowe and J. L. Gumnick, "Enhancement of Photoelectric Quantum Efficiency in the Near Infrared," _Appl. Phys. Lett._, vol. 11, pp. 249-250, October 15, 1957.

14. D. K. Schroder, R. N. Thomas, J. Vine and H. C. Nathason, "The Semiconductor Field-Emission Photocathode," _IEEE Trans. on Electron Devices_, vol. ED-21, pp. 785-798, December 1974.

15. N. S. Khlebnikov and A. E. Melamid, "O Raspredilenii Fotoelectronov po Energiam i Uglam Vyleta dlia Slozhnykh Katodov," _Radiotekhnika i Elektronika_, vol. 4, pp. 1008-1017, June 1959.

16. _Electro-optics Engineering Notes_, published by Sylvania Electronic Systems, Mountain View, CA, #5-1, October 1970.

FIGURE CAPTIONS

Fig. 1. Illustration of the sampling geometry.

Fig. 2. Superposition of the waveform expressed by (1), for $V_o = 14.2V$ and $\Gamma = 68$ psec, on an oscilloscope trace of a driving potential $v(t,z_o)$. Vertical scale: 2V/div; horizontal scale: 20 psec/div.

Fig. 3. Illustration of waveforms encountered in optoelectronic sampling. A. Waveform of the envelope of optical radiation incident on the detector. B. The sampling potentials. C. The sampling function effected by $v(t) - V_r$. D. The sampler output shown on a time axis scaled by $\frac{T}{\Delta t}$.

Fig. 4. Example of the time relationship between $v(t)$ and $f_s(t)$ shown on 10 psec/div horizontal scale for two values of V_r. The values of τ are 9.6 and 4.9 psec for V_r of 12.3 and 12.7V, respectively. Other parameters are $V_o = 14.2V$, $\Delta x = 10\mu m$, $\gamma = 0$, $\Gamma = 68$ psec; $g_\lambda(v_x)$ corresponds to cesium-antimony at $\lambda = 6200\text{Å}$.

Fig. 5. Graphical representation of quantities defining the quality parameters η_E and η_F.

Fig. 6. Dependence of τ and η_E on V_r at $\lambda = 6200\text{Å}$, for five values of drift space dimension $\Delta x_{1,2,3,4,5} = 10,20,30,40$, and 50 μm, respectively. The monotonic increase of η_E with decreasing Δx is shown by the constant τ line, labeled 7 psec.

Fig. 7. Dependence of τ and η_E on V_r at $\lambda = 4047\text{Å}$, for five values of drift space dimension $\Delta x_{1,2,3,4,5} = 10,20,30,40$, and 50 μm, respectively.

Fig. 8. Dependence of τ and η_E on V_r for $\Gamma_{1,2,3} = 100,80$, and 60 psec, respectively.

Fig. 9. Illustration of the effect of emission delays, described by (15) and (16), on τ and η_E for $\gamma_{0,1,2,3,4} = 0,18,36$, and 54 psec, respectively.
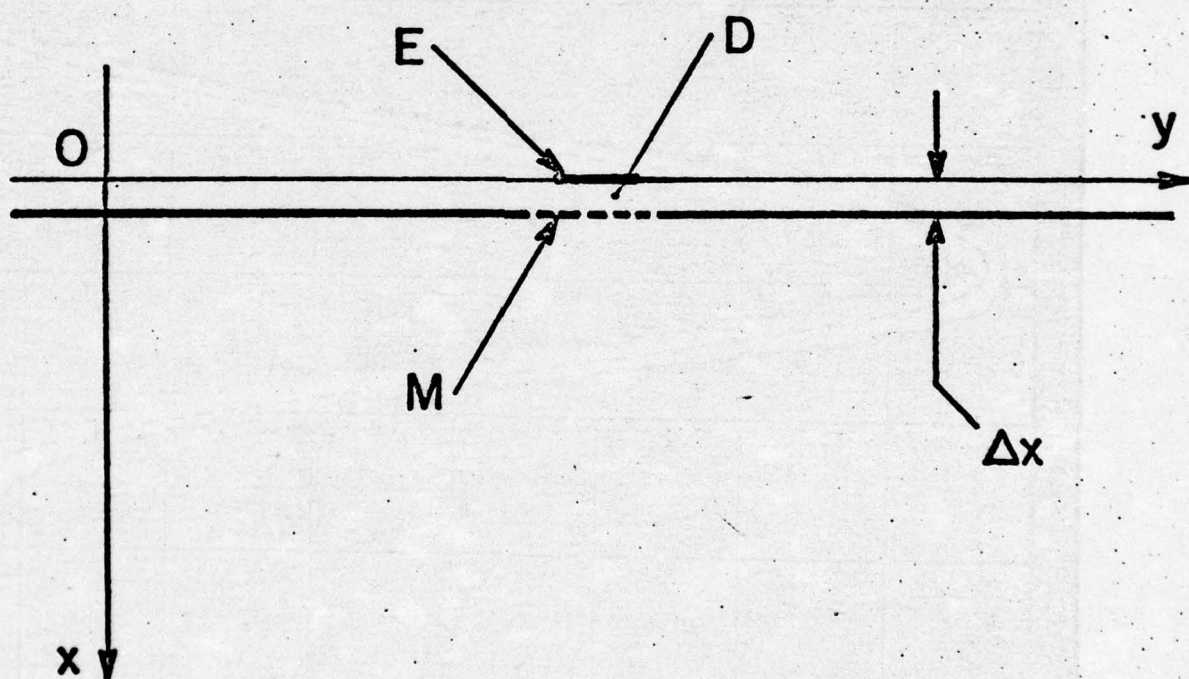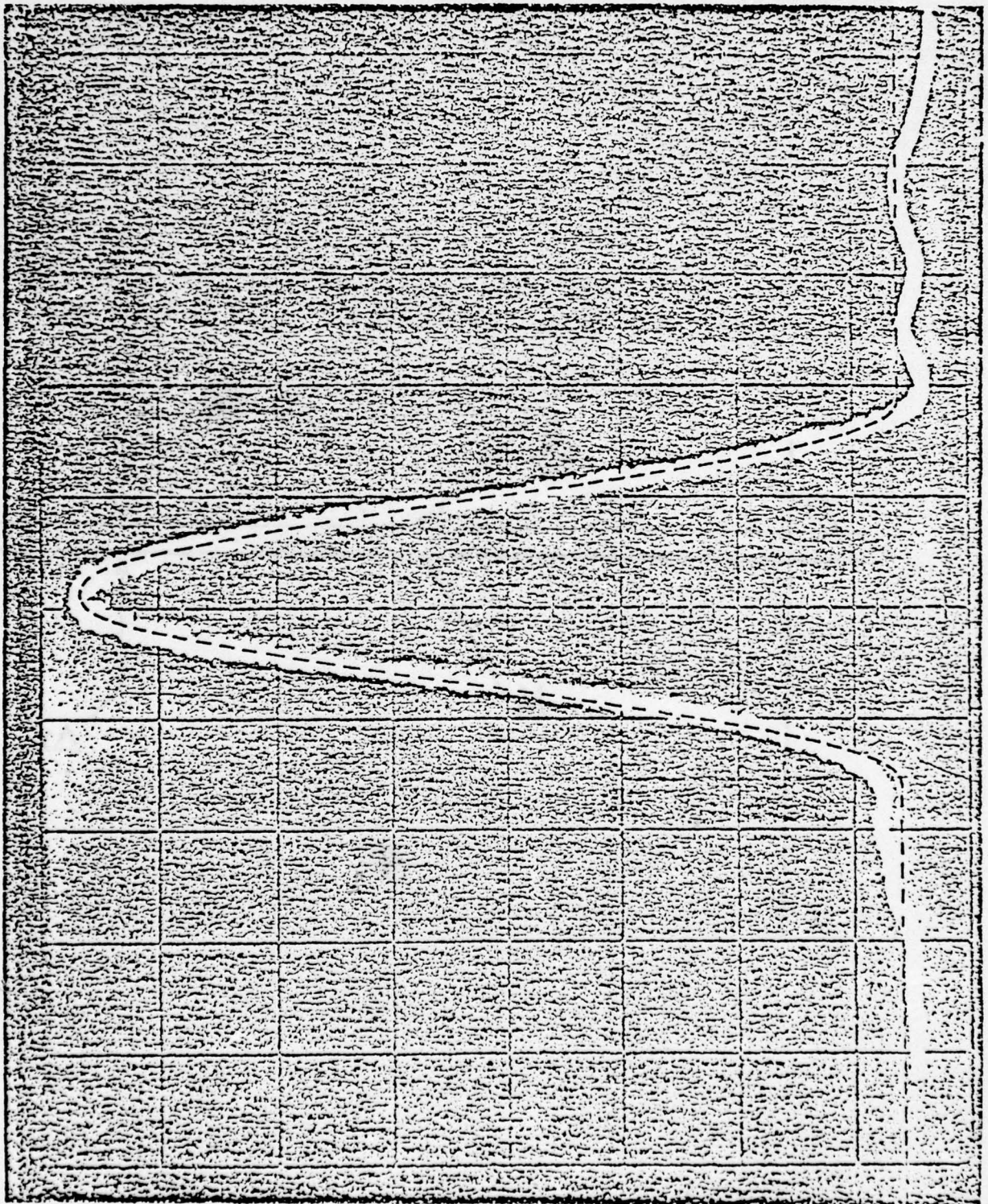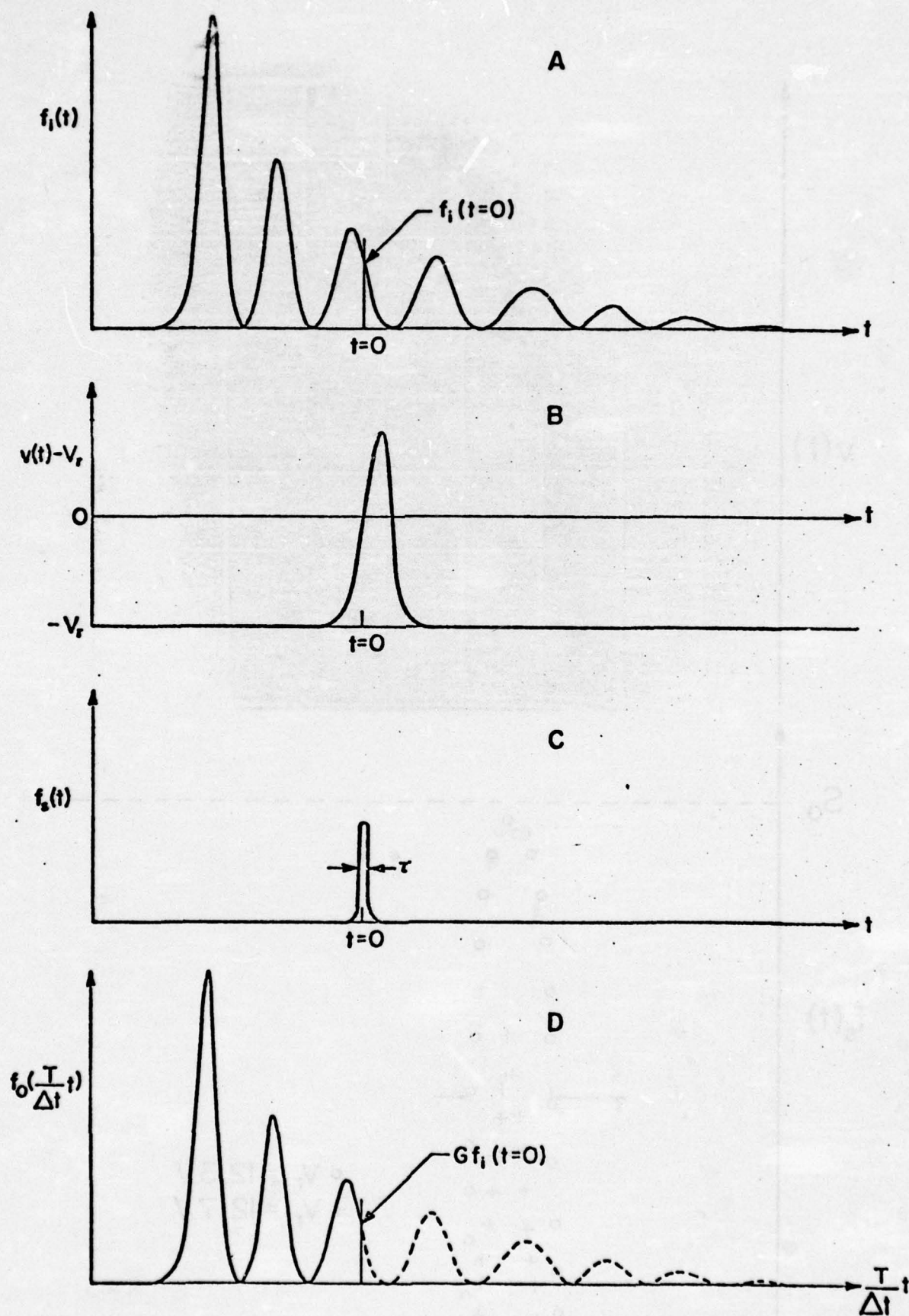
Figure 1.

Figure 2.

Figure 3.

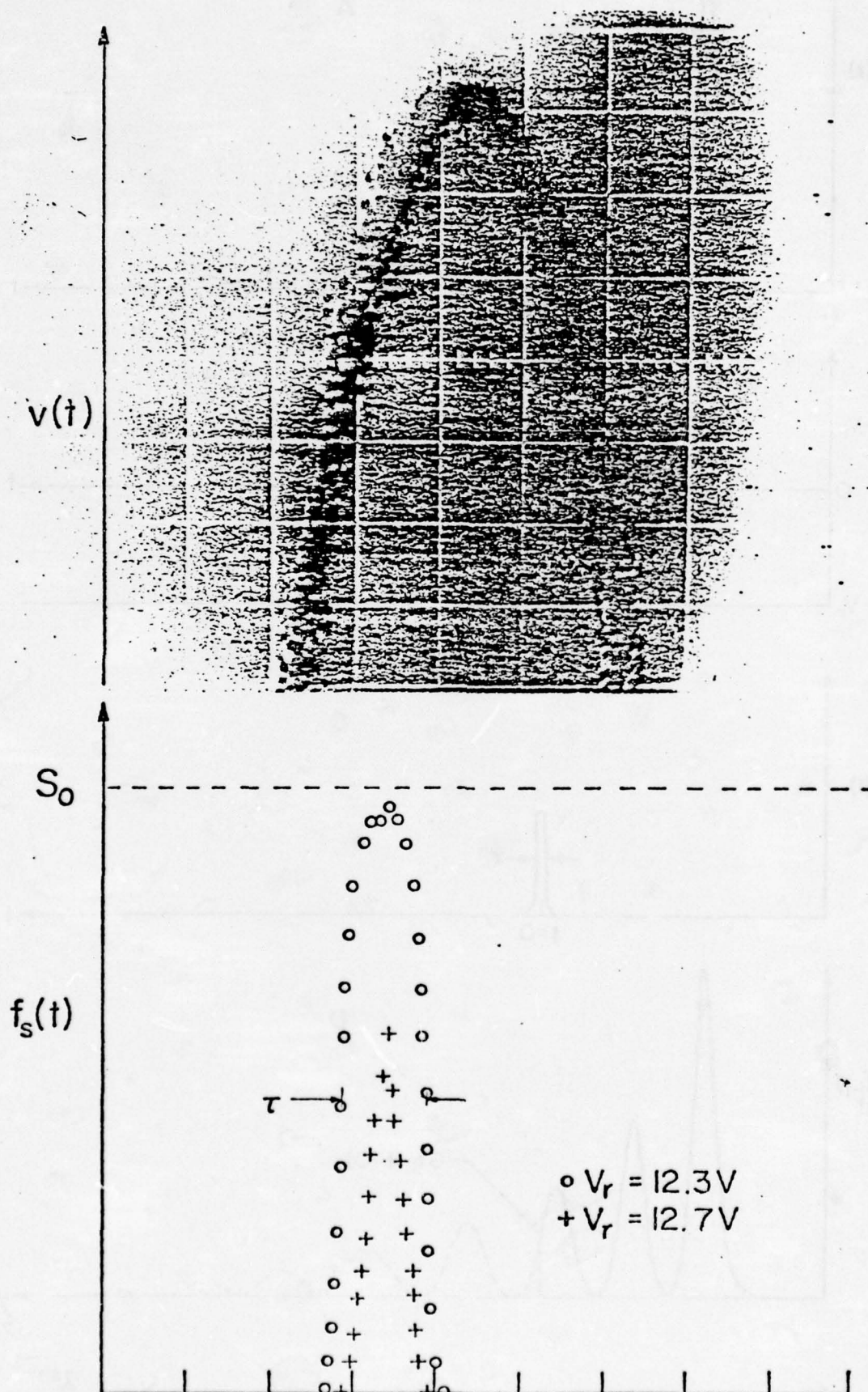$v(t)$

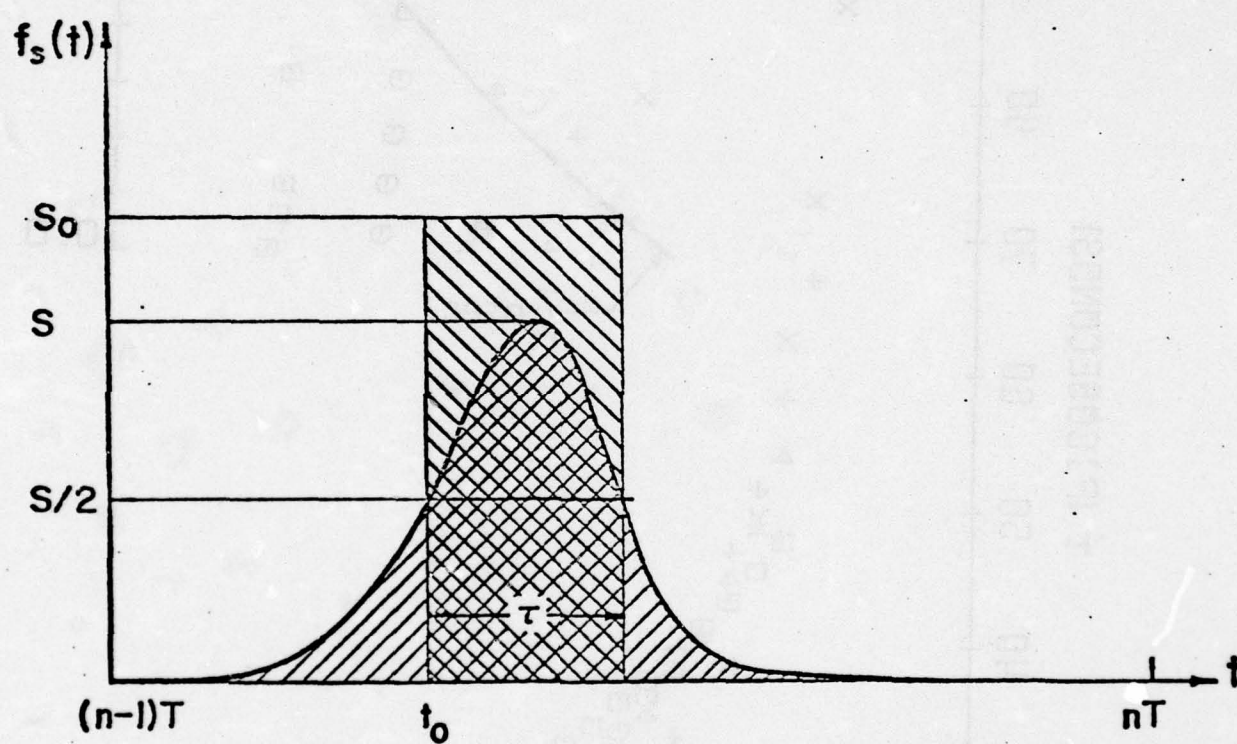S_0

$f_s(t)$

τ

$\circ\ V_r = 12.3\,V$
$+\ V_r = 12.7\,V$
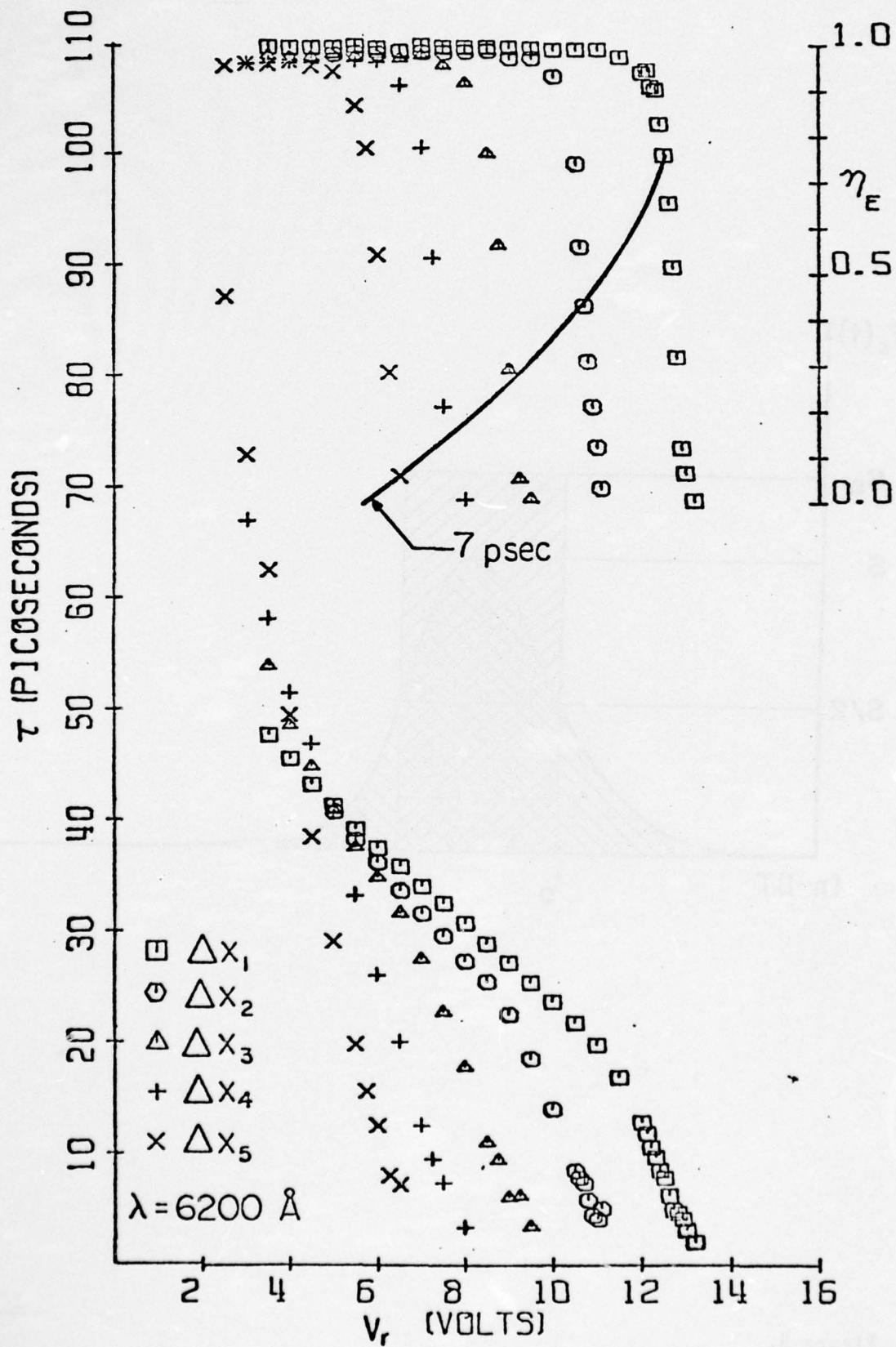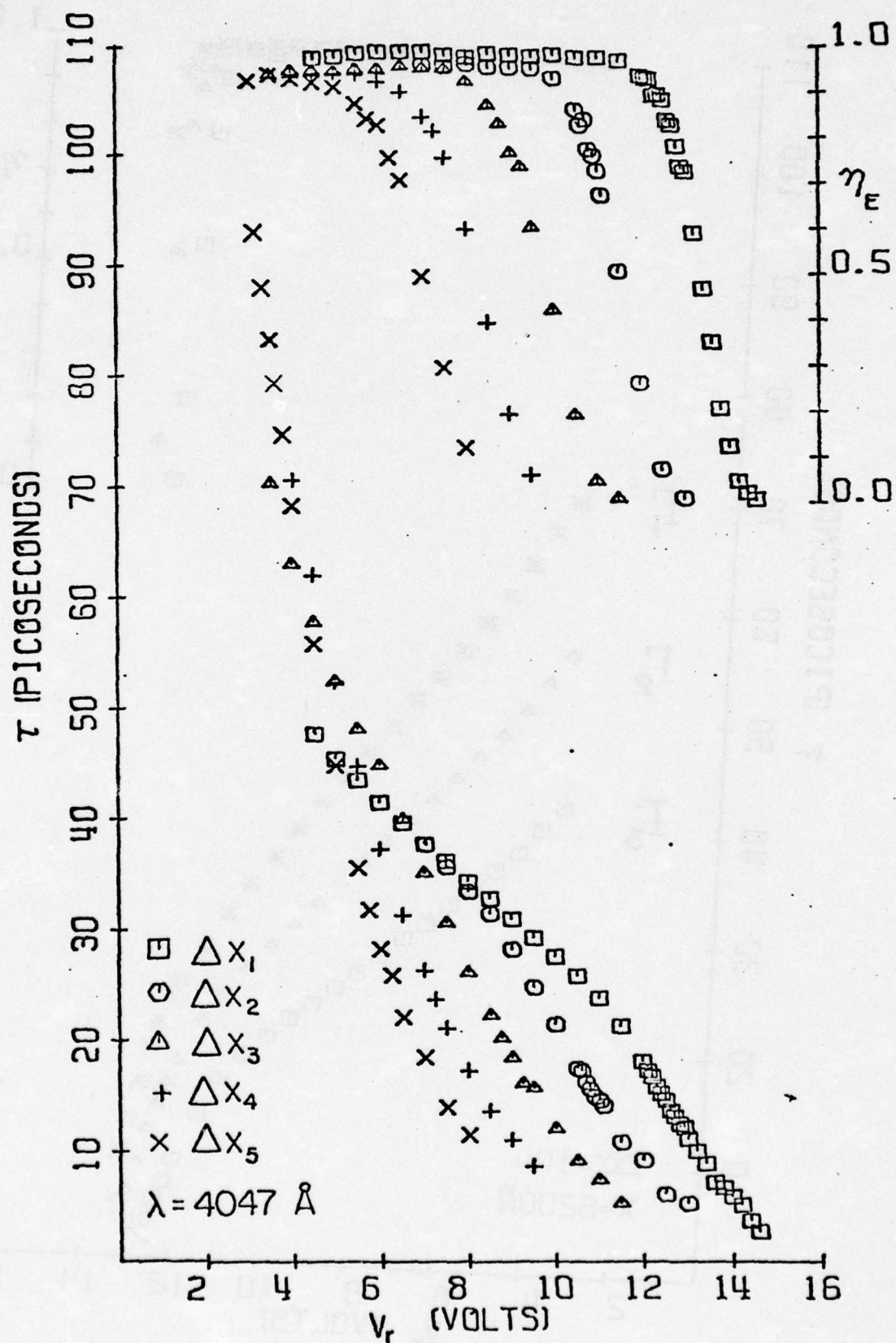
Figure 4.
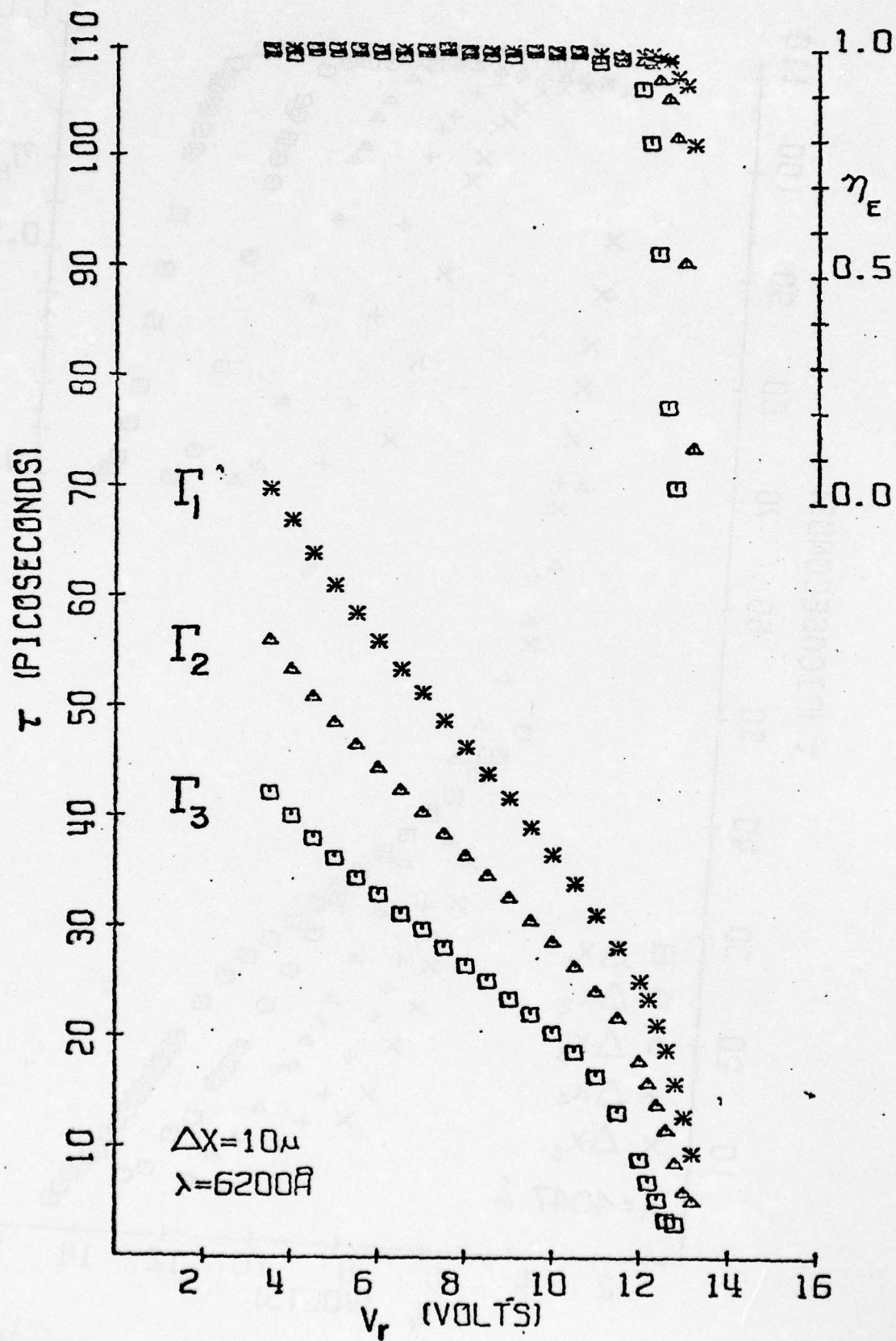
144

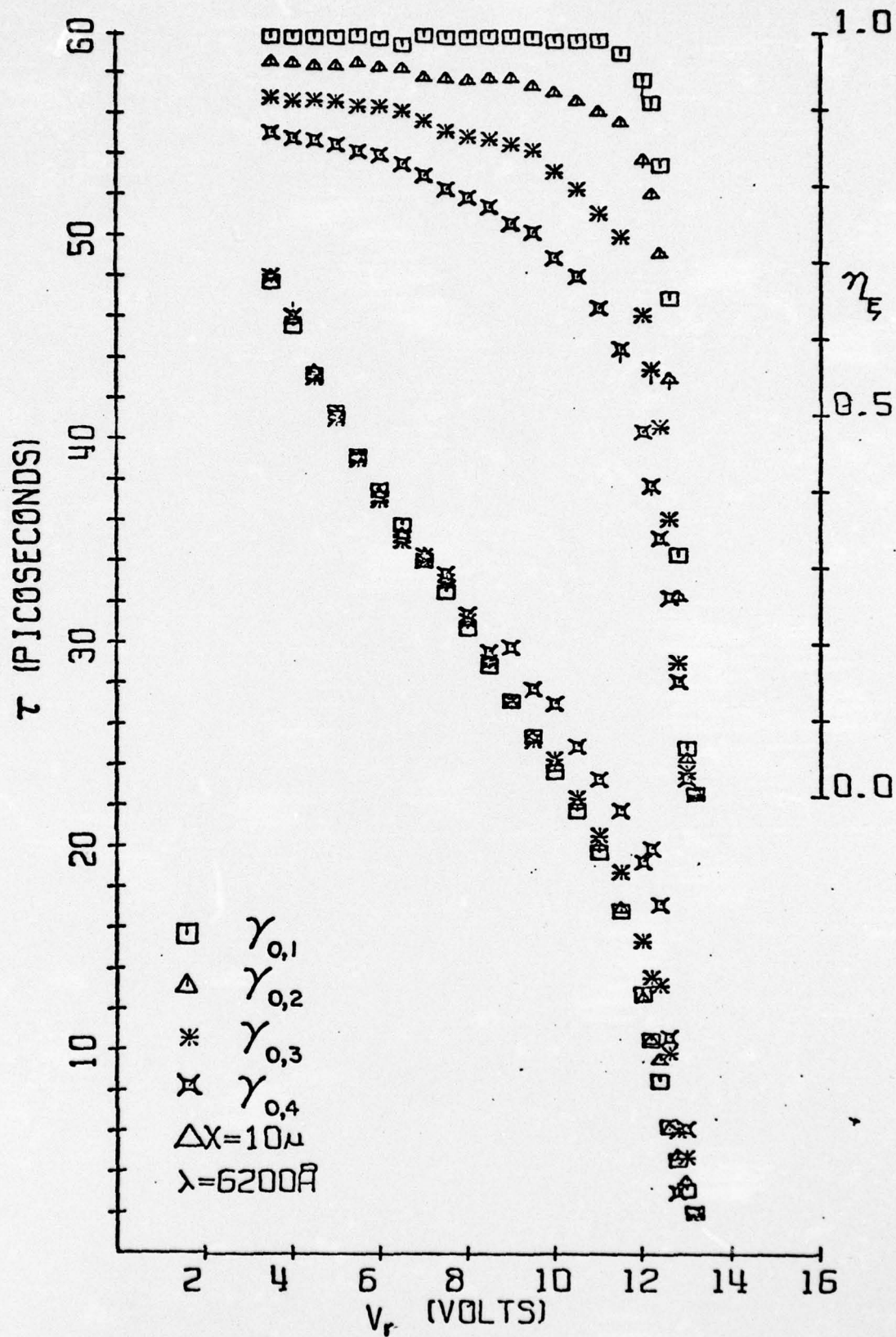Figure 5.

Figure 6.

146

Figure 7.

Figure 8.

Figure 9.

B-VI

Adaptation of Optoelectronic Sampling to the

Study of the Dynamics of Photoemission

Spectral response, quantum yield, and the electron velocity distri-
bution of photoelectric emission have been the standard parameters used
in interpreting the mechanisms of photoemission. Even in the study of
Garbe[1] on the factors affecting photoemission from cesium oxide covered
GaAs, a negative-electron-affinity material, no consideration is given
to the time evolution of photoemission; average escape depths are com-
puted on the basis of quantum yield and optical absorption coefficients.
We can estimate only indirectly (and with a large margin of error) the
time response of such materials. Clearly, the considerations discussed
at the end of Section B-V and the questions they raise are not resolved
by simple escape depth estimates.

The tools for studying the entire evolution of photoemission on
picosecond time scales can now be designed and fabricated. We propose
to use our existing, cw-operated, mode-locked dye laser for the source
of tunable, picosecond pulses. The time resolved detection of photoelec-
trons will be carried out with an apparatus based on an adaptation of the
high-speed sampler described in Section B-V. Since all studies on photo-
emission require electron energy separation, the high-speed sampler must,
fortuitously, operate under idealized conditions, i.e., if the photoelec-
trons are passed through an energy filter before entering the drift space
D of the sampler, the analysis of the sampling process is reduced to the
limiting case -- given as example on p. 14, B-V -- corresponding to
$g_\lambda(\nu_x) = \delta_\lambda(\nu_x - \nu_{xo})$. Under these conditions of monoenergetic photoelec-
trons, the resolution of the sampler is highest. Picosecond sampling
should be achievable for materials with a good quantum yield.

150

A schematic of the high-speed, microstrip sampler adapted to a velocity-selective, time-evolution measuring apparatus is shown in Figure 1. A thin strip photoemitter E is placed at a distance from the microstrip sampler such that photoelectrons are first accelerated into a magnetic field B oriented perpendicularly with respect to their velocity. For any one value of B, only one velocity group of photoelectrons will be incident on the strip M_1 of the sampling configuration. This strip is now designed as a meshed slit. All other components and configurations are the same including the conventional electron multiplier for the amplification of the sampled current. The analysis of Section B-V simplified since $g_\lambda(v_x)$ is always $\delta_\lambda(v_x - v_{xo})$. If within any period n, $f_i(t) \propto \delta(t - t_n)$, then, for any given magnetic field B_j, $j = 1,2,\ldots,$ the apparatus measures $G_\lambda(v_x,\gamma)\big|_{v_x = v_x(B_j)}$. A magnetic field scan yields the entire $G_\lambda(v_x,\gamma)$.

Since no such measurements have been made in the past, there appears to be no need at this time to reconsider our understanding of the time evolution of photoemission. However, it is anticipated that the processes controlling the evolution of photoemission, diffusion and tunneling, will be manifested quantitatively in these time studies, allowing for revision. Adding to the basic understanding of electron emission from surfaces, the results of these efforts should also contribute to our ability to characterize photoactive materials for high-speed optoelectronic applications.

[1] S. Garbe, "Factors Affecting the Photoemission from Caesium Oxide Covered GaAs," Solid-State Electronics, vol. 12, pp. 893-901, 1969.
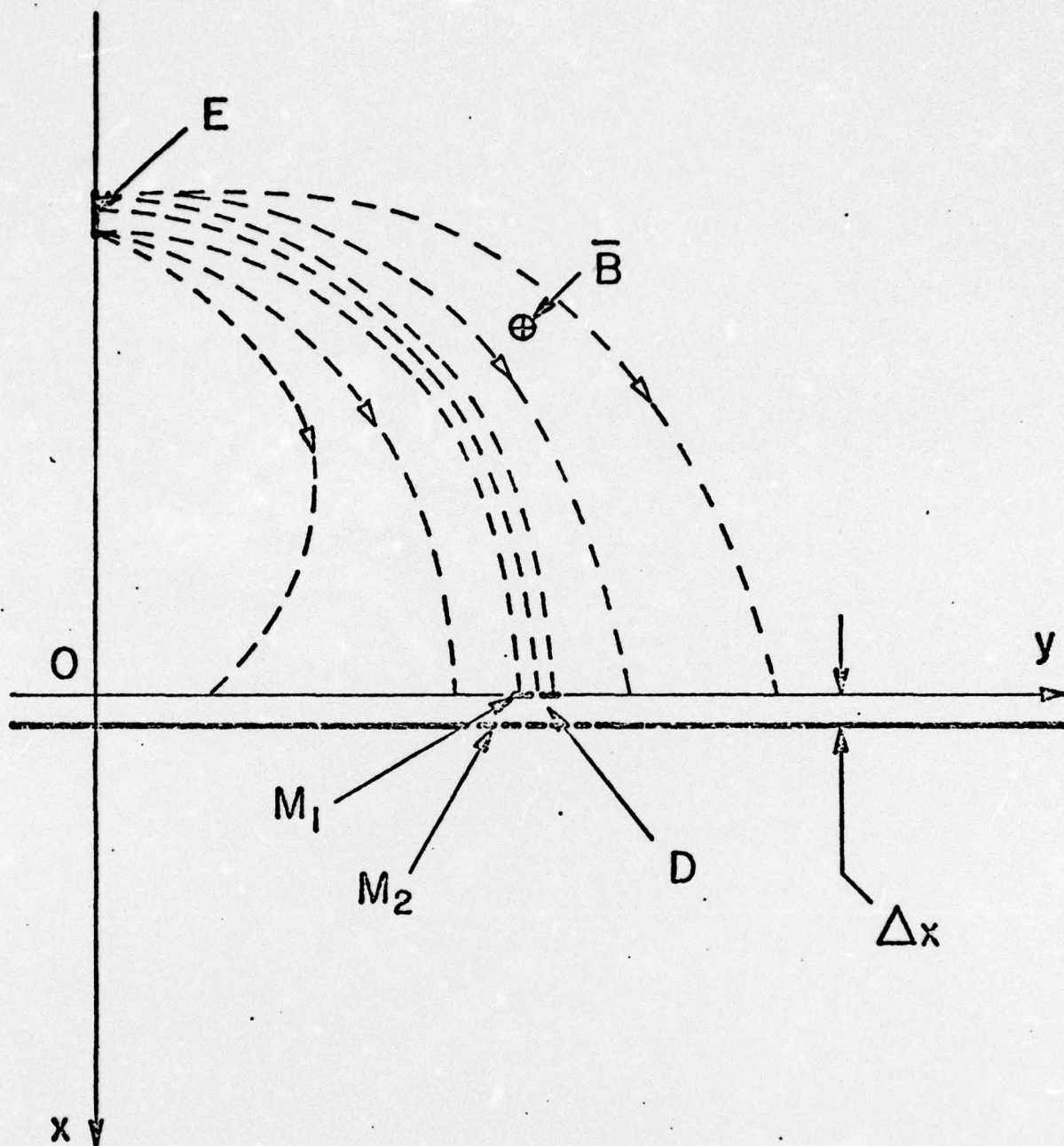
Fig. 1. Illustration of the geometry of an electron sampler including
a photoelectron energy separating provision: E, photoemitter;
D, drift space; M_1, meshed strip; M_2, meshed ground plane;
Δx, drift space dimension.

33

United States Patent [19]

Merkelo

[11] **3,941,998**

[45] **Mar. 2, 1976**

[54] **OPTOELECTRONIC SAMPLING HEAD**

[75] Inventor: **Henry Merkelo**, Urbana, Ill.

[73] Assignee: **The University of Illinois Foundation**, Urbana, Ill.

[22] Filed: **Feb. 26, 1974**

[21] Appl. No.: **446,051**

[52] **U.S. Cl.** .... 250/207; 250/211 R; 313/95; 313/99
[51] **Int. Cl.²** H01J 39/00; H01J 39/12; H01J 39/14
[58] **Field of Search** .... 250/207, 211 R; 313/99, 313/95; 250/211 R; 313/95

[56] **References Cited**
UNITED STATES PATENTS

3,327,152	6/1967	Greilich	313/99
3,375,391	3/1968	Day	313/99
3,446,971	5/1969	Ruddock	250/207

Primary Examiner—James W. Lawrence
Assistant Examiner—T. N. Grigsby
Attorney, Agent, or Firm—Daniel M. Rosen

[57] **ABSTRACT**

An electronic sampling head comprising a housing having a path for impinging radiation, a photoemissive element positioned across said path, photoelectron ejection means positioned in proximity to said photoemissive element, means for applying ultrashort sampling potential differences between said photoemissive element and said photoelectron ejection means for accelerating photoelectrons emitted by said photoemissive element in response to said incident radiation, and means for detecting said photoelectrons, all resulting in the capability of detecting high-speed radiation phenomena with waveform fidelity.
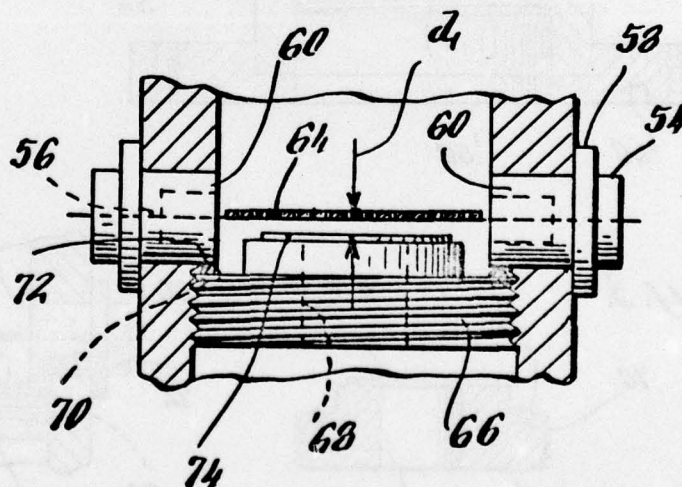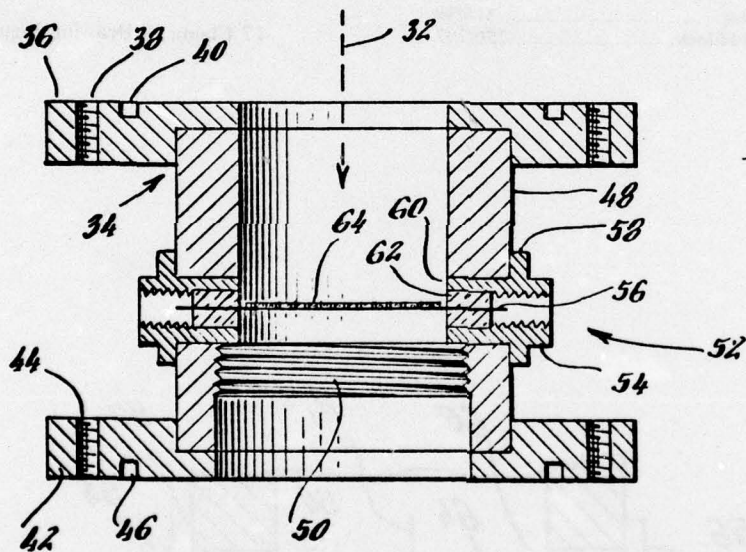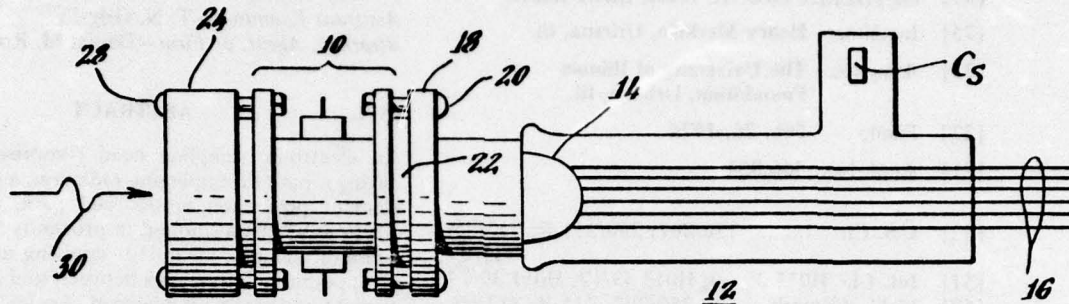
17 Claims, 9 Drawing Figures
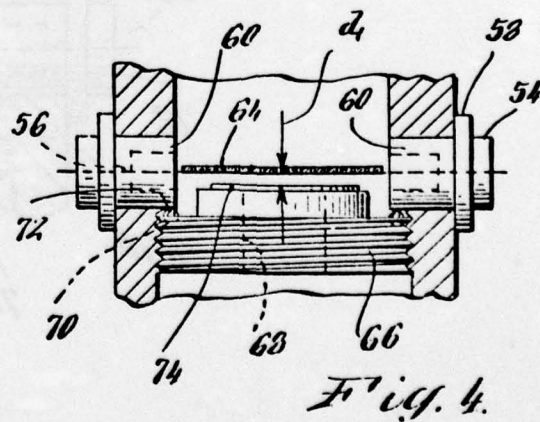
Fig. 1.

Fig. 2.

Fig. 3.

WIRE MESH

Fig. 4.

Fig. 5.

66

64

72

d_2

74

68

+V₀

76

78

82

80

PULSE GEN.

⊓ -Vₛ

BIAS TEE

56B

+Vᵦ

S.H.

E.M.

Vₛ

56A

30 10

12

84

Fig. 6.

155
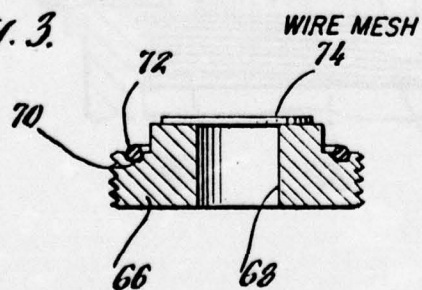
Figure 7. Sampling function width, τ, and sampling efficiencies η$_τ$ and η$_A$ as a function of retarding potential for sampling pulses of 10 V peak, 100 psec basewidth; light at λ = 6200Å; cesium-antimonide photocathode.
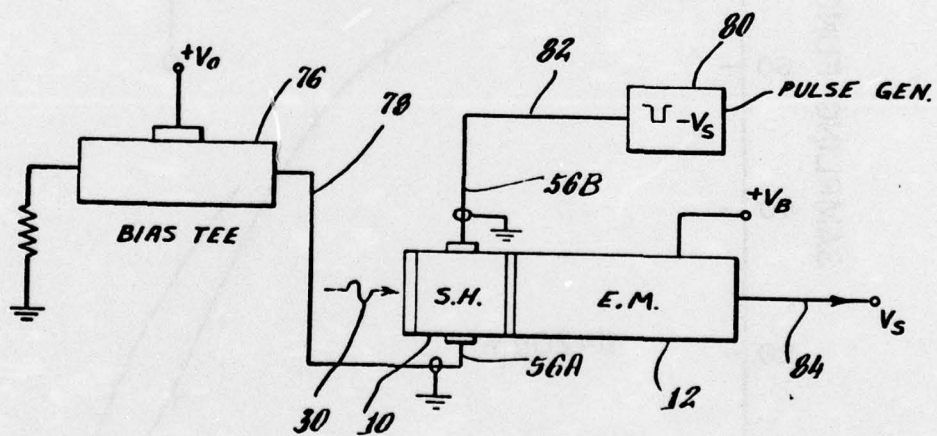
Figure 8. Sampling function width, τ, and sampling efficiencies η_τ and η_A as a function of microstrip spacing for sampling pulses of 10 V peak, 100 psec basewidth.

157

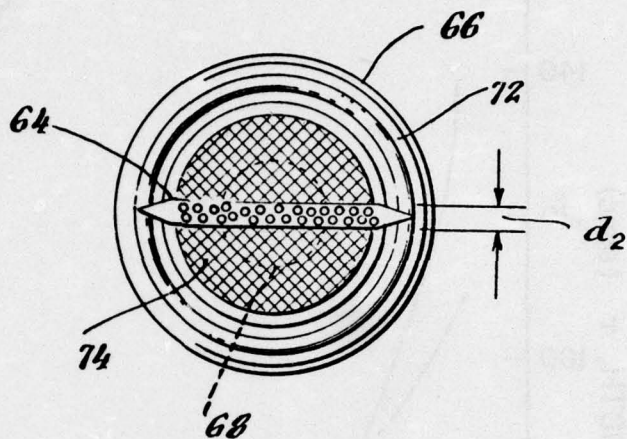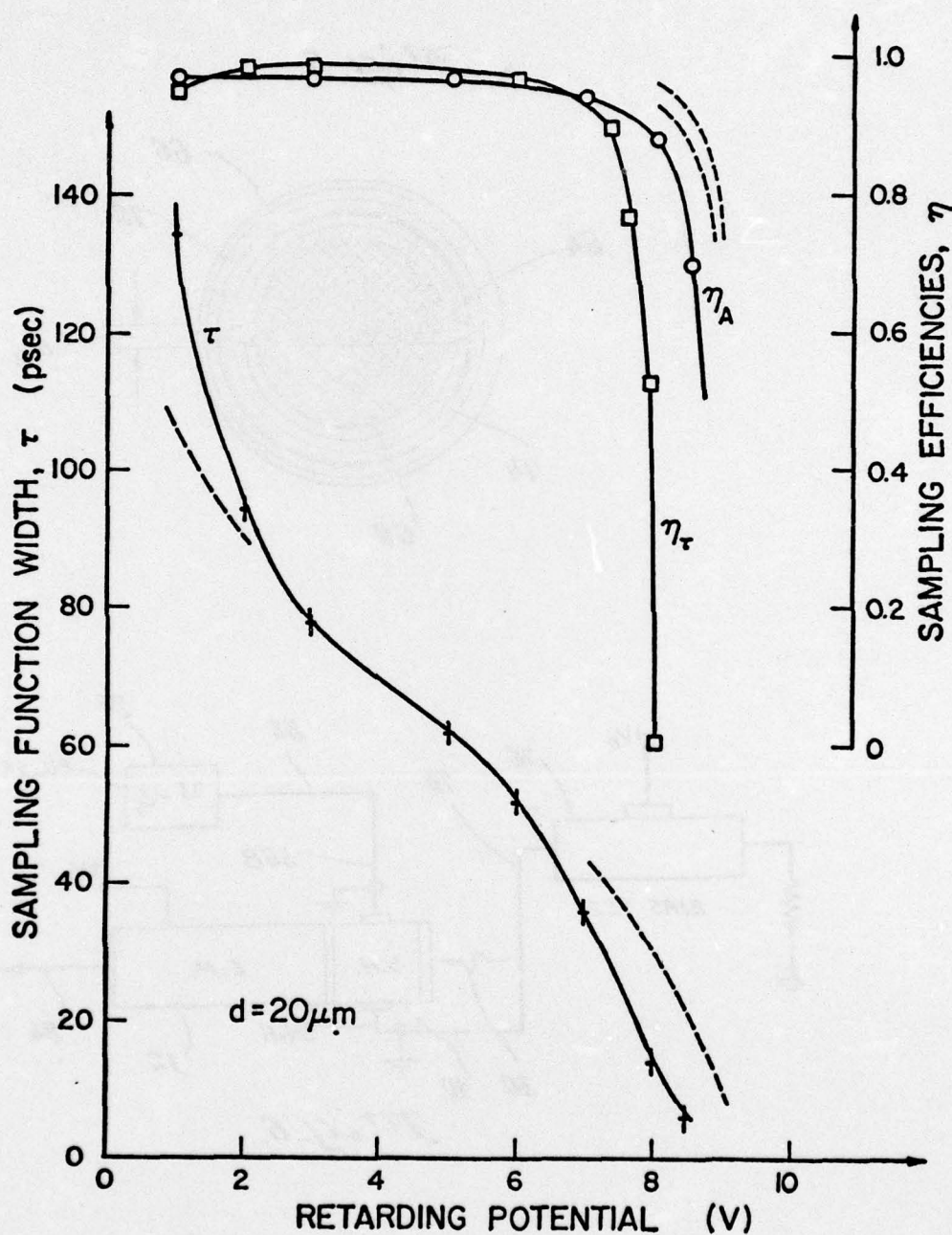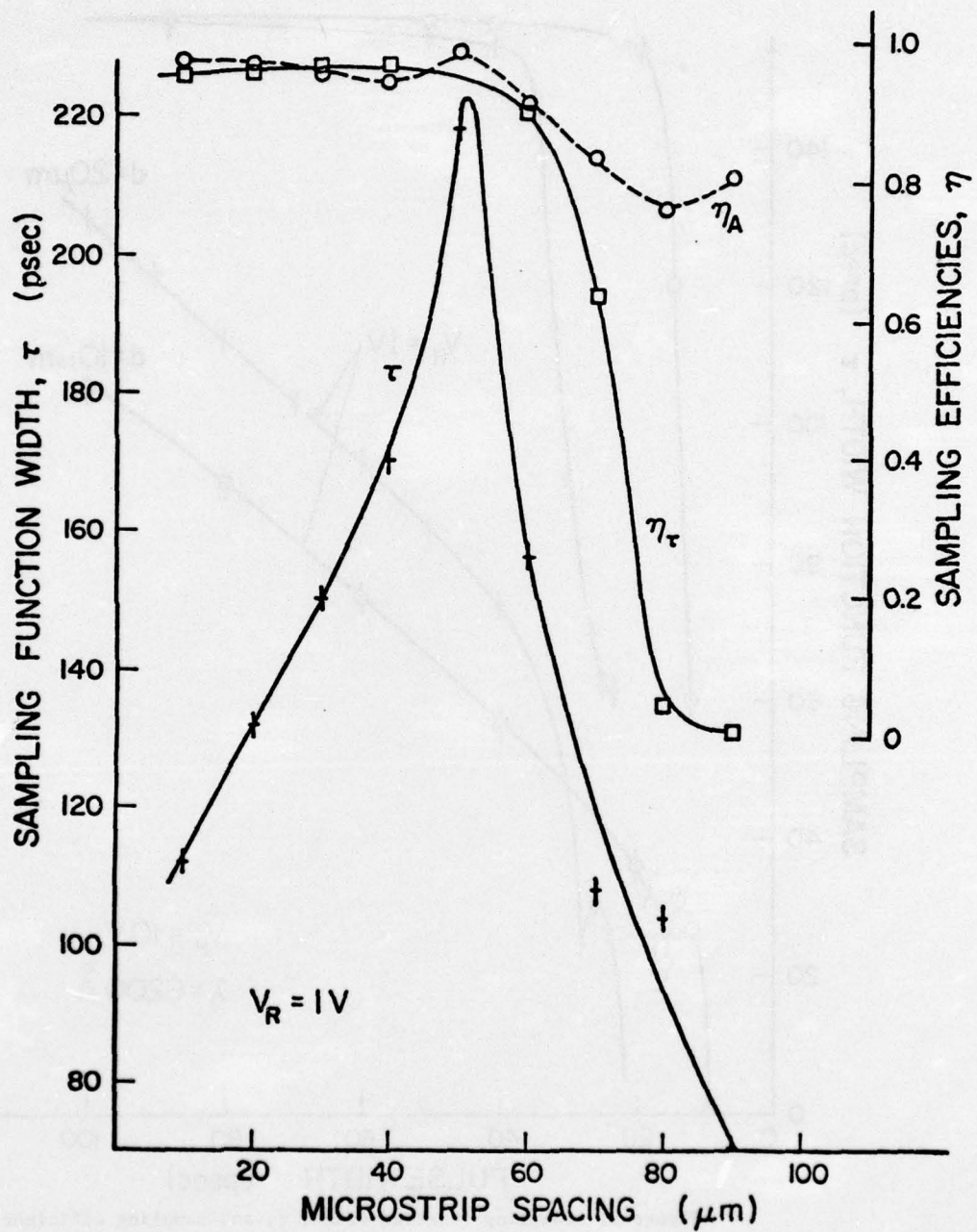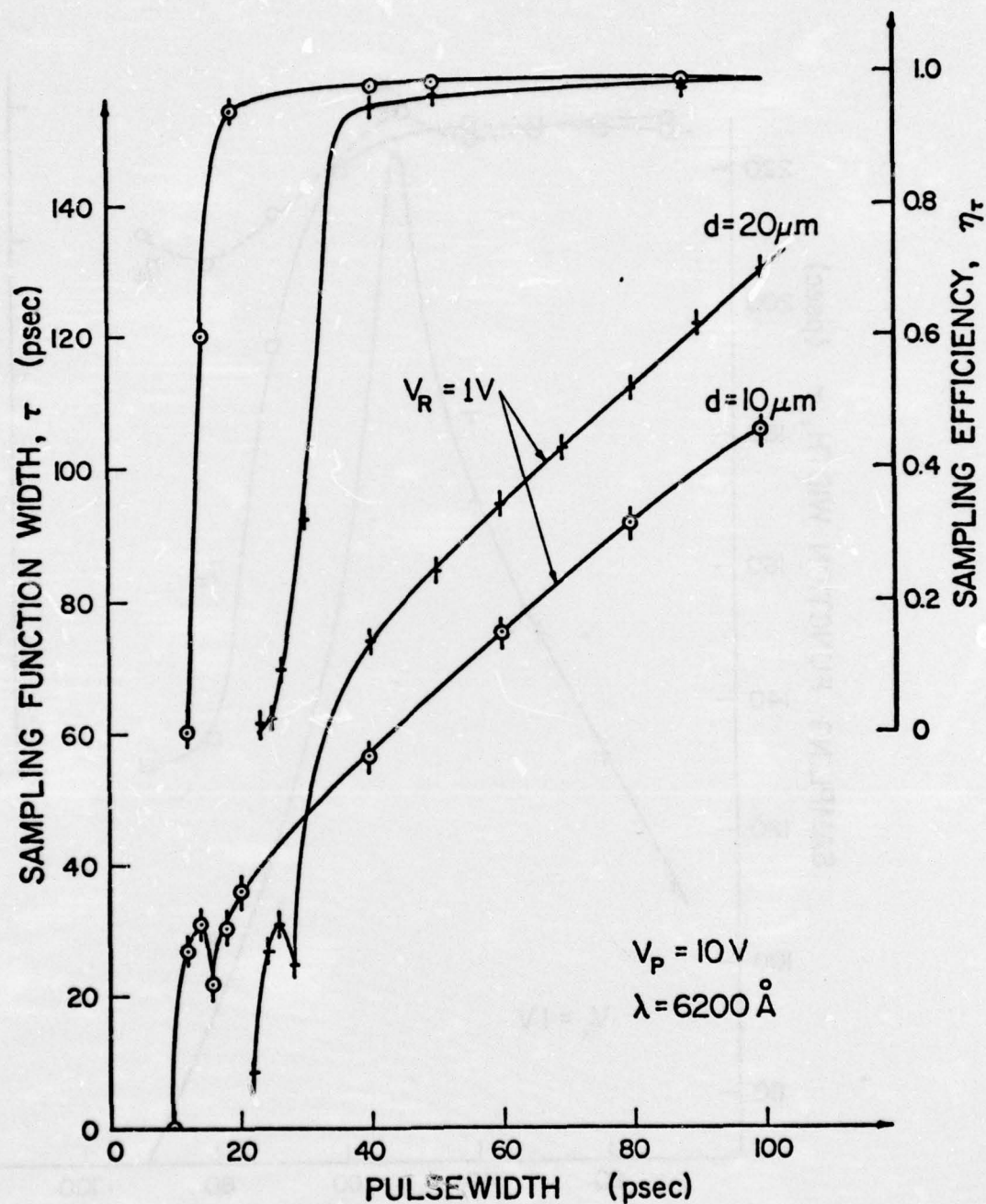**Figure 9.** Sampling function width, τ, and sampling efficiencies η_τ and η_A as a function of sampling pulsewidth for sampling pulses of 10 V peak; light at $\lambda = 6200\overset{\circ}{A}$; cesium-antimonide photocathode.

1

OPTOELECTRONIC SAMPLING HEAD

The invention herein described was made under a contract with the Department of the Navy.

This invention relates to optical detection devices and specifically to optical sampling heads usable in conjunction with photoelectron amplifying devices suitable for low power radiation detection.

A need exists for a high resolution sampling detector for detecting radiation levels, particularly optical, at relatively high sampling speeds. Since in many applications the photon flux level at high sampling speed will be low, a sensitive device for detection is required.

A conventional form of detection device is the photomultiplier. In its usual form, the single stage device employs a photocathode, emitting electrons in response to impinging radiation, a secondary emissive electrode or dynode, and a collector electrode or anode. In a multistage electron multiplier, a cascade of dynodes are employed, with successively higher biasing potentials, such that impinging primary electrons cause emission of secondary electrons in a multiplying progression from successive dynodes, and are ultimately collected by the anode which in turn provides an output signal.

It is desirable to utilize an electron multiplier for providing high resolution, high speed sampling of optical radiation; however, conventional photocathodic detecting structures do not possess adequate resolution nor speed to enable rapid sampling of optical signals, particularly in the measuring or detecting of a rapidly varying light level. Such light levels, which may be laser generated, may require sampling rates approaching the picosecond range. Additionally, the use of high sampling rates is best controlled electronically, at the actual sampling point. This latter feature is difficult to achieve in conventionally gridded photomultiplier structures.

It is therefore the primary object of the present invention to provide a sampling device which is operable with high resolution over a short sampling time.

It is another object of the present invention to provide a sampling device adapted to be employed with a conventional electron multiplier for improving the resolution thereof.

It is a further object of the present invention to provide a sampling device which may be electronically controlled to produce sampling intervals of shorter duration than heretofore possible while maintaining high resolving characteristics.

The foregoing objects are realized in a device constructed of a housing having a path for impinging radiation and a photoemissive element positioned across said path. A photoelectron ejection electrode is positioned adjacent the photoemissive element and a sampling potential difference can be applied across the element and electrode. Any electrons emitted by the element due to the incident radiation thereon during the sampling pulse duration is accelerated through the ejection electrode to a suitable detection device such as a conventional electron multiplier. The device structure includes an elongated photoemissive strip located in close proximity to the ejection electrode, the latter taking the form of a circular wire mesh. The width of the strip and its distance from the mesh are set with predetermined relationship for optimum, high-speed results.

2

The foregoing objects and brief description of the present invention will become more apparent from the following detailed description and appended drawings wherein

FIG. 1 shows the head of the present invention utilized with an electron multiplier;

FIG. 2 is a cross section along the optical path of the head showing the housing and photoemissive strip;

FIG. 3 illustrates the insert and ground plane element;

FIG. 4 shows the insert in position in the housing;

FIG. 5 is a top view showing the relationship of the strip to the underlying ground plane forming a microstrip configuration.

FIG. 6 is an illustration of the circuit utilizing the head of the present invention; and,

FIGS. 7, 8 and 9 illustrate as examples the graphical relationships of the effect various dimensional parameters and biasing have on resolution and efficiency.

Referring to FIG. 1, sampling head 10 constructed in accordance with the present invention is shown in mounted position on a conventional electron multiplier 12. For purposes of illustration, the electron multiplier may be that of an RCA Model 7102 photo-tube including a dynode/anode structure 14 including a plurality of voltage leads 16 for applying a potential to the dynode/anode electrode structure 14. Other conventional electron multipliers may also be employed with the sampling head. The photo-tube 12 has been modified to the extent that an external source of electrons, supplied by the sampling head 10, may be provided. To this end, a flange 18 including mounting bolts 20 provides a support frame for mounting the head 10 to the tube 12. An O-ring seal 22 may be provided to vacuum and optically seal the head outlet to the tube inlet.

On the left side of the head 10, referring to FIG. 1, a lens or window unit 24 is bolted to the optical inlet side of the head 10. A further O-ring seal 26 may be used to vacuum seal the optical element through the head. The head is bolted by means of bolts 28 to the lens structure 24.

Incident radiation 30 impinges, through the lens 24, upon the photosensitive surface creating photoelectrons which are sampled by the head 10 in a manner to be set forth in further detail below, and the resulting electron flow multiplied in the electrode structure 14 of the electron multiplier 12.

The structure of the sampling head 10 is shown in greater detail in FIGS. 2–5. The cross section FIG. 2 shows that the sampling head includes a central optical path 32 passing through a housing indicated generally as 34. The upper flange 36 of the head structure 34 includes bolt holes 38 for accommodating the bolts 28, and a groove 40 for accommodating the O-ring 26, shown in FIG. 1. The lower flange 42 of the head structure 34 includes bolt holes 44 for accommodating the bolts 20, and a groove 46 for accommodating the O-ring 22.

The housing 34 further includes a side wall 48 which may be square or circular in shape. The internal passage way 32, axially defining the optical path, is preferably round in shape and includes a plurality of threads 50 formed in the interior wall for accommodating an insert, shown in FIG. 3. The housing 34, including flanges and side walls, as preferably constructed of a cold rolled steel or like sturdy conductive material.

Incorporated into the side walls 48 are a pair of feed-through leads 52 which include a conductive cap 54

3

having provision for attaching or incorporating a conductive wire **56**. The cap **54** is supported on the housing by a support flange **58**. The feedthrough is formed as a plug fitting into the wall **48**, and includes an outer conductive shell **60** and an inner glass feedthrough member **62**. Through the feedthrough is connected a conductive photoemissive strip **64**, composed of a suitable photoemissive material such as cesium antimony or the like. The strip may be finely perforated or semi-transparent, or formed as a mesh, and has tapered ends. The component material structure of the feedthrough is designed to permit the coupling of the broadbound high frequency sampling signals to the strip **64**.

The strip **64** is positioned across the optical path **32**.

The insert **66**, FIG. 3, is a conductive, externally threaded, round plug-like component including a central electron path **68** and a groove **70** for accommodating a spacer **72**. The upper part of the insert **66** includes a fine wire mesh **74** which can be circular and which is affixed to the insert **66** as by spot welding or the like. The wire mesh **74** performs the function of a photoelectron ejection electrode in cooperation with the photoemissive strip **64**, and requires a certain spacing with respect to the strip **64** for electronic matching in a microstrip configuration. The insert **66** is positioned into the body of the structure **34** by rotating the mating threaded portions of the insert **66** and the interior **50** of the housing **34** until the spacer **72** contacts the lower projecting portion of the shell **60**, shown in FIG. 4. Accurate control of the spacer dimension will control the spacing distance d_1 between the strip **64** and the microstrip ground plane which acts as an ejection electrode **74**. The electrode **74** is termed an ejection electrode in that it performs the function of causing electrons from the strip **64** to be ejected into the path **32**.

The top of the assembly, viewed in the direction of the optical path **32**, is shown in FIG. 5. The strip **64** is designed to have a predetermined width, d_2, across the optical path, which also provides maximum operational characteristics.

By way of example, the wire mesh may be constructed of a woven or etched nickel screen. Other conductive metallic materials compatible with phototube processing may also be employed.

Due to the high frequency of operation, the components forming the housing, insert, strip and feedthrough are, as shown in FIGS. 2–5, designed to be assembled employing techniques which will result in a broadband, nondispersive electrical system suitable for high vacuum construction. The relationship of the dimensions d_1 and d_2 are critical with respect to the device operation. These parameters are mutually interdependent in determining the mode propagation in accordance with broadband design criteria, and should be scaled to produce a reflectionless and dispersionless fundamental mode propagation. An example of such dimension selection will be found in the IRE Transactions of the Professional Group on Microwave Theory and Technique entitled, "Symposium on Microwave Strip Circuits", March, 1955.

According to the embodiment disclosed herein, where, as illustrated in FIGS. 7–9, resolution of optical pulse durations in the picosecond (10^{-12} seconds) range can be achieved. The spacing d_1 was chosen at 300 microns to which corresponds a strip width, d_2, of 1.5 millimeters, all designed in accordance with microstrip design criteria and matched for a 50 ohm termina-

4

tion. The optical path **68**, by way of reference, is about 1.5 inches in diameter.

The electron multiplier, which serves as the integrating-amplifier section, along with the output circuitry, is mounted in a large glass to metal seal. This is then brazed to an O-ring flange to allow the sampler portion to be bolted to the multiplier section. Before the two sections are joined together, antimony is deposited on the silver coated stainless steel strip by a vacuum-evaporation process. The strip is soldered to the center pins of the feedthrough connectors, and the sampling portion is bolted to the integrating amplifier section. Next, cesium gas is introduced into the previously evacuated system while the tube is baked in an oven at 150° C to form a cesium antimonide photocathode (Cs_3Sb).

Operation of the sampling head is set forth in FIG. 6. The head, **10**, in position on the electron multiplier **12**, is biased by applying a retarding potential V_o to the strip **64**. This potential V_o is applied through a conventional bias tee **76**, available from the General Radio Corp., for keeping the d.c. level free of sampling pulses. The potential V_o is supplied to the electrode **64** by contacting lead **78** to feedthrough lead **56A**, thereby rendering the potential of the electrode **74** negative with respect to the strip **64**. An optical signal **30** is directed to the sampling head, as described above. A sampling pulse is supplied by the sampling pulse generator **80** along the line **82** through the feedthrough lead **56B** to the strip **64**. The sampling pulse $-V_s$, applied to strip **64**, is negative with respect to the ground electrode **74** and serves to both cancel and exceed in magnitude the retarding potential V_o. Should radiation be incident upon the strip during the sampling pulse interval, electrons emitted from the strip **64** in response to incident photons will be accelerated by the potential difference toward the photoelectron ejecting element (the ground plane wire mesh **74**) and pass through the electron path **68** into the electron multiplier **12**. Since the electron multiplier, under the bias $+V_B$, serves to amplify the electron flow, an output signal V_s will be provided along line **84**.

By way of example, and with the spatial dimensioning set forth above, the sampling head was employed with an optical pulse of about 300 psec rise time derived from a mode-locked HeNe laser. Using a −7 volt, 250 psec wide sampling pulse, with Vo set at −2.2 volts, full time resolution of the mode locked laser pulses were achieved.

Referring to FIGS. 7, 8 and 9 graphical relationships showing the criticality of the dimensional relationships, as well as the effect of varying potential levels, and sampling pulse widthes are demonstrated.

The parameters found useful in characterizing the optoelectronic sampler are the sampling efficiencies η_τ, η_A and the pulse width τ. Thus, η_τ represents the ratio of the relative number of photoelectrons of the derived sampling function to the maximum possible number, $A_o\tau$, of photoelectrons that could be sampled in the same interval for the same set of conditions, and η_A represents the ratio of the sampled photoelectrons of the sampling function to the total number of sampled photoelectrons in the entire sampling function. Clearly, η_τ and η_A are maximally unity and are specified to designate amplitude sampling efficiency and sampling quality respectively.

As a result of this analysis, changes in η_τ, η_A and τ due to variations in the input conditions can be used to

5

optimize the output signal with respect to resolution and signal magnitude.

The retarding potential represents the constant voltage applied to the sampler structure which prevents photoelectrons from reaching the sampler anode at all times that the sampling voltage pulse is not present. When the sampling voltage pulse does occur with sufficient amplitude, the net voltage difference between the photocathode and anode can result in photoelectrons traversing the sampler drift space. As the retarding potential is increased, the effective time during which the photocathode is forward biased decreases, resulting in improved resolution, as shown in FIG. 7.

Although improved resolution is desirable, one must consider the effect of increased retarding potential on sampling efficiencies. η_{τ} and η_A tend to fall when the retarding potential is increased to a potential for which the effective duration of the sampling pulse is too short to allow those photoelectrons with comparatively small initial velocities to reach the anode.

FIG. 8 illustrates the effects of different spacings, d_1, between the photocathode and the sampler anode for a fixed set of parameters. From these numerical results, it can be shown that if the duration of the accelerating field is approximately equal to or smaller than the time necessary for all the emitted photoelectrons to traverse the drift space, then only those photoelectrons, if any, with large initial energies will be sampled. This results in a decrease in time dispersion due to the initial velocity spread of the photoelectrons as is illustrated in FIG. 8 for d_1 greater than 70 microns. Also note that the sampling efficiency η_{τ} rapidly deteriorates as fewer photoelectrons are collected.

FIG. 9 illustrates the dependence of the sampling function width and the sampling efficiency on the incident wavelength for a cesium antimonide photocathode. It should be noted that, in all cases considered, wherever the sampling efficiencies dropped, the order $\eta_A > \eta_{\tau}$ was preserved, indicating that though signal magnitudes could become small, signal fidelity would be retained. For the exemplary cesium antimony photocathode considered, it appears that the highest resolution and greatest sampling efficiencies occur in the red part of the visible spectrum. Those incident wavelengths which result in the narrowest range of energies for the emitted photoelectrons will be capable of the highest resolution since the transit time dispersion effect which degrades the time response to a sampling photomultiplier tube is due to the spread of initial velocities of the emitted photoelectrons.

Although the invention has been described in conjunction with certain preferred embodiments, it will be understood that other variations, modifications, substitutions, additions and deletions may be made within the framework and spirit of the invention.

What is claimed is:

1. A high speed sampling head for photoelectrons comprising a housing having a path for impinging radiation, a strip-shaped photoemissive element positioned across said path, planar photoelectron ejection means positioned in proximity to said photoemissive element in said path, means for propagating a high speed sampling potential difference between said photoemissive element and said photoelectron ejection means, means for accelerating photoelectrons emitted by said photoemissive element in response to said incident radiation, and means for detecting said photoelectrons, whereby

6

said ejection means constitute a microstrip ground plane for said photoemissive element.

2. The head of claim 1 wherein said photoelectron ejection means is a circular wire mesh.

3. The head of claim 1 wherein said photoemissive element is an elongated shaped strip across said optical path having a predetermined narrow dimension width relative to the spacing from said photoelectron ejection means.

4. The head of claim 3 wherein said photoemissive element is perforated.

5. The head of claim 1 wherein said means for detecting is an electron multiplier.

6. The head of claim 1 wherein a first bias potential is applied to said photoelectron ejection means whereby said photoelectron ejection means becomes negative with respect to said photoemissive element and wherein said sampling potential has a magnitude greater than said first bias potential, thereby rendering said photoelectron ejection means momentarily positive with respect to said photoemissive element.

7. An optoelectronic sampling head comprising a housing having an optical path for impinging light, a photoemissive elongated strip positioned across said optical path and supported in said housing by broadband insulated electrical feedthrough elements, an insert positionable in said housing, said insert including a photoelectron ejection ground plane and an electron path, and spacer means mounted to said insert and positioned with said insert against said housing for positioning said photoelectron ejection ground plane with predetermined spatial distance from said photoemissive strip.

8. The head of claim 7 wherein said photoelectron ejection ground plane is a circular wire mesh.

9. The head of claim 8 wherein said photoemissive element is perforated or semitransparent.

10. The optoelectronic sampling head of claim 7 further including means for applying a high frequency content sampling potential difference along said broadband feedthrough elements relative to said ground plane for accelerating photoelectrons emitted by said photoemissive strip toward said ground plane and along said electron path, and means coupled to said housing for receiving and detecting electrons passing along said electron path.

11. The head of claim 10 wherein said photoelectron ejection ground plane is a metallic mesh.

12. The head of claim 10 wherein said photoemissive element is perforated or semitransparent.

13. The head of claim 10 wherein said means coupled to said housing is an electron multiplier.

14. The head of claim 10 wherein a first electron retarding potential is applied to said photoelectron ejection ground plane and wherein said sampling potential exceeds said first retarding bias potential and is negative with respect to the potential of said photoelectron ejection ground plane.

15. The sampling head of claim 7, wherein said photoelectron ejection ground plane is spaced from said strip a distance up to 300 microns.

16. An optoelectronic sampling head comprising a conductive housing defining an optical path in the axial direction of said housing for impinging light, a pair of diametrically opposite apertures in said housing, insulation means sealed in said apertures, electrical leads extending through said insulating means, an elongated photoemissive strip supported on said leads inside said

7

housing, a conductive insert positioned within said housing and having affixed thereto a perforated photoelectron ejection ground plane normal to the axis of said housing, said ground plane being spaced from said elongated strip a distance up to 300 microns in the axial direction of said housing, and electron multiplier means affixed to said housing in the optical path on the end thereof toward said ground plane, whereby said ground plane constitutes a microstrip ground plane for said strip.

8

17. The sampling head of claim 16 wherein said housing is provided with internal threads, said insert having external threads engaging said internal threads whereby the axial position of said ground plane is adjustable, whereby said ground plane is electrically connected to said housing, and further comprising a source of a sampling potential connected to said leads, and a source of a bias potential connected to said leads.

* * * * *